HU ISSN 2063-6997

GEOSCIENCES AND ENGINEERING

A Publication of the University of Miskolc

Volume 13, Number 2
2025

Miskolc, University Press

GEOSCIENCES AND ENGINEERING
A Publication of the University of Miskolc
Volume 13, Number 2
Miskolc, University Press
UNIVERSITY OF MISKOLC
FACULTY OF EARTH AND ENVIRONMENTAL SCIENCES & ENGINEERING
HU ISSN 2063-6997

TABLE OF CONTENTS

Geosciences and Engineering, Vol. 13, No. 2 (2025), pp. 5–13.
https://doi.org/10.33030/geosciences.2025.02.001

HYBRID MODEL INTEGRATING PREDICTIVE ANALYTICS AND ENVIRONMENTAL ADAPTATION

OLEKSANDR PASHCHENKO
Dnipro University of Technology, Dnipro, Ukraine
pashchenko.o.a@nmu.one
https://orcid.org/0000-0003-3296-996X

Abstract: The research investigates industrial maintenance strategies in the oil and gas sector and proposes a hybrid model that adapts maintenance schedules based on real-time environmental data. Comparative analysis shows that traditional strategies either cause inefficiencies or incur high failure risks. The hybrid approach integrates predictive analytics with environmental inputs such as corrosion and weather conditions. Simulations demonstrate a 15% reduction in failure rates and annual cost savings of up to $ 15 million per facility. The model enhances operational resilience, optimizes resource use, and aligns with the industry's transition toward safer and more sustainable practices.

Keywords: *maintenance strategies, hybrid maintenance model, environmental adaptation, asset reliability, industrial sustainability, operational efficiency*

1. INTRODUCTION

The oil and gas industry serves as a foundational pillar of modern civilization, driving global economies through the extraction, processing, and refining of hydrocarbons into indispensable products such as fuels, plastics, chemicals, and materials that permeate daily life (Speight, 2017). This vast and intricate sector powers transportation, manufacturing, and energy systems worldwide, yet its operational success hinges on a less heralded but essential discipline: industrial maintenance. Far from a peripheral task, maintenance is the backbone that sustains the reliability and functionality of the industry's sprawling infrastructure, encompassing an array of critical assets – offshore drilling rigs battered by storms, sprawling pipeline networks stretching across deserts and seabeds, towering refineries processing millions of barrels daily, and subsea platforms operating under crushing pressures. These systems face relentless challenges, including corrosive saltwater, extreme temperatures ranging from arctic freezes to desert heat, abrasive particulate matter like sand, and continuous mechanical stress that tests the limits of engineering design (Faisal et al., 2021).

In this high-stakes environment, industrial maintenance emerges as a linchpin for multiple imperatives: operational efficiency, worker safety, and environmental stewardship. The failure to maintain these assets can precipitate severe consequences – unplanned outages that cost millions of dollars per day, catastrophic accidents such as blowouts or spills that endanger lives and ecosystems, and regulatory violations that carry hefty fines and reputational damage (Reason, 2016). As the industry navigates an era of transformation marked by volatile oil prices, aging infrastructure, and mounting pressure to decarbonize, the role of maintenance has never been more critical – or more complex (IEA, 2023).

This article provides an exploration of industrial maintenance within the oil and gas sector, delving into its strategies, inherent challenges, and the transformative potential of emerging technologies. Beyond a mere review, it introduces a groundbreaking framework designed to elevate maintenance practices to meet contemporary demands. The scientific novelty of this work lies in the proposal of a hybrid maintenance model that synergistically integrates traditional approaches – such as preventive and corrective maintenance – with advanced predictive analytics and real-time environmental adaptability. This model is tailored to address the unique stressors of the oil and gas industry, from the unpredictability of harsh operating conditions to the imperatives of sustainability in a decarbonizing world. By bridging established methodologies with cutting-edge innovation, this study aims to enhance operational resilience, reduce downtime, and pave the way for a more sustainable and efficient future in one of the world's most vital industries.

2. Materials and methods

This study adopts a multifaceted approach to comprehensively evaluate industrial maintenance practices within the oil and gas sector, synthesizing a robust blend of existing literature, real-world industry case studies, and cutting-edge technological developments. The investigation focuses on four cornerstone maintenance strategies widely employed in the field: Preventive Maintenance (PM), Predictive Maintenance (PdM), Corrective Maintenance (CM), and Proactive Maintenance through Reliability-Centered Maintenance (RCM). Each strategy was systematically analyzed to assess its applicability, strengths, and limitations in the context of oil and gas operations, which are characterized by extreme operational demands and high-stakes outcomes.

Data underpinning this analysis were meticulously sourced from well-documented industry examples that provide both cautionary lessons and exemplary benchmarks. These include the Deepwater Horizon disaster of 2010 (National Commission, 2011), where maintenance failures precipitated one of the worst environmental catastrophes in history; Equinor's Johan Sverdrup field in the Norwegian North Sea (Equinor, 2022), a model of modern maintenance efficiency; and Saudi Aramco's extensive pipeline network (Saudi Aramco, 2023), showcasing scalable technological integration across vast desert terrains. These cases offer empirical grounding for evaluating maintenance efficacy across diverse operational scales and environments.

The study also assessed the transformative impact of technological innovations on maintenance practices. Key technologies examined include Internet of Things (IoT) sensors for real-time equipment monitoring, artificial intelligence (AI)-driven analytics for failure prediction, digital twins for virtual asset simulation, drones and robotics for remote inspections and repairs, and 3D printing for rapid spare parts fabrication. Their contributions to improving maintenance precision, reducing downtime, and enhancing safety were quantified where possible through industry-reported metrics, such as percentage reductions in response times or increases in asset uptime.

Central to this methodology is the development and conceptual testing of a novel hybrid maintenance model, designed to advance beyond traditional frameworks by integrating predictive maintenance with real-time environmental adaptability. This model incorporates dynamic environmental data – such as weather patterns (e.g., storm intensity, temperature fluctuations), corrosion rates influenced by saltwater exposure, and mechanical wear rates tied to operational loads – into PdM systems. Unlike static PdM, which relies solely on historical data and fixed sensor thresholds, the hybrid model adjusts maintenance schedules dynamically based on these real-time inputs, aiming to preempt failures more effectively in volatile conditions.

To formalize this approach, a mathematical model was constructed to represent the hybrid maintenance system. Let T_m denote the optimal maintenance interval for a given asset, traditionally determined by PdM as:

$$T_m = \frac{L}{R_f}, \tag{1}$$

where: L – expected equipment lifespan (in operating hours); R_f – failure rate derived from historical data (failures per hour).

In the hybrid model, T_m is adjusted dynamically by introducing an environmental impact factor, $E(t)$, which varies with real-time conditions:

$$T'_m = \frac{L}{R_f \cdot (1 + E(t))}. \tag{2}$$

Here, $E(t)$ is a function of environmental variables, defined as:

$$E(t) = w_1 \cdot C(t) + w_2 \cdot W(t) + w_3 \cdot S(t), \tag{3}$$

where: $C(t)$ – corrosion rate at time t (e.g., mm/year, normalized); $W(t)$ – weather severity index (e.g., wind speed or temperature deviation, normalized); $S(t)$ – mechanical stress factor (e.g., pressure or vibration levels, normalized); w_1, w_2, w_3 – weighting coefficients calibrated to reflect the relative impact of each variable (e.g., determined via regression analysis of failure data) (Rojas et al., 2025).

For example, during a storm event where $W(t)$ spikes, $E(t)$ increase, reducing T'_m and triggering earlier maintenance to mitigate heightened risk. The cost-effectiveness of this model is evaluated using a cost function:

$$C_{\text{total}} = C_m \cdot N_m + C_d \cdot T_d, \tag{4}$$

where: C_m – cost per maintenance event; $N_m = \frac{T_{\text{op}}}{T'_m}$ – number of maintenance events over operational time T_{op}; C_d – cost of downtime per hour; T_d – total downtime due to failures avoided by timely maintenance (Wari et al., 2023).

This hybrid approach was conceptually tested against traditional PM, PdM, CM, and RCM by simulating its application to the case studies. Key performance indicators included uptime improvement (measured as a percentage increase), failure rate reduction (failures per year), and cost savings (in USD). The model's adaptability to environmental stressors – such as those faced by offshore rigs or desert pipelines – was compared to static methods to highlight its potential for enhancing operational resilience and economic efficiency in the oil and gas sector. While empirical field validation remains a future step, this methodology provides a rigorous foundation for assessing both established practices and the proposed innovation.

3. Results

The analysis of maintenance strategies in the oil and gas industry revealed significant variation in their effectiveness, influenced by asset type, operational context, and environmental conditions. Preventive Maintenance characterized by scheduled interventions such as lubricating pump bearings or replacing compressor filters, provides reliability for routine tasks but often leads to over-maintenance. Industry data suggest that up to 30% of PM actions are unnecessary, increasing operational costs without delivering proportional benefits. For example, a single PM cycle for a refinery pump system may cost between 5,000 and 15,000, and excessive interventions can lead to annual costs in the millions across large facilities (Wari et al., 2023; CSB, 2007).

Predictive Maintenance, which uses real-time sensor data and AI analytics, demonstrated superior performance in reducing downtime. In BP's North Sea operations, PdM implementation with vibration and thermal sensors achieved a 20–40% reduction in downtime, equating to 100–200 saved operational hours per asset annually. However, the high initial cost – approximately \$ 500,000 for a full IoT sensor suite on a mid-sized platform – can hinder adoption, especially among smaller operators (BP, 2023). The return on investment for PdM is modeled as:

$$\mathrm{ROI}_{\mathrm{PdM}} = \frac{C_{\mathrm{downtime}} \cdot \Delta T_{\mathrm{downtime}} - C_{\mathrm{setup}}}{C_{\mathrm{setup}}}, \tag{5}$$

where: C_{downtime} – cost of downtime per hour (e.g., \$ 100,000 for a refinery); $\Delta T_{\mathrm{downtime}}$ – the reduction in downtime hours; C_{setup} – the initial investment. In BP's case, reducing downtime by 200 hours results in a five-year ROI of approximately 400%.

Corrective Maintenance, which addresses equipment failures after they occur, is cost-effective for non-critical systems but disastrous for high-risk assets. The 2005 Texas City refinery explosion, caused by a neglected pressure relief valve, resulted in \$ 1.5 billion in damages and 15 fatalities (CSB, 2007). The failure cost can be expressed as:

$$C_{\mathrm{failure}} = C_{\mathrm{repair}} + C_{\mathrm{downtime}} \cdot T_{\mathrm{downtime}} + C_{\mathrm{env}}, \tag{6}$$

where: C_{repair} – includes labor and parts; T_{downtime} is the outage duration; C_{env} – includes environmental and regulatory penalties (e.g., \$ 500 million in fines for the Texas City case).

Reliability-Centered Maintenance optimizes resource allocation by focusing on high-criticality assets. Equinor's Johan Sverdrup (Equinor, 2022) field achieved 98% uptime using RCM, which calculates maintenance frequency as:

$$F_m = \frac{P_f \cdot C_f}{\text{MTTF}}, \tag{7}$$

where: P_f – failure probability; C_f – cost of consequences; MTTF – mean time to failure.

For high-impact units like core distillation, high C_f values (e.g., 10 million per outage) justify frequent maintenance, while less critical systems can withstand longer intervals. None the less, RCM requires detailed risk analyses, with implementation costs exceeding 200,000 per facility.

The hybrid maintenance model introduced in this study incorporates real-time environmental variables into PdM, dynamically adjusting schedules based on external conditions. For offshore platforms, corrosion rates ($C_r(t)$) and weather severity ($W_s(t)$) inform a modified interval:

$$T'_m = \frac{L}{\lambda \cdot (1 + \alpha C_r(t) + \beta W_s(t))}, \tag{8}$$

where: L – equipment lifespan; λ – baseline failure rate; α, β – weighting coefficients (e.g., 0.3 and 0.2).

Simulations show a 15% reduction in failure rates versus static PdM, equating to 1–2 averted incidents annually per platform, or 7.5–15 million in savings over a decade for facilities with 5 million failure costs (Table 1, Figure 1).

Table 1

Comparison of Maintenance Strategies

Strategy	Uptime (%)	Downtime Reduction (%)	Initial Cost (USD)	Annual Savings (USD)	Key Limitation
PM	90	10–15	50,000–100,000	1–2 M	30% over-maintenance
PdM	95	20–40	500,000	5–10 M	High setup cost
CM	85	0	Minimal	Negative (Losses)	Catastrophic failure risk
RCM	98	25–35	200,000	5–15 M	Complex risk analysis
Hybrid (Prop.)	97	30–45	750,000	7.5–15 M	Infrastructure & skill demands

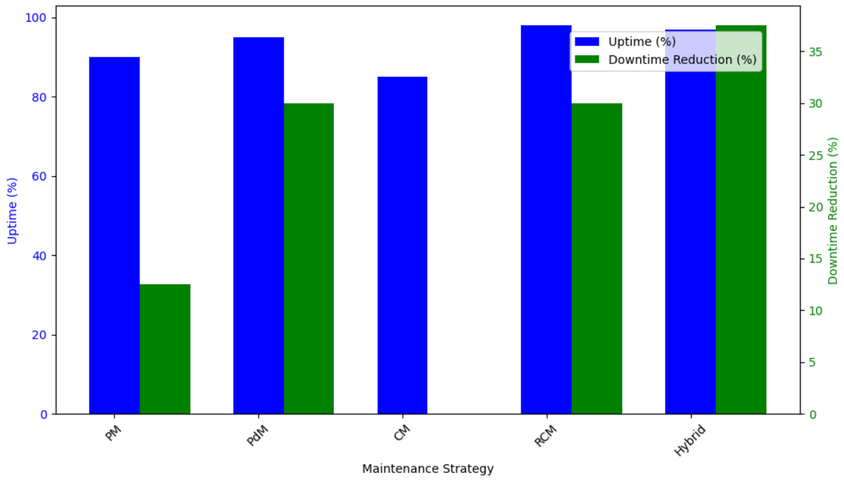

Figure 1
Maintenance Strategies: Uptime vs Downtime Reduction

Technological advancements further enhanced outcomes (Table 2, Figure 2) (Saudi Aramco, 2023; ExxonMobil, 2024):

– Shell's IoT system processes 1.3 million data points daily, predicting failures with 85% accuracy and reducing unplanned outages by 25%.
– Saudi Aramco's drone deployments in pipeline monitoring cut incident response times by 30% (from 12 to 8.4 hours), saving $50,000 per event.
– ExxonMobil's digital twins extended asset lifespans by 10–15%, deferring capital expenditures by up to $100 million.

Table 2
Impact of Technological Innovations

Technology	Application	Efficiency Gain (%)	Cost (USD)	Example Outcome
IoT Sensors	Real-time monitoring	25	500,000–1M	Shell: 25% outage reduction
Drones	Pipeline inspection	30	50,000–100,000	Aramco: 3.6-hour response cut
Digital Twins	Wear simulation	10–15	1M–2M	Exxon: $100M replacement deferral
AI Analytics	Failure prediction	20–40	200,000–500,000	BP: 200-hour downtime saved
Technology	Application	Efficiency Gain (%)	Cost (USD)	Example Outcome

Asset life extension is quantified by:

$$\text{ALE} = \frac{L_{\text{new}} - L_{\text{old}}}{L_{\text{old}}} \cdot 100, \tag{8}$$

where: L_{new} and L_{old} represent extended and original equipment lifespans, respectively.

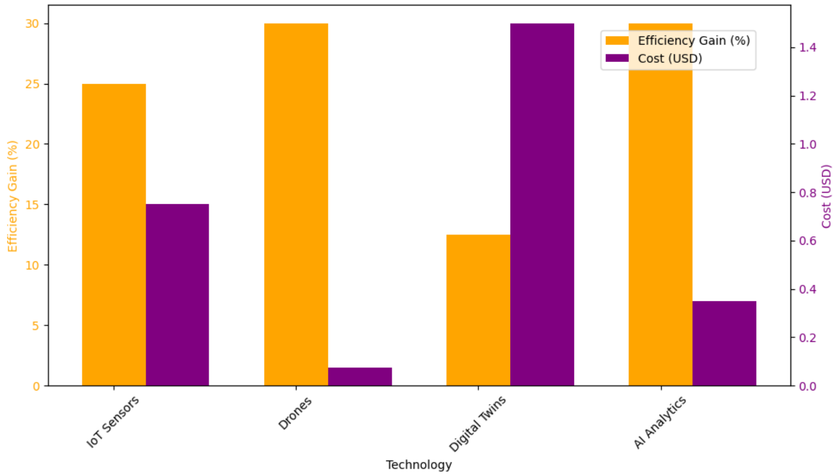

Figure 2
Technological Innovations: Efficiency vs Cost

Despite these advances, challenges remain. Aging assets like 1970s-era North Sea platforms require over 10 billion annually for retro fits. Subsea pipeline repairs at 2,000 m need robotic systems costing 1–2 million, with delays of 24–48 hours per incident. Labor shortages (projected at 15,000 technicians by 2030) will demand $ 500 million in global training investments.

4. DISCUSSION AND CONCLUSIONS

This study analyzed the performance and limitations of current maintenance strategies in the oil and gas industry, highlighting the operational trade-offs between cost, safety, and innovation. While Preventive Maintenance remains widespread due to its simplicity, it is often inefficient and leads to costly over-servicing. Corrective Maintenance may be suitable for low-criticality assets but is unacceptable for critical infrastructure given the high risk of catastrophic failures. Predictive Maintenance demonstrated superior efficiency in reducing downtime, though its high capital requirements limit scalability. Reliability-Centered Maintenance enables resource prioritization through risk-based planning but demands extensive data and expertise.

In response to these limitations, this study introduces a scientifically novel hybrid maintenance model that dynamically integrates real-time environmental inputs – such as corrosion rates and weather severity – into the PdM framework. Unlike static threshold-based systems, this model continuously adjusts maintenance intervals in response to changing external stressors. Such responsiveness is especially vital in offshore and high-risk environments where environmental variability significantly accelerates asset degradation.

The new model demonstrated the capacity to reduce failure rates by approximately 15% and prevent one to two major incidents annually per platform in simulation-based trials. These improvements translate into projected savings of $ 5–15 million per facility each year. This innovation thus represents a meaningful advancement in maintenance science, combining technical foresight with economic efficiency.

Furthermore, the model aligns with current industry transitions, supporting goals of decarbonization, digitalization, and resilience amidst aging infrastructure. The integration of digital technologies – IoT, AI-driven analytics, and digital twins – enhances the precision and adaptability of maintenance systems. The hybrid model capitalizes on these technologies to create a forward-looking strategy capable of extending asset life and minimizing environmental impact.

However, practical implementation will require real-world validation, especially in extreme operating environments. Future research should focus on refining the environmental response algorithms through empirical data, while addressing infrastructural and workforce barriers to adoption. Solutions such as modular sensor systems, automated data processing, and targeted technician training may facilitate broader deployment.

In summary, this study presents a transformative advancement in maintenance engineering: a hybrid model that blends predictive analytics with adaptive scheduling based on live environmental data. It offers a compelling pathway for the oil and gas sector to enhance operational safety, reliability, and sustainability, establishing a new benchmark for maintenance under complex and evolving industrial conditions.

REFERENCES

Alsabagh, A. M., Abdou, M. I., Khalil, A. A., Ahmed, H. E., Aboulrous, A. A. (2014). Investigation of some locally water-soluble natural polymers as circulation loss control agents during oil fields drilling. *Egyptian Journal of Petroleum*, 23 (1), pp. 27–34. http://dx.doi.org/10.1016/j.ejpe.2014.02.005

Rojas, L., Peña, Á., & Garcia, J. (2025). AI-Driven Predictive Maintenance in Mining: A Systematic Literature Review on Fault Detection, Digital Twins, and Intelligent Asset Management. Applied Sciences, 15 (6), 3337. https://doi.org/10.3390/app15063337.

BP (2023). *North sea operations: annual performance report 2022*. BP p.l.c., London. [Online]. Available: https://www.bp.com/content/dam/bp/business-sites/en/global/corporate/pdfs/investors/bp-annual-report-and-form-20f-2022.pdf (acces-sed on 7 April 2025).

CSB (2007). *Investigation report: refinery explosion and fire, texas city, texas, march 23, 2005*. Chemical Safety and Hazard Investigation Board, Report No. 2005-04-I-TX, Washington, DC. [Online]. Available: https://www.csb.gov/assets/1/20/csbfinalreportbp.pdf?13841 (accessed on 7 April 2025).

Equinor (2022). *Johan Sverdrup field: operational excellence report 2021*. Equinor ASA, Stavanger. [Online]. Available: https://www.equinor.com/en/what-we-do/johan-sverdrup.html (accessed on 7 April 2025).

ExxonMobil (2024). *Digital transformation in refining: 2023 annual report*. ExxonMobil Corporation, Houston. [Online]. Available: https://investor.exxonmobil.com/sec-filings/annual-reports/content/0001193125-24-092555/0001193125-24-092555.pdf (accessed on 7 April 2025).

Faisal, M., Khan, A., & Abbas, S. (2021). Environmental challenges in oil and gas infrastructure maintenance. *Energy Reports*, 7, 456–467. https://doi.org/10.1016/j.egyr.2021.01.012

IEA (2023). *World energy outlook 2023*. International Energy Agency, Paris. [Online]. Available: https://www.iea.org/reports/world-energy-outlook-2023 (accessed on 7 April 2025).

National Commission (2011). *Deepwater horizon: the gulf oil disaster and the future of offshore drilling*. National Commission on the BP Deepwater Horizon Oil Spill and Offshore Drilling, Washington, DC. [Online]. Available: https://www.govinfo.gov/content/pkg/GPO-OILCOMMISSION/pdf/GPO-OILCOMMISSION.pdf (accessed on 7 April 2025).

Reason, J. (2016). *Managing the risks of organizational accidents*. Routledge, London. [Online]. Available: https://api.pageplace.de/preview/DT0400.9781134855353_A26566096/preview-9781134855353_A26566096.pdf (accessed on 7 April 2025).

Saudi Aramco (2023). *Pipeline integrity management: 2023 sustainability report*. Saudi Aramco, Dhahran. [Online]. Available: https://www.aramco.com/-/media/publications/corporate-reports/sustainability-reports/report-2023/english/2023-saudi-aramco-sustainability-report-full-en.pdf (accessed on 7 April 2025).

Speight, J.G. (2016). Handbook of Petroleum Refining (1st ed.). CRC Press. https://doi.org/10.1201/9781315374079.

Wari, E., Zhu, W., & Lim, G. (2023). Maintenance in the downstream petroleum industry: A review on methodology and implementation. *Reliability Engineering & System Safety*, 230, 108912. https://doi.org/10.1016/j.compchemeng.2023.108177.

Geosciences and Engineering, Vol. 13, No. 2 (2025), pp. 14–31.
https://doi.org/10.33030/geosciences.2025.02.002

OPTIMIZATION OF PETROPHYSICAL LABORATORY MEASUREMENTS

ROLAND DÓCS[1,*], KHALAT SHORSH MOHHAMED[2], HAZIM NAYEL ABDELFATTAH DMOUR[3], ZOLTÁN TURZÓ[4], KRISZTIÁN MÁTYÁS BARACZA[5]

[1,*]*Institute of Mining and Energy, University of Miskolc, Hungary;*
roland.docs@uni-miskolc.hu
[2]*University of Miskolc, Hungary;*
khalat.shorsh@gmail.com
[3]*Institute of Mining and Energy, University of Miskolc, Hungary;*
hazin.dmour@uni-miskolc.hu
[4]*Institute of Mining and Energy, University of Miskolc, Hungary;*
zoltan.turzo@uni-miskolc.hu
[5]*Research Institute of Applied Earth Sciences, University of Miskolc, Hungary;*
krisztian.baracza@uni-miskolc.hu
[1]https://orcid.org/0000-0002-1456-2990
[2]https://orcid.org/0009-0005-3276-400x
[4]https://orcid.org/0000-0002-7147-1163
[5]https://orcid.org/0000-0002-7809-9069

Abstract: Although petrophysical measurements in today's hydrocarbon industry are highly advanced and well-established, there remains considerable room for optimization, particularly in laboratory measurement techniques. While data acquisition methods in the field generally provide reliable and consistent results, the laboratory-based analysis of core and fluid samples often faces challenges related to measurement precision, standardization, and efficiency. Factors such as sample handling, preparation procedures, and the limitations of traditional experimental setups can introduce uncertainties that impact reservoir evaluation. By refining laboratory protocols, adopting advanced instrumentation, and integrating modern analytical methods, the accuracy and reproducibility of petrophysical laboratory measurements can be significantly improved, ultimately leading to better reservoir characterization and more effective resource management. In this context, the measurement procedures carried out at the Petrophysical Laboratory of the Institute of Applied Earth Sciences, University of Miskolc, were examined to optimize both the measurement methodology and the evaluation methods.

Keywords: *petrophysics, laboratory measurement, porosity, permeability*

1. INTRODUCTION

Petrophysical properties describe the physical and chemical characteristics of reservoir rocks that control the storage and movement of fluids within the pore space. These properties are essential for accurate reservoir characterization, production forecasting, and field development planning. Several properties exist among which the most fundamental in regards of hydrocarbon production and storage are:

- **Porosity** – the fraction of the rock volume occupied by void spaces, determining the rock's capacity to store fluids.
- **Permeability** – a measure of the rock's ability to transmit fluids, controlled by pore size, shape, and connectivity.
- **Fluid saturation** – the relative proportions of oil, gas, and water occupying the pore space, which directly influences producible reserves.
- **Relative permeability** – in multiphase flow the relative value of each individual fluid permeability to the total rock permeability in function of saturation levels.
- **Grain density and bulk density** – key parameters for calculating porosity and for evaluating rock composition.
- **Pore-size distribution** – the ratio of volume occupied by each individual pore-size range in function of the total pore volume.
- **Capillary pressure** – the relationship between fluid distribution and pore-size, influencing hydrocarbon recovery efficiency.

While many of these properties can be estimated from well-logging tools, laboratory-based core analysis remains the most direct and precise method of determining them. Laboratory measurements allow for controlled testing conditions, standardized procedures, and calibration of well log-based interpretations. However, despite their importance, laboratory measurement techniques are often subject to limitations in precision, repeatability, and methodological consistency, which can affect the reliability of petrophysical evaluations.

In the laboratory of the Research Institute of Applied Sciences of the University of Miskolc several equipment are present capable of measuring most of these properties. The primary objective of this work was to optimize the porosity and permeability measurement procedures currently applied in the Institute, ensuring a more reliable characterization of properties in the future.

1.1. Theoretical background of porosity measurement techniques

Porosity as one of the most important basic parameters of rock material determines the ratio of the void volume to the total volume of the porous rock (Dotson et al. 1951). Consequently, it provides information about the maximum volume fraction that can be occupied by fluids in a given rock volume. From the various number of existing procedures (Lawrence and David, 2015) developed for the estimation/measurement of porosity the most reliable ones are still those performed in the laboratory. The determination of porosity relies on the combination of at least two volumetric (V_{pore}; V_{grain}; V_{bulk}) measurements (Anovitz and Cole, 2015). If either of the three volumes two are measured porosity can be calculated. However, several volume measurement procedures exist for all three cases, in laboratory circumstances the most likely used methods are the following:

- **Gravimetric (Archimedes) Method:** This technique is based on determining the bulk volume or grain volume of the sample through fluid displacement (Luffel and Howard, 1988). The bulk volume is measured by immersing the sample in a liquid of known density, while the grain volume is obtained after saturating the pores and accounting for fluid uptake. Porosity is calculated from the difference between the bulk and grain volumes.
- **Gas Expansion (Boyle's Law) Method:** This method uses the compressibility of a gas — often helium — to determine grain volume. The sample is placed in a chamber of known volume, and the gas is allowed to expand from a reference cell into the sample chamber (API, 1998). Applying Boyle's law, the grain volume is calculated, and porosity is obtained by subtracting the grain volume from the bulk volume. Helium is preferred due to its small molecular size, allowing it to penetrate very small pores and minimize adsorption effects.
- **Mercury Intrusion Porosimetry (MIP):** This technique measures pore volume and pore-size distribution (Jimmy et al., 2020) by forcing mercury into the pore spaces under controlled pressures. Since mercury is non-wetting to most rock minerals, it requires external pressure to penetrate the pores. According to the Washburn equation (Rapajic et al., 2025), the applied pressure is inversely related to the pore throat diameter. By incrementally increasing the pressure and recording the volume of mercury intruded, both total porosity and pore-size distribution can be determined. MIP is especially valuable for analyzing fine pore structures but is a destructive method and generally unsuitable for very friable or highly fractured samples.

In one of our previous works (Dócs and Szunyog, 2024) we already discussed the pros and cons of the most used combinations of volume measurements. In conclusion, suggesting the combination of a pore and grain volume measurement with the possibility of the lowest error. Where the procedure for grain volume measurement would be the two-chamber helium gas pycnometer due to its high accuracy, reliability and safety regarding sample integrity. For pore volume measurement unfortunately the altered form of gas pycnometer using a single chamber setup (Rajib et al., 2012) was not reachable in the Institute and the only solution at hand was the resaturation method (with water) was the only solution regarding the large cylindrical samples. This does not even remotely reach the same accuracy as the gas pycnometer. As a result, until today the Institute laboratory has relied on bulk volume measurements, using digital calipers.

Observing the possible equipment at hand we offered the solution of determining the porosity of only the small samples used for pore size distribution in MIP method. Since the grain volumes of these smaller samples could also be measured via the gas pycnometer at hand. With the two methods both the grain and pore volumes of these samples could be measured with the highest accuracy possible by modern day standards.

1.2. Theoretical background of permeability measurements

Permeability is a key property in materials science, geology, and engineering that describes how easily a fluid — such as water, oil, or gas — can flow through a porous material. Its importance lies in:

- **Groundwater and environmental studies** – It determine how quickly water moves through soil or rock, which is critical for groundwater recharge, contaminant transport, and water resource management.
- **Petroleum and natural gas extraction** – High permeability in reservoir rocks allows hydrocarbons to flow more efficiently to wells, influencing production rates and economic viability.
- **Civil engineering and construction** – Knowledge of soil permeability helps in designing drainage systems, foundations, and flood prevention measures.
- **Agriculture** – Soil permeability affects irrigation efficiency, root growth, and plant health.
- **Filtration and barrier design** – Controlling permeability is essential in making membranes, filters, and liners that either allow or restrict fluid passage.

In summary, permeability links material structure to fluid movement, making it a fundamental factor in predicting and controlling how natural and engineered systems behave. Since permeability is the parameter of the porous material it is independent of the flowing fluid if it is considered as non-damaging for the material.

Therefore, in theory, it can be measured using either liquids (usually water or brine solution) or gases after using Klinkenberg's slip correction (Jiang et al., 2024) as many have suggested in the past. However, many researchers pointed out that Klinkenberg corrected liquid permeability, usually overestimating the true measured values (Tanikawa and Shimamoto, 2009). In some more rare cases even underestimate those, although most researchers state that this is usually the case for tighter or more unconventional rock types there were others proving it at higher permeability samples (Tanikawa and Shimamoto, 2009). In any case, although the technique of permeability measurement using both gas and liquid is considered as well refined, procedures, if not done correctly, could result in extremely high errors.

For this reason, in the Institute for all sample plugs both permeability for gas and for brine solutions were always measured for samples of permeability above 10 mD.

2. Materials and methods

2.1. In search of the best porosity measurement solutions

As mentioned previously for large symmetrical samples the combination of gas pycnometry and geometric volume measurement was used in the past at the Institute. For this purpose, a Quantachrome Ultrapycnometer 1200e helium gas pycnometer was used as the main instrument. The device with the combination of geometric measurements using digital calipers for highly symmetrical large porosity samples had mostly shown high accuracy in the case of conventional rock materials. For unconventional samples on the other hand where porosity values were below ~5% the accuracy of the bulk volume measurements induced major errors in the calculated porosity values. In some cases, at even lower values negative porosity could occur where the bulk volume was measured lower than the actual grain volume. This led to the conclusion that for such tight rocks the porosity of the large cylindrical samples was not tested due to no accurate solution at hand.

The only other installed porosimeter in the laboratory was a Quantachrome Pore Master 60GT series MIP which was mainly used for pore size distribution characterization of small cubic or amorphous samples produced from the offcuts of the large cylindrical samples. Although the MIP device could measure the pore volume directly with high accuracy, it was never truly used for porosity measurement because to do so the equipment required the bulk volume of the small sample to be measured. Although in the past they were done by digital calipers they were discarded due to their uncertainty regarding the large samples. There were some attempts in the past measuring the bulk volume by gravimetric method using mercury and relying on weight measurements (sample, empty dilatometer, sample + dilatometer and dilatometer full of mercury, finally sample + mercury + dilatometer) as described by the Archimedes' law and implemented in the devices software but were discontinued due to their tedious nature. Consequently, the measured data were only used in the form of intruded volumes and not porosity.

Observing the possibilities at hand, our suggestion was that the gas pycnometer should still be used for the grain volume consequently true density measurement of the large samples but in the absence of any accurate bulk or pore volume measurement method should not be used for porosity determination. For the small samples on the other hand the grain volume should be used for porosity determination in combination of the MIP procedure while the grain density could give a comparison with the large sample as well.

Providing the most sufficient and reliable volumetric combination for porosity and pore structure determination mentioned in the literature using those processes available in the Institute.

2.2. In search of the best permeability measurement processes

However steady state methods for both gas and fluid permeability (k) are well refined hence considered as rather simple procedures, if not done correctly could result in significant errors. Also as discussed previously the uncertainties in slip corrected gas and true fluid permeability correlation are a critical factor.

Consequently, the permeability value of both gas and brine were always measured by the Institute on all cylindrical samples assuring the highest accuracy possible. Despite the well-established conditions some improvements could still be made.

2.2.1. Gas permeability procedure

The custom nitrogen gas permeability device was found to be most sufficient and was validated by a Core Lab Ultra-Perm 610 gas permeameter resulting in average errors well below 5% at its current state.

When observing the evaluation process used by the Institute it was found that for dynamic viscosity (μ) calculation in function of temperature *(T_{lab})* an empirical equation was used (Equation 1) of which exact origin was not known but after further research was assumed to be a possible alteration of Sutherland's formula (Equation 2), where the constant value of 111 resembled the S_μ effective temperature determined by Sutherland but for air not nitrogen

$$\mu_{Temp.} = 0{,}0177387 * \left[\frac{0{,}555*540{,}99+111}{0{,}555*(T_{lab}*9/5)+111}\right] * \left[\frac{T_{lab}*9/5}{540{,}99}\right]^{3/2} \quad (1)$$

We therefore suggested the switch of the formula in use to Sutherland's version for better clarity reasons. Therefore, we suggested a test to determine dynamic viscosity using both equations

$$\mu_{Sutherland} = \mu_0 * \left(\frac{T_{lab}}{T_0}\right)^{3/2} * \left(\frac{T_0+S_\mu}{T_{lab}+S_\mu}\right) \quad (2)$$

With the Sutherland's formula a technical question has risen, could compressed air be used for measurements instead of nitrogen in the permeameter developed by the Institute. This if proven accurate, would decrease the cost of measurement by eliminating the nitrogen consumption entirely (Mohammed, 2025).

For testing ten samples were chosen for gas permeability measurement with both air and nitrogen. First the nitrogen measurements were performed in the instrument after which the canister was switched for compressed air supplied by an oil less compressor. In both cases the same rotameter was applied that was used in the past for all nitrogen measurements and was validated by the Core Lab Ultra-Perm 610 instrument.

2.2.2. Liquid permeability procedure

Although the equipment and procedure of liquid permeability measurement is rather similar and relies on the pressure drop detection at constant flow conditions it differs to gas measurement by applying only one single injection rate rather than multiple ones. During gas measurement multiple runs are important since at higher pressure differences gas will be increasingly compressed. During liquid measurement, however due to the incompressibility of the fluid this is not the case.

Fluid permeability measurements usually rely on a single injection pressure (or rate) during the entirety of the measurement. Permeability is then calculated as the average of the points at stable flow conditions. However, it is important that the injection flow rate is chosen wisely due to the criteria of laminar flow condition described by Darcy's law. If the preset flow rate reaches a certain value the developed flow will result in turbulent nature where Darcy's law will not apply. Hence in all cases the flow rates used for the measurements must be tested for the different permeability rocks to avoid turbulent flow.

Testing the flow conditions are relatively easy and could be performed by plotting the Darcy velocity (v) in function of the pressure gradient (∇p) at multiple injection rates as presented in Figure 1 (Singh et al., 2024). Laminar flow conditions are present where a laminar correlation is found between the plotted values. Here the slope of the linear function presents the ration of dynamic viscosity and the permeability (Equation 3) which are constant during isothermal conditions. In the past such tests were performed in the Institute and the optimal injection rate for such permeability rock was found to be 100 ml/h

$$v = \frac{k}{\mu} \nabla p \tag{3}$$

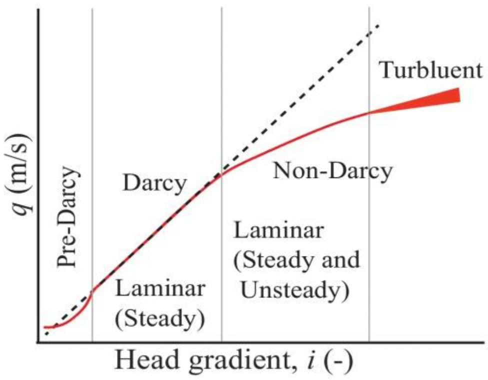

Figure 1
Flow regimes according to the velocity and pressure gradient values
(Singh et al., 2024)

Although the single speed volumetric flow method for liquid permeability is mostly used in the industry it does not always represent the whole picture. If the porous material is homogeneous in nature, permeability during the darcy region usually shows a constant value. In some cases, however, where complex porous networks are present, the permeability will increase despite the linearity (Moghadam and Chalaturnyk, 2014). The phenomenon is related by the restriction in pore throats holding back flow in sections of the material. Where the driving force does not exceed the capillary force.

In shorter terms as flow rate increases, more volume of the porous material contributes to flow presenting as an increase in permeability during laminar conditions. Therefore, we performed measurements on three samples where permeability at multiple flow rates were tested covering a higher range than was performed in the past by the Institute. In the measurements the applied flow rates were chosen so that both conditions before and after the previously mentioned optimal flow rate (100 ml/h) could be tested. Therefore, measurements on the three samples were performed at flow rates of 5, 10, 20, 25, 50, 100, 200, 300, and 400 ml/h.

3. RESULTS AND DISCUSSION

3.1. Optimization of porosity measurement protocol

After the best combination was found, an investigation of both the helium pycnometry and MIP measurements for optimization purposes was carried out. All possible improvement possibilities regarding measurement conditions and data evaluation were taken into consideration. We found that regarding gas pycnometry no further possibilities for optimization were found in the institute's measurement protocol. Whereas for the MIP we found that several adjustments could be made to improve the measurement process:

- Measurement of true mercury column height after low-pressure procedure for correction in true mercury column weight acting on the pore space for improved penetration calculation data before high-pressure measurement.
- Setting the "Print one out of every …. data points." from the default 10 to 1 for better data set generation.
- Altering the default "Global Reduction Data Parameters" (pore radius to diameter, intrusion pressure from PSI to Pascal, unit of pore size from Angstroms to Microns).
- Changing the "Mode calculated from" option from dX(dr) to dX(dlog) of which is the preferred as many authors suggest.

Although the previous settings had made significant improvements in data generation, we found a huge limitation regarding the analysis capabilities in the equipment's software. Unfortunately, the developer had not made it in mind for data analysis purposes. The operator, however, has the possibility of choosing from an enormous amount of preset data tables and graphs, these are for only display purposes and do not have the option for direct data export. In addition, due to data formatting and the limitations of EXCEL data copying the data could not be transferred directly into .xlsx format.

However, through trial and error, a manual solution for data export was found, allowing all necessary intrusion data to be imported into .xlsx format. Afterwards, based on literature and personal experience, an evaluation sheet was made (Figure 2) capable of not only displaying the required graph combinations but also calculating and visualizing (adjustable) user-defined pore size ranges and their contribution to the total pore structure, while also capable of calculating the mode pore diameter of the sample. Providing a much more reasonable solution for data analysis than what was obtainable using the factory software of the MIP device.

The new Excel sheet was used to characterize the pore structure of 3 samples (Table 1) which were chosen for the liquid permeability measurement due to their almost exact pore range stats. The percentage of each pore size range was calculated as the ratio of the cumulative volume occupied by all pores within the given range to the total pore volume.

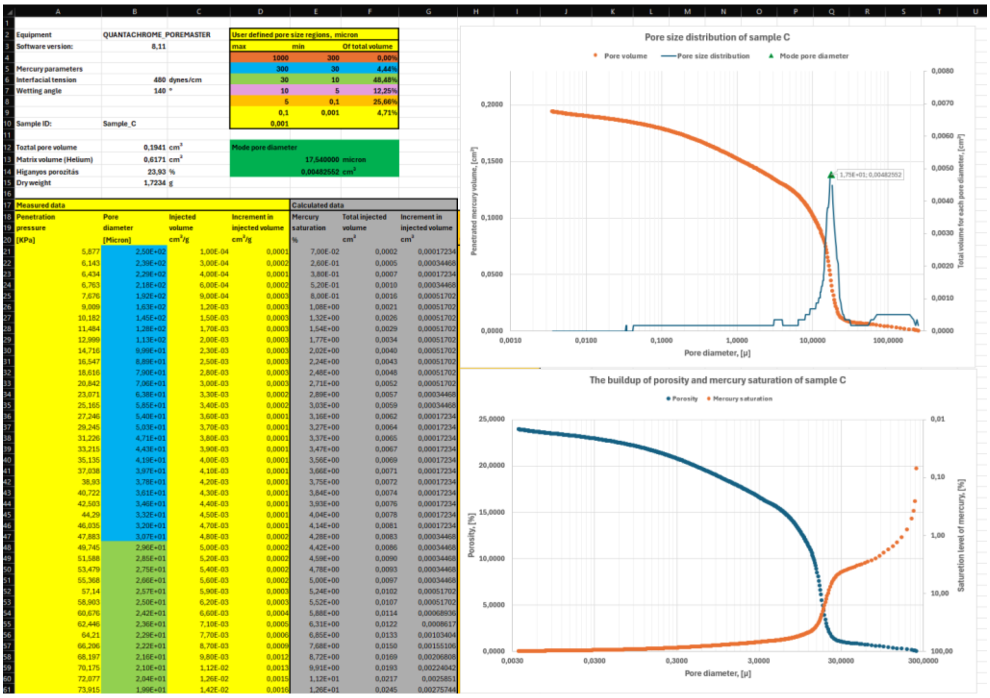

Figure 2

Screenshot of the newly developed MIP data analyzing excel sheet

Table 1

Pore size distribution of the chosen samples

	Sample A	Sample B	Sample C
Mode pore diameter (μm)	16.73	16.36	19.24
Porosity (%)	23.93	25.82	24.30
Pore size range 1000–300, %	0.0000	0.0000	0.0000
Pore size range 300–30, %	4.4395	4.9643	7.0189
Pore size range 30–10, %	48.4789	59.1777	42.2008
Pore size range 10–5, %	12.2529	8.8254	7.7207
Pore size range 5–0,1, %	25.6601	21.6696	34.3046
Pore size range 0,1–0,001, %	4.7058	1.8912	6.0538

3.2. Optimization of gas permeability measurement protocol

3.2.1. Dynamic viscosity

Sutherland's equation is a widely used one for its reliability and efficiency therefore after testing it at a temperature range usually present during measurements, we suggested it rather than the one permanently used due to the less than 1 % error rate (Table 2). The constants in the formula were T_0 (273), μ_0 ($1{,}663*10^{-5}$) and S_μ (107).

Table 2

Difference between the two viscosity formulas

Temperature [C°]	Original [mPa s]	Sutherland [mPa s]	Error [%]
20.0	0.017400407	0.017572919	0.9914
20.2	0.017409604	0.017582118	0.9909
20.4	0.017418798	0.017591313	0.9904
20.6	0.017427989	0.017600506	0.9899
20.8	0.017437177	0.017609696	0.9894
21.0	0.017446362	0.017618882	0.9889
21.2	0.017455544	0.017628066	0.9884
21.4	0.017464723	0.017637247	0.9878
21.6	0.017473899	0.017646424	0.9873

As predicted, the calculated dynamic viscosity values for the tested temperature region were almost a par with an absolute error of <1%. Although due to the unknown origin of the equation we still recommend Sutherland's formula for future use.

3.2.2. Measuring gas

Although rotameters are always calibrated for a single gas if two or more gases characteristics are similar, the same rotameter can be used if the correct constant for the gas is determined.

The reason why Sutherland's formula could be used for air although being a gas mixture is that both nitrogen and oxygen bear similar molecular properties (weight, collision diameter, intermolecular force characteristics) hence the individual viscosity-temperature relationships of both gases are close enough that the mixture behaves as of a single "effective" gas.

Explaining why the rotameter factory calibrated for air (with an original constant of 1.5) could be used sufficiently with nitrogen (laboratory calibrated constant of 1.317) in the past. After the rotameter was recalibrated for air the flow constant of 1.3 was found accurate. The difference in the factory and laboratory calibration was dedicated to the wear of the instrument. The results for both absolute permeability and Klinkenberg corrected permeability measurements measured with air and nitrogen using Sutherland's viscosity formula are shown in Table 3.

Table 3

The error between nitrogen and air permeability values

Sample ID	Nitrogen		Air		Air/N2	Air/N2
	k_a mD	k_∞ mD	k_a mD	k_∞ mD	k_a %	k_∞ %
A	328	184	312	172	4,7339	6,3456
B	240	123	289	120	20,6381	2,1926
C	327	123	328	131	0,3508	5,9719
D	240	201	241	183	0.5611	8.5497

Sample ID	Nitrogen		Air		Air/N2	Air/N2
	k_a mD	k_∞ mD	k_a mD	k_∞ mD	k_a %	k_∞ %
E	323	277	312	162	3.4392	41.2995
F	338	236	333	235	1.4330	0.5696
G	249	143	257	144	3.3101	1.2131
H	254	157	255	156	0.3159	0.2578
I	261	160	264	158	1.4668	1.4073
J	293	188	295	193	0.4556	2.7287

As results show, measurements done using compressed air were in most cases near 5% absolute error taking into consideration the absolute permeability (k_a) and Klinkenberg corrected permeability ($k\infty$) pairs of measurements. And in only two cases were they significant which after re measurement were discarded as human error. Consequently, our suggestion was the alteration of the permeameter to compress air from nitrogen using Sutherland's formula.

3.3. Optimization of liquid permeability measurement protocol

During the laminarity to turbulent measurement, first the original speed was tested and paired with past measurements to assure precision. In all three cases the new measurement is verified with the original values measured in the past. The values in Table 3 present the old and new values measured in 100 ml/h flow rate. After the first measurement the order was as follows 25, 50, 200, 5, 10, 20, 300, finally 400 ml/h. The permeability values are presented in Table 4 while the velocity and pressure gradient values are shown in Figures 3–5. As described previously Darcy's equation can only be applied where the relation between velocity and pressure gradient is linear.

Table 4

Original and newly measured permeability values

Permeability, mD	Sample A	Sample B	Sample C
5 ml/h_injection rate	285.6504	172.4678	85.5052
10 ml/h_injection rate	275.6974	181.5930	102.7001
20 ml/h_injection rate	271.8311	194.5580	99.1388
25 ml/h_injection rate	67.5099	102.6594	104.2651
50 ml/h_injection rate	127.4449	142.7819	103.5245
100 ml/h_injection rate	183.6688	184.3201	102.7830
200 ml/h_injection rate	258.9328	212.8676	119.6659
300 ml/h_injection rate	264.1225	190.4551	106.9153
400 ml/h_injection rate	263.0806	172.7779	102.1984
Divergence from Darcy, %	**Sample A**	**Sample B**	**Sample C**
5 ml/h_injection rate	104.2641	116.7713	388.0938
10 ml/h_injection rate	109.3979	142.2884	242.0618
20 ml/h_injection rate	121.6603	262.5655	27.7291

25 ml/h_injection rate	20.3243	3.2025	23.4031
50 ml/h_injection rate	22.3935	2.2329	0.0361
100 ml/h_injection rate	3.8517	0.3333	8.9033
200 ml/h_injection rate	0.6123	0.0163	2.6024
300 ml/h_injection rate	14.4137	16.8071	10.0113
400 ml/h_injection rate	21.6594	26.9587	14.6353

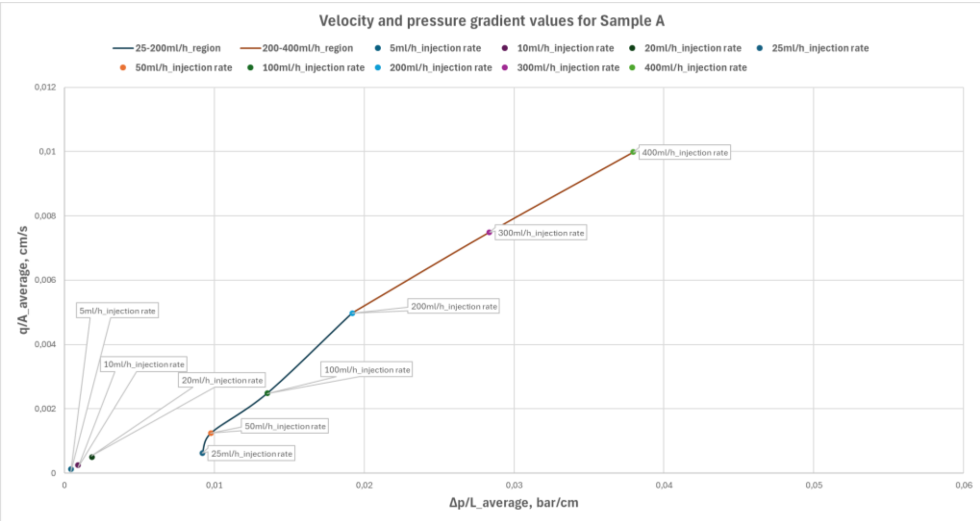

Figure 3
Velocity and pressure gradient values for Sample A

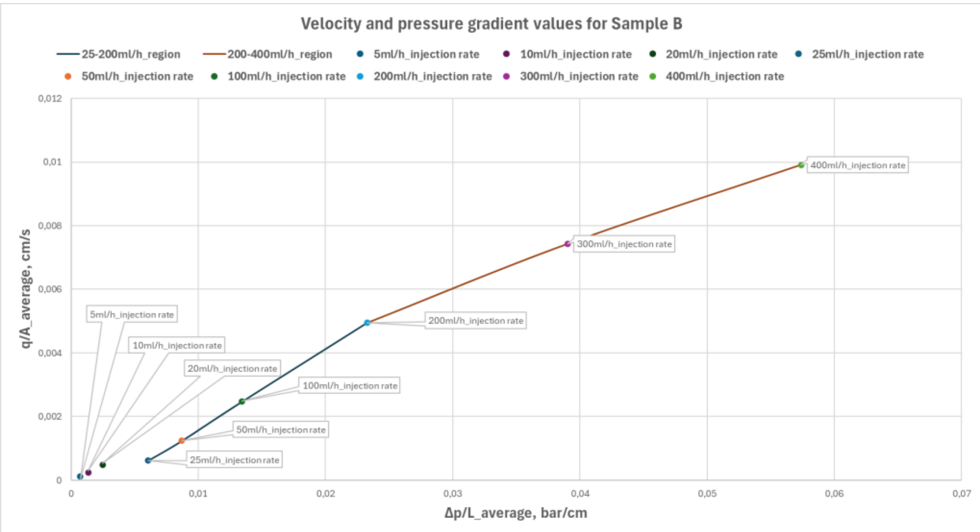

Figure 4
Velocity and pressure gradient values for Sample B

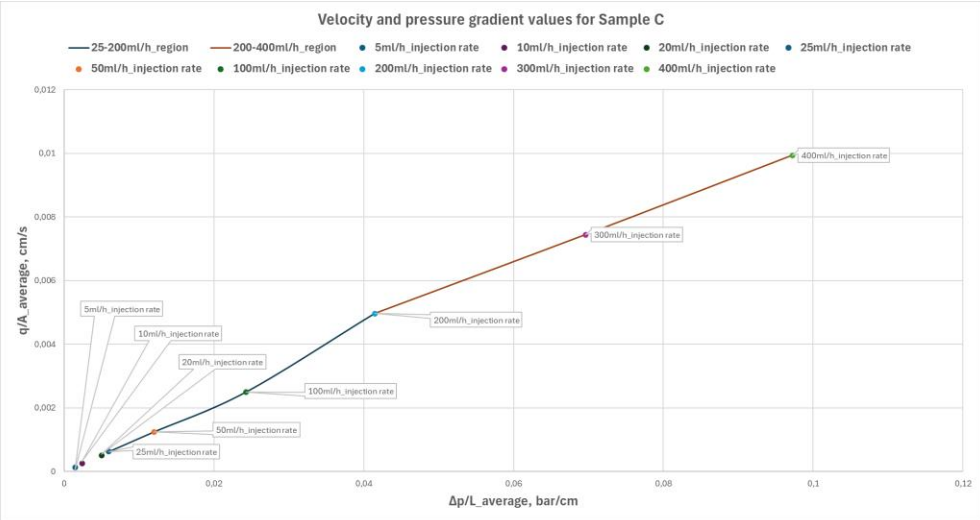

Figure 5

Velocity and pressure gradient values for Sample C

Results show that for all three samples three individual sections were present. At flow rates of 5, 10 and 20 ml/h presumably the so-called pre-Darcy region, at 25, 50, 100, and 200 ml/h the well-developed Darcy region, and covering the 200, 300 and 400 ml/h points deviated from the linear presenting pressure drops higher than those assumed by Darcy's law.

Although at first sight at Sample C the pre-Darcy region did not appear to be present, however, calculating the divergence from the Darcy section showed otherwise. The pre-Darcy region as many stated is a chaotic flow region in which the pressure drop effects are not yet established. Consequently, we discarded the section in the further analysis. Concentrating only on the linear and post-linear sections.

Numerous researchers have presented that Darcy's law has its limitations and can only be applied for a narrow pressure region where the pressure drop is mainly influenced by viscous forces. These flow conditions are primarily dominant in the reservoir section further from the wellbore area where Darcy's law at the elevated velocity does not apply even if laminar flow conditions are present. This transient pre-turbulent region is known as the Forchheimer region. Forchheimer's solution (Equation 4) by presenting and adding an inertial term to Darcy's equation had proven great correlations not only for the post-Darcy laminar but for the true Darcy region as well (Bagci et al. 2014), (Sedghi and Rahimi, 2011).

The Forchheimer equation is essential in reservoir-scale modeling and field-scale forecasting because it accounts for non-linear flow behavior that becomes significant at high flow velocities, especially in high-permeability formations, near-wellbore regions, and during enhanced recovery operations. Unlike Darcy's law, which assumes purely viscous (linear) flow, the Forchheimer model incorporates inertial effects, providing a more accurate estimation of pressure drops and flow rates under realistic field conditions. Neglecting these non-linearities can lead to underestimation of pressure losses and overprediction of production rates, ultimately reducing the reliability of reservoir performance forecasts and development planning.

Consequently, providing a solution for better estimations for pressure drop estimation at higher fluxes in the porous media while also proving sufficient in the low velocity Darcy region. Consequently, providing a more accurate method for pressure drop calculation at the wellbore sections and for different injections (such as fluid injection; underground gas storage etc.) type processes. We therefore suggested the implementation of the Forchheimer formula to be used instead of Darcy's during the permeability measurement to improve the reliability of the measurements while providing additional information for pressure drops at higher velocities

$$\nabla p = \frac{\mu}{k} v + \beta \rho v^2 \tag{4}$$

In his solution, the pressure gradient equals two pressure drop effects. The first part refers to where the viscous forces dominate (Darcy, laminar linear) and the second where at higher speeds the inertial forces are more dominant (Forchheimer, laminar flow but not linear relations). In the equation β (1/m) is Forchheimer's constant which quantifies how strongly the inertial effects contribute to the pressure loss. And its value changes according to the pore geometry, tortuosity and grain-size distribution of the porous material.

By applying its quadratic form for all speeds except the ones at the pre-Darcy region high correlations were found for all three measured samples (Figure 6–8) where the divergence of values calculated with both cases for the Darcy region was minimal (Table 5).

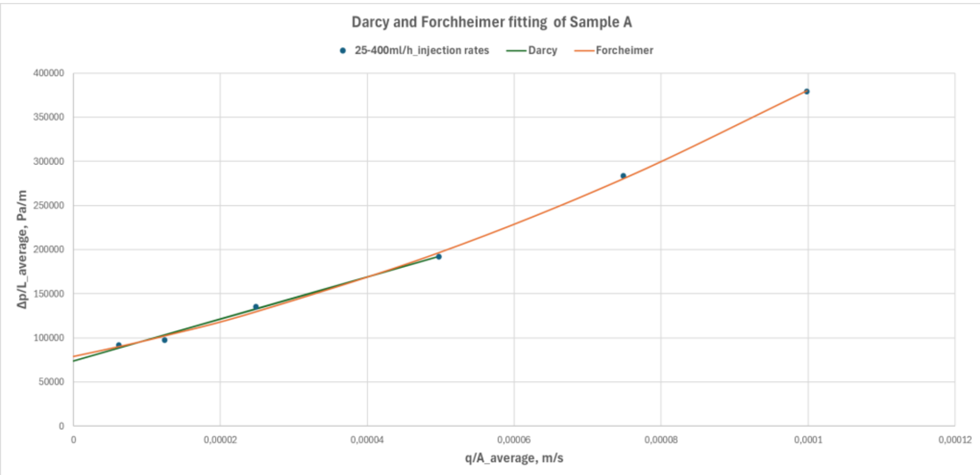

Figure 6

The result of Darcy and Forchheimer fittings for Sample A

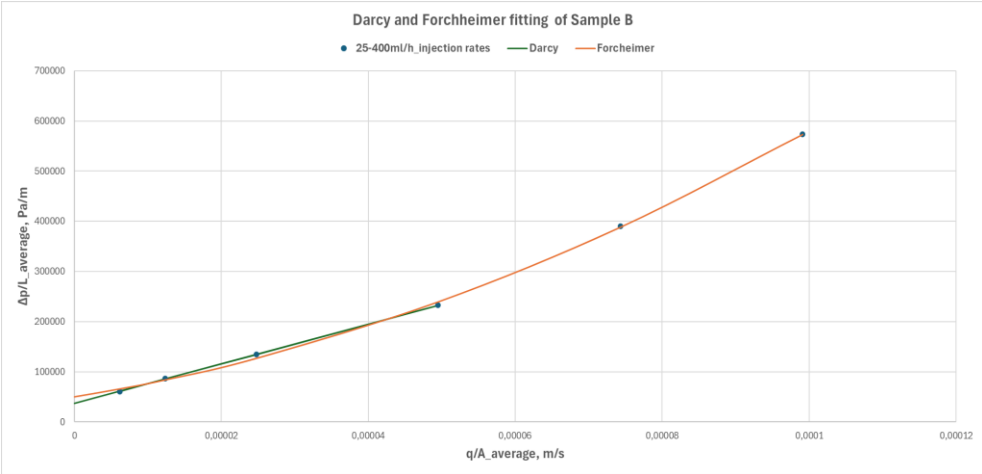

Figure 7
The result of Darcy and Forchheimer fittings for Sample B

Our conclusion after both methods was that the inflexion point was in all cases located at 200 ml/h where the maximum permeability value was measured and belonged to a permeability exceeding the original 100 ml/h value. This marked the true Darcy potential and the beginning of the Forchheimer region for all three selected samples. Also, the original assumption in the past that higher than 100 ml/h speeds would cause turbulent flow was proven false by the excellent regression on Forchheimer's equation.

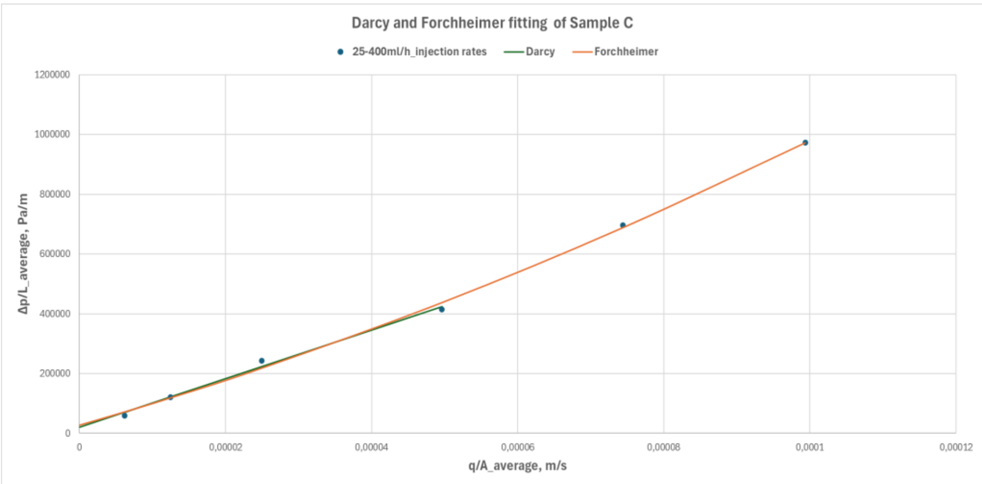

Figure 8
The result of Darcy and Forchheimer fittings for Sample C

Table 5

Divergence in the pressure drop calculated with Darcy and Forchheimer solutions

Solution	Sample A	Sample B	Sample C
Darcy regression	0.9921	0.9998	0.9919
Forchheimer regression	0.9987	0.9993	0.9979
Divergence at the laminar section, %			
25 ml/h_injection rate	1.9836	7.6182	1.5690
50 ml/h_injection rate	0.8621	2.0243	2.3605
100 ml/h_injection rate	2.3631	5.8081	2.1990
200 ml/h_injection rate	2.2915	2.9664	3.3134

The significance of this maximum permeability value in reservoir simulation practices is that it presents the lowest pressure gradient obtainable in the pore structure of the sample when fluids are moving on the rim of the wellbore's drainage area.

According to the test data we highly suggest the implementation of a new liquid permeability protocol where the permeability of such porous rock would be measured at multiple rates following the exact order of 50, 100, 200, 300, 400, and 200 ml/h. The second 200 ml/h step should be included to test if any porosity decremental effect had occurred during the higher velocity steps that would permanently damage permeability (Kozhevnikov et al., 2024).

4. Discussion and Conclusions

In this study, we critically evaluated and optimized the porosity and permeability measurement protocols employed in the petrophysical laboratory of the Research Institute of Applied Earth Sciences, with a focus on enhancing their relevance and reliability in the context of modern hydrocarbon reservoir characterization.

While the existing protocols aligned broadly with current standards, we identified key areas — specifically in pore-size distribution analysis, gas dynamic viscosity calculation, and pressure drop estimation — where targeted methodological refinements led to measurable improvements in accuracy. These improvements directly impact the precision of reservoir property assessments, such as fluid flow behavior and storage capacity, which are critical for reliable reservoir modeling and production forecasting.

Importantly, these enhancements were achieved without additional capital investment, by maximizing the capabilities of existing laboratory infrastructure. This demonstrates that even mature measurement workflows can yield significant performance gains when subjected to focused scientific scrutiny, ultimately contributing to more robust and cost-effective hydrocarbon reservoir evaluation.

Acknowledgments

Supported by the university research scholarship program of the Ministry for Culture and Innovation from the source of the national research, development and innovation fund.

References

Anovitz, L. M. & Cole, D. R. (2015). Characterization and analysis of porosity and pore structures. *Reviews in Mineralogy and Geochemistry*, January, Vol. 80, pp. 61–164.

API, 1998. *Recommended Practices for Core Analysis.* RP 40. II. Washington D.C.: API Publishing Services.

Bagci, Ö., Dukhan, N. & Özdemir, M. (2014). Flow regimes in packed beds of spheres from pre-Darcy to turbulent. *Transport in Porous Media*, Vol. 104, pp. 501–520.

Dócs, R. & Szunyog, I. (2024). Direct porosity measurement using single chamber gas pycnometers. *Geosciences and Engineering*, 12 (2), pp. 45–56.

Dotson, B. J., Slobod, R. L., McCreery, P. N. & Spurlock, J. W. (1951). Porosity-Measurement comparisons by five laboratories. *J. Pet. Technol.*, December, 3 (12), pp. 341–346.

Jiang, B., Xiao, Q., Shen, R. & Ding, Z. (2024). A new derivation for the apparent permeability model applied to the full Knudsen number range. *Transport in Porous Media*, Vol. 151, pp. 2241–2263.

Jimmy, X. L., Reza, R., Tobias, M. M. & Mohammad, S. (2020). Pore size distribution controls dynamic permeability. *Geophysical Research Letters*, 48 (5).

Kozhevnikov, E. V., Turbakov, M. S., Riabokon, E. P. & Gladkikh, E. A. (2024). Apparent permeability evolution due to colloid migration under cyclic confining pressure: On the example of porous limestone. *Transport in Porous Media*, Vol. 151, pp. 263–286.

Lawrence, A. M. & David, C. R. (2015). Characterization and analysis of porosity and pore structures. *Reviews in Mineralogy and Geochemistry*, 80 (1), pp. 61–164.

Luffel, D. L. & Howard, W. E. (1988). Reliability of laboratory measurement of porosity in tight gas sands. *SPE Formation Evaluation,* December, 3 (4), pp. 705–710.

Moghadam, A. A. & Chalaturnyk, R. (2014). Expansion of the Klinkenberg's slippage equation to low permeability porous media. *International Journal of Coal Geology*, Vol. 123, pp. 2–9.

Mohammed, K. S. (2025). *Klinkenberg effect: Laboratory study of the fluid inpedence of rock permeability.* University of Miskolc: s.n.

Rajib, A., Madland, M. V., Fred, B. & Aksel, H. (2012). *A study of sulphite ions-effects on aging and imbibition capillary pressure curve.* International Symposium of the Society of Core Analysts held in Aberdeen, Scotland, UK, 27–30 August, 2012, SCA2012-34.pdf, 12 p. (available online: https://www.jgmaas.com/SCA/2012/SCA2012-34.pdf).

Rapajic, I., Simic, S. & Süli, E. (2025). Modeling capillary rise with slip boundary condition: Well-posedness and long-time dynamics of solutions to Washburn's equation. *Physica D: Nonlinear Phenomean*, Volume 481.

Sedghi, A. M. & Rahimi, H. (2011). Adoption of Manning's equation to 1D non-Darcy flow problems. *Journal of Hydraulic Research*, 49 (6), pp. 814–817.

Singh, K., Camulli, H. & Bradley, J. (2024). Sediment size effects on non-Darcy flow: insights from Izbash equation and Forchheimer inertial coefficient analysis. *Hydrogeology Journal*, Vol. 32, pp. 1853–1871.

Tanikawa, W. & Shimamoto, T. (2009). Comparison of Klinkenberg-corrected gas permeability and water permeability in sedimentary rocks. *International Journal of Rock Mechanics & Mining Sciences*, 46 (2), pp. 229–238.

Geosciences and Engineering, Vol. 13, No. 2 (2025), pp. 32–48.
https://doi.org/10.33030/geosciences.2025.02.003

HYDROLOGICAL CAUSES AND CONSEQUENCES OF THE WATER INRUSH INTO THE PRAID SALT MINE, TRANSYLVANIA, ROMANIA

BALÁZS KOVÁCS
Institute of Water Resources and Environmental Management, University of Miskolc
balazs.kovacs@uni-miskolc.hu
https://orcid.org/0000-0002-3594-7355

Abstract: The Praid salt mine, Romania was flooded by the Corund Creek in May 2025, which changed the hydrodynamic and environmental conditions of the site. To provide an overview of the situation, we discuss the geological processes forming the salt diapir, highlighting its hydrogeological aspects. We also present the previous mining activities, and the most probable process of the water intrusion into the mine areas. Since a new situation arose as a result of the inrush of water, we analyze the hydrodynamic processes of the recent (flooded) state and we give an outline of future possibilities.

Keywords: *Praid, salt mine, flood, salt diapir, hydrodynamics*

1. INTRODUCTION

The Praid Basin lies at the eastern edge of the Transylvanian Basin and the Gurghiu Mountains and is part of the “Salt Region”. In a broader sense, the Praid Basin extends around the Salt Hill called Muntele De Sare (Sóhát) (Figure 1) with its three settlements of Praid (Parajd), Ocna de Jos and Ocna de Sus (Alsó Sófalva and Felső Sófalva). The small, triangle shaped basin, which is no more than 2 km wide and 7 km long, points southeast towards Corund city and connects to the Sovata Basin in the northwest through the Târnava Mică (Kis-Küküllő) river’s valley. In the middle of the Praid Basin lies the salt hill, with the highest point of 576 m above sea level, which is the exposed surface of a salt diapir, extending to a depth of 2.7–3.0 km. The Praid salt dome is one of the largest geological formations of its kind in Europe, with an elliptic horizontal cross-section with axes approximately 1200 and 1400 m long.

Salt mining dates back to the Middle Ages, but industrial deep mining only began in the 18th century, when the József Mine was opened in 1762 in the southwestern part of the hill, under the leadership of Austrian mining engineer Aladár Frendl (Horváth, 1998). Subsequently, mining cavities and chamber and pillar type excavations were developed on several levels down to a depth of 400–410 m below the surface.

Experts had already drawn attention to the danger of flooding of the mine areas in 2007 (Deák et al., 2007a), and in recent years there have been several minor water ingress incidents from the Corund Creek, which were stopped by water management experts after a short or longer period of time. In one such case, the lowest mine level was covered with more than 1 m of water, which allows us to predict the likely consequences in the current situation. It was interesting to note that the flooding caused only minor damage to the mine walls, with a few centimeters of dissolution during several months of flooding period.

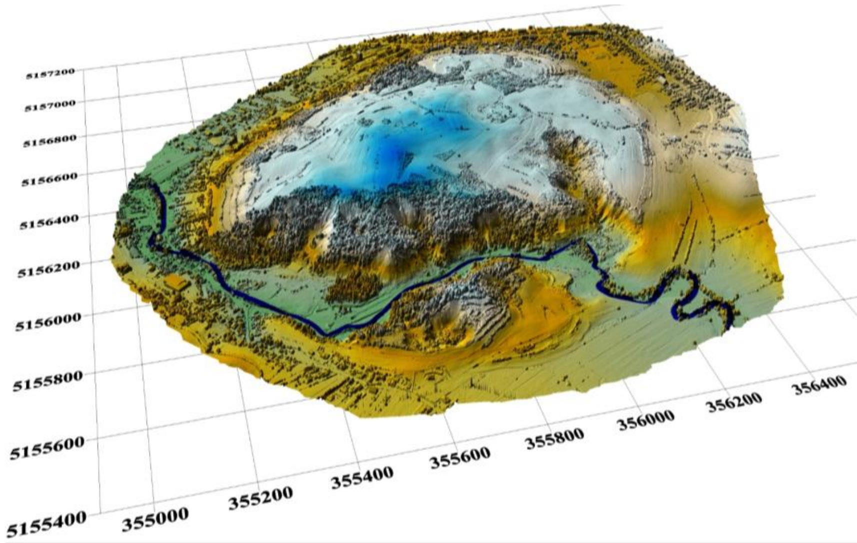

Figure 1
3D view of the Salt Hill (Sóhát, Muntele De Sare, units are given in meters)

Unfortunately, despite increasingly frequent warnings, the underground mine areas were not isolated from the Corund Creek. A flood situation developed on the Corund Creek at the end of May 2025, when the creek, which has a small catchment area and therefore capricious flow rate flux fluctuations (the creek is 19.6 km long, catchment area 137 km²; average slope of the riverbed 24.7 m/km, 10-year [10%] frequency water discharge 70 m^3/s, 100-year [1%] frequency discharge – 200 m^3/s based on data provided by Romanian Water Authority), a flood wave with a discharge of 60 m^3/s formed, resulting in a much stronger water intrusion into the so-called "Parallel mine" from the Salt Canyon direction on 27 May 2025, than previously. During the water intrusion, the entire water flow of the stream rushed into the mine cavities, resulting in the entire underground cavity system being filled to a level of 477 m a.s.l. (the level of the Corund Creek) by 29 May 2025. The salt miners tried until the very end to prevent the entire cave system from flooding by carrying out underground work, but the underground protective structures were washed away by the flood, so these efforts were unsuccessful. Fortunately, the flood did not claim any human lives.

2. METHODS

Elevation data for the larger area are from EUSTAT website (https://ec.europa.eu/eurostat/web/gisco/geodata/digital-elevation-model/eu-dem) using the appropriate cutoff from the 30 m horizontal and 1 m vertical resolution EU-DEM grid.

Large resolution Digital Surface Model (DSM) based on LIDAR photogrammetry recordings were made by the Babes-Bolyai University, Cluj-Napoca, Romania, with a horizontal resolution of 44.3 · 44.3 mm. Due to the need of high frequency DSM recordings (1-2 DSMs/day) there was no possibility for strong post processing and recalibrating of the images that lead to large elevation errors at locations with recordings from fewer drone positions and also in absolute elevation data. To reduce these errors, we performed a subsequent recalibration based on standalone buildings and other georeferencing points. Based on cross check of several images the relative error was decreased below approx. 10 cm, the absolute error below approx. 50 cm which made the DSMs usable. In most cases we used DSMs for comparative analyses that further reduced the errors.

The maps of underground openings and cavities were digitized from ancient mine maps by the support experts of the Romanian partners. Due to different and partially unknown local reference systems used at the surveys the boundary lines are converted to world coordinates by approx. 2-5 m lateral accuracy. The schematic cross section of the underground mine areas used in several explanatory figures was presented by SALROM specialist, Szilamér J. Kovács geologist without further citation.

All Corund Creek parameters were determined by the Romanian Water Authority based on the statistical evaluation of long-term measurements of water stages and flow rates. The sodium chloride concentrations were estimated based on electric conductivity measurements measured by in situ testing devices.

3. GEOLOGY OF THE SALT DIAPIR

The formation of the Praid salt deposits is summarized based on the works of István Horváth (1998, 2011) and the website www.salinapraid.ro. The Transylvanian Basin was formed by continuous subsidence at the end of the Cretaceous period and the beginning of the Paleogene period, while the neighboring Carpathian Mountains were uplifted.

The Praid salt dome itself was formed approximately 20-22 million years ago, during the Middle Miocene, Lower Badenian geological period. At that time, the shallow inland sea that had formed in the basin was separated from the ancient Tethys Sea, and the salt layers precipitated as a result of strong evaporation were deposited in the basin, which was sinking in the meantime. The current extent of the Transylvanian salt layer is approximately 16,200 km^2, with an average evaporite thickness of around 250 m (Figure 2).

The constant sinking of the basin resulted the formation of a nearly 5,000 m thick sedimentary formations during the subsequent geological eras, which was deposited on top of these salt layers. The salt mass therefore once lay deep below the younger layers, and the roots of the elliptical salt body in Praid is still at a depth of 2,700–3,000 m today. Under the significant pressure of the overlying rocks, the salt, like a plastic, dense liquid, was pressed towards the edges of the Transylvanian Basin. In the diapir fold zone, the plastic salt layers were compressed by enormous forces and pushed upwards towards the surface along existing fault lines in the form of salt domes. Where the salt folds could not rise to the surface, they became stuck at various depths and formed so-called crypto-diapirs.

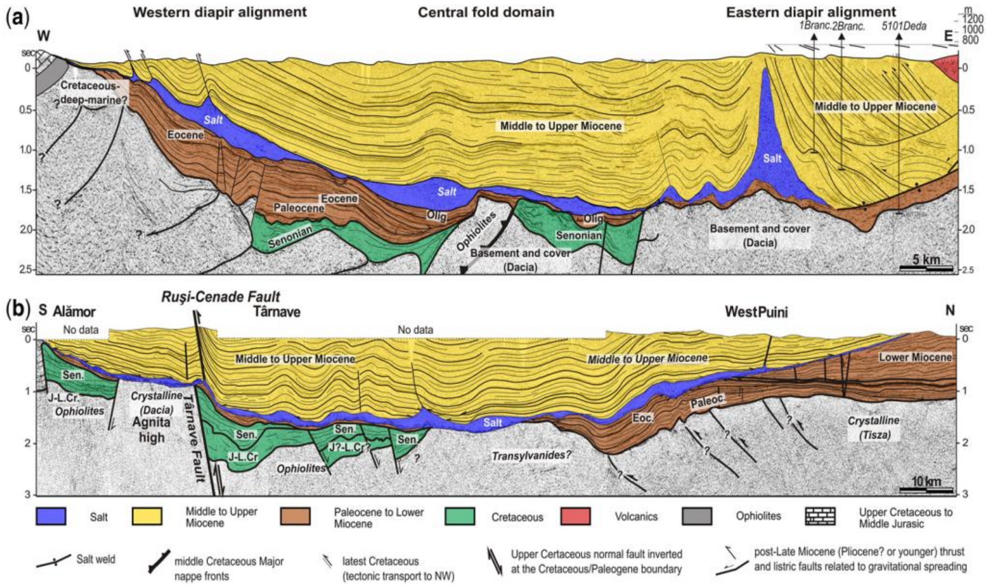

Figure 2

An E-W and N-S geological cross section through the Transylvanian Basin
(Tamas et al., 2025)

Paleogene sediments are found on the edge of the Transylvanian Basin, sloping towards the interior of the basin. Within this area lies a zone of diapiric folds, where deep-seated salt domes rose to the surface and broke through the younger sedimentary layers. In the central part of the basin, there is a region of wide, circular wave folds, known as domes, in whose porous rocks considerable natural gas deposits accumulated during the Upper Badenian, Sarmatian, and Lower Pannonian geological periods.

The four important layers of the Badenian sequence, from bottom to top, are the Badenian tuff, the Globigerina marl, the evaporites (salt and gypsum layers), and finally the shale and clayey marl layer, which is the cap rock of salt diapirs.

The Pleistocene strata are discordantly deposited on the Badenian strata. These are the products of post-Pliocene Harghita volcanism, i.e., volcanic agglomerates and breccias consisting of pyroxene and amphibolite elements and grayish tuffaceous binding material. The volcanic rocks are several hundred meters thick and form the main landforms surrounding the Praid Basin. The uppermost layer consists of Holocene sediments, which consist of river sediments, alluvial cones, sand and gravel deposits, soils, and carbonate deposits (e.g., Corund aragonite spring sediments).

One of the characteristics of the Praid salt deposit is that it contains interbedded rocks (crystalline schist, dolomite, quartzite, layered sandstone, clay schist, marl) and rock inclusions. The Praid salt is densely layered, with snow-white and dark gray salt layers alternating rhythmically, and the folds of the layer lines were clearly visible on the walls of the salt chambers.

As already mentioned, the Praid Salt Dome was formed during tectonic processes when the crumpled salt dome pierced through the younger layers of the Neogene strata. This process modified the water network of the basin. The emergence of salt hill caused hydrographic changes in the area where the Târnava Mică river and Corund Creek meet. The emergence of the salt diapir formed a barrier to the flow of the Corund Creek, while the larger Târnava Mică river was able to keep pace with the emergence of the salt dome and gradually deepen its erosional valley. The Corund Creek probably broke through the diapir area in the southern part through a valley-like depression formed by the collapse of salt karst cavities along tectonic lines, thus creating the Salt Canyon (Canionul De Sare, Sószoros) in Praid.

In the salt mountain zone, numerous salt karst phenomena can be observed on the surface, where smaller and larger, partly clay-lined funnels and depressions occur, resembling the karst phenomena of limestone regions: dolines, sinkholes, potholes, and karst fields. Some of the dolines and sinkholes are constantly forming and deepening, partly due to the infiltration of rainwater and partly due to the collapse of dissolution cavities formed by underground seepage. Some larger sinkholes are traces of ancient, irregular surface mining, in some cases irregular cavities left by Roman salt mining, or more recent illegal mines from which the local population stole salt during the prohibition period.

The sodium chloride content of Praid rock salt is between 94 and 98%. Unlike the salt deposits in the surrounding area, the productive salt body contains only very small amounts of gypsum and anhydrite (www.salinapraid.ro).

4. THE HISTORY OF THE PRAID SALT MINE, GEOMETRY OF UNDERGROUND MINE CAVITIES

The website of the Praid salt mine (www.salinapraid.ro) provides a detailed history of mining based on Horváth (1998), the most important details of which are as follows:

Systematic salt mining in Transylvania began during the Roman Empire, and after they abandoned it, the so-called surface "salt cutting" was continued first by the Avars and then by the Bulgarians. After the Hungarian conquest, King Stephen's salt transport ships regularly sailed on the Mures (Maros) River after 1003.

The Transylvanians had the ancient right to freely exploit natural resources, from which their free "salt right" originated, the continuous restriction and authorization of which depended on the historical balance of power. The earliest written record of salt mining is King Andrew II's 1222 charter of privileges for the German Order of Knights of "Barcaság", which granted them permission to operate salt-carrying ships on the Mures (Maros) and Olt rivers.

In 1405, King Sigismund of Luxembourg banned the opening of salt mines by local landowners, while in 1463, King Matthias confirmed the Transylvanians' right to use salt.

Until 1562, salt was the public property of the Transylvanian people, which meant that every household could obtain salt free of charge. Until 1562, salt was the common property of the Székely people, which meant that every Székely household could obtain salt free of charge, but this ceased after the suppression of the Székely uprisings, as King John II Sigismund confiscated the salt mine in Praid for the benefit of the royal treasury. The election conditions of Transylvanian princes Gábor Báthori (1603), István Bocskai (1605), Gábor Bethlen (1613), and György Rákóczi I (1631) included respecting the ancient freedoms of the Transylvanians and guaranteeing their free salt rights, but the free salt to which the Transylvanian people were entitled was only restored during the war of independence led by Ferenc Rákóczi II. Underground mining began in Praid in 1762, when the József Mine, which was geotechnically very stable and bell-shaped, was opened.

In 1787, the Praid salt mine became the property of the Vienna treasury. In 1864, the trapezoidal Parallel (Párhuzamos) Mine was opened, at the same time as the Nándor Mine was expanded. In 1898, the Erzsébet exploration tunnel began to be excavated in the northwestern part of Salt Hill. The medieval mining technique was reorganized after World War I, and in 1945, explosive salt mining was introduced. Between 1947 and 1949, the Dózsa György Mine was opened, but the Parallel Mine was still in operation until 1954. In 1972, work began on opening a new mining section in the north-eastern part of Salt Hill, but the work was abandoned due to quality indicators.

In 1978, new underground levels were created beneath the old mine chambers, with 12 m high, 20 m wide and 200 m long chambers, and later (in 1991) the development of the Telegdy Mine section began in the north-eastern part of the salt deposit with 16 m wide and 8 m high chambers, with square support pillars between them with a cross-section of 14 m × 14 m. The extent of the mine cavities throughout the entire Salt diapir is shown in Figure 3, for better presentation of the underground mining areas a 3D figure taken from the work of Deák et al. (2007b), is presented (Figure 4.)

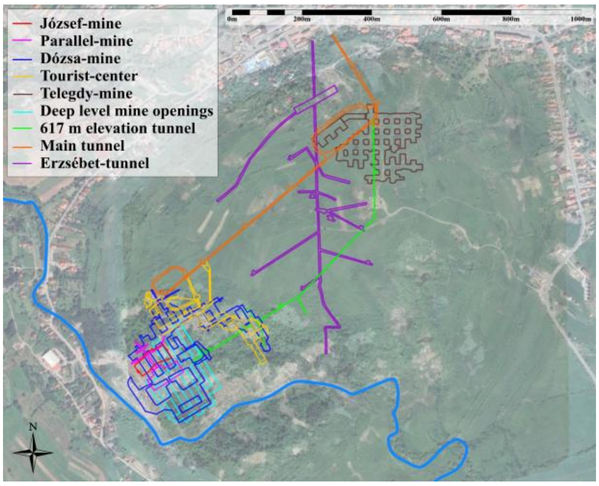

As Figures 3 and 4 clearly show, the bell-shaped dome of the József Mine and the pyramid-shaped ceiling of the Parallel Mine are closest to the surface. The former collapsed in a small area over time, which is why this area was covered with a larger roof structure on the surface to protect it from rainwater. There have also been minor collapses deeper in the mine. The wider pillar separating the József- and Parallel Mines collapsed in the middle section, and there have also been minor and major collapses in the ceiling of the parallel mine during water ingress. Most of these cavities were filled with concrete and clay fillings in an attempt to eliminate them.

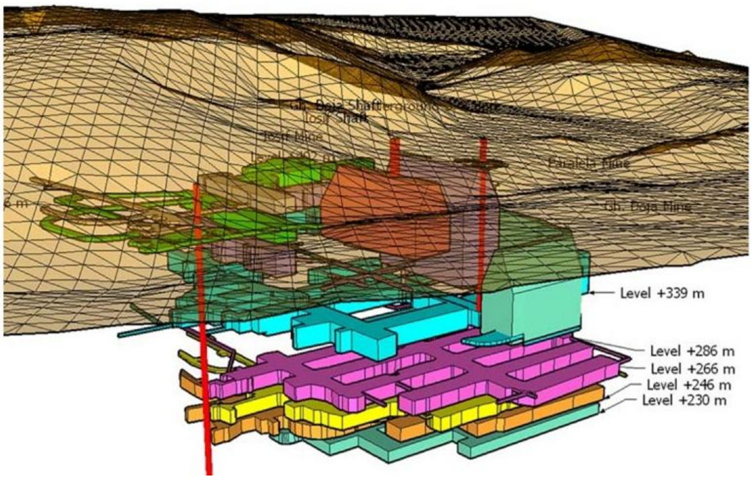

Figure 4
3D view of mine openings in the Southern part of the Salt Hill (Deák et al., 2007b)

5. PROCESSES OCCURRING DURING WATER INRUSH, HYDROGEOLOGY AND HYDRAULICS OF THE SYSTEM, STABILITY AFTER FLOODING

Over the past decades and centuries, numerous dissolution cavities and cavity systems have formed in the salt dome. Some of these were formed by water infiltrating along the fault systems in the area and, due to prolonged dissolution processes, could be as deep as 10–15 m below the surface (these are patterns of natural salt karstification).

The dissolution cavities were tapped through the vein systems by the mine cavities, and periodic "sweating" and seepage in the ceiling zones of the mines seemed natural over time, which the miners continuously pumped out from the mine areas. Occasionally, these slow dissolutions caused minor or major collapses, one of the largest of which was the collapse of part of the ceiling of the József Mine. These cavities were fed partly by sinkholes formed on the left bank of the Corund Creek and partly by fresh water slowly seeping along the veins and cracks crossing the stream, causing a continuous dissolving of salt.

In addition to this natural cavity formation, however, dissolution cavities also formed at the contact surface of the salt dome and the alluvium of the Corund Creek, as a kind of discontinuity, but these were of minor importance before the flood of the mine.

When the water broke through, the stream found its way to the former karstic cavities, where the continuous inflow of fresh water increasingly dissolved the salt formations, widened the cracks, and then broke through walls of the existing cavity system leading to the Parallel Mine's roof level (Figure 5). At first, this process only led to a low flow towards the mine, but with the continuous dissolution of the cavities, in its final state it was able to swallow the total discharge of the creek, which at that time was approximately 60 m^3/s.

This intruding water first spread across the floor level of the Parallel Mine, then poured down deeper and deeper levels along shafts, inclining shafts, blind shafts, and previous drill holes (Figure 6). In this phase, not only the dissolving effect of fresh water, but also the mechanical force of the turbulently flowing water destroyed the salt rocks. According to the miners, the water rushing downwards dissolved the salt in a zone several meters wide, even exceeding 10 m in diameter, along the drill holes as it flowed towards the deeper levels. Once it reached the deepest levels, the water filled the mine from the bottom up, causing, for example, the wooden support structures of the Parallel Mine were crushed into the adjacent mine chambers, confirming that the water ingress occurred through the Parallel Mine and that any inflows into the József Mine from the surface were negligible during the water ingress process.

As a result of the water ingress, by 29 May 2025, the entire underground cavity system had filled up to the level of the Corund Creek, i.e., 477 m a.s.l. The total volume of the mine cavities can only be estimated with a high degree of inaccuracy based on the time required for flooding and the estimated average discharge of the creek. According to those calculations a total volume mine cavities of 4–7 km^3 was determined.

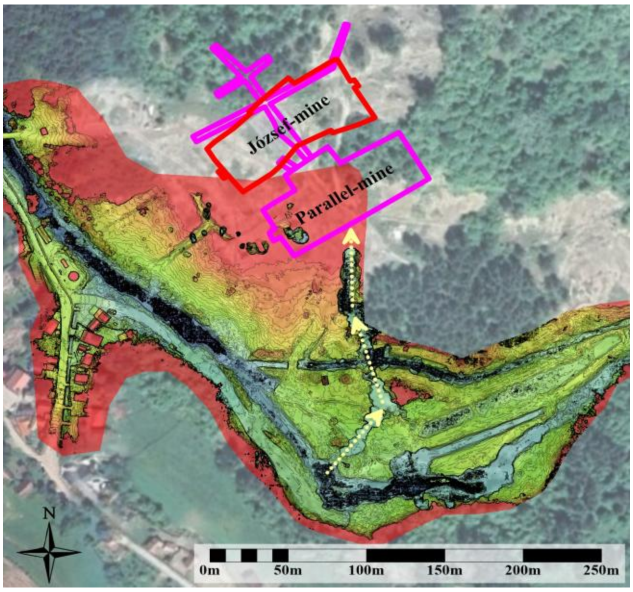

Figure 5
The direction of freshwater inflow can be easily traced on the surface relief based on the collapse of underground cavities (evaluation based on photogrammetry-based [LIDAR] DSM by Babes-Bolyai University, Cluj-Napoca made on 13. 06. 2025)

The fresh water entering the mine gradually dissolved more and more salt through the dissolution and erosion processes described above, and also dissolved the salt stored in the area of the former and current mining cavities. The salt deposits stored in the mine chambers are significant in that the dissolution of the mined powder and debris-like salt is much faster due to its large surface area than the dissolution of the salt walls along the pillars, which could have significantly reduced the rate of dissolution from the pillars.

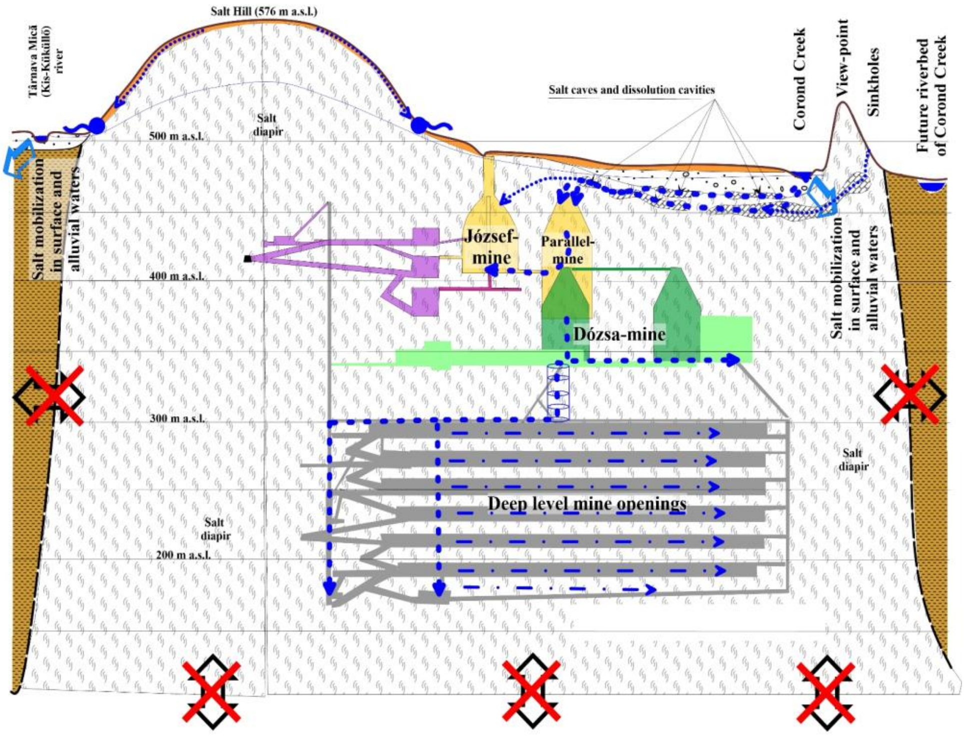

Figure 6

Schematic representation of the flooding of the studied salt mine

The saturation concentration of sodium chloride is 359 g/dm^3 at 25 °C, which varies only a little with temperature (375 g/dm^3 at 60 °C) and pressure. This is important because the temperature in deeper mine cavities is higher than near the surface, but at the same time, no significant change in solubility is to be expected. Considering the total filled volume of 4–7 km^3, a total of 1.4–2.5 million metric tons of salt was dissolved in the mine in a few days. According to online sources (Széchely, 2015), the mine's annual salt production was 120–150 thousand metric tons, which means that in 3-5 days, the salt equivalent of 10–20 years of production dissolved in the mine cavities. However, the density of saturated NaCl salt solution is 1170 kg/m^3, which is 17% higher than that of water, which is significant in terms of the hydrodynamics and stability of the area after filling.

According to measurements, the salt solution reached saturation in the mine chambers within a few days (by 5 June 2025) in the József Mine and in 3 weeks it the Telegdy Mine (Máthé et al., 2025) at the farthest and highest point from the water ingress point. From this point on, no further dissolution of salt could occur at the contact surfaces with the saturated salt solution. However, salt dissolution does occur after filling, wherever the saturated solution is diluted due to the infiltration of fresh water into the mine areas. Since the amount of water in the mine is nearly constant (corresponding to the current water level of the Corund Creek), a quantity of saturated salt solution corresponding to the amount of fresh water currently entering the mine escapes from the mine cavities, primarily into the Corund Creek, maintaining higher salt concentrations than before on a permanent basis.

The most typical inrush pathlines can be determined based on surface subsidence. The map shown (Figure 7) is based on topographical surveys conducted by Babes–Bolyai University on 4 and 14 June 2025, which, due to the lack of postprocessing, remain somewhat inaccurate but are nevertheless representative. The changes in terrain clearly show the main direction of the water intrusion, as well as the alternative stream beds created during the defense measures, which are also capable of directing water in this main direction. In addition, the eastern parts also show the zones where the increasingly saturated waters from the near-surface mining areas seep out. These zones transport the waters partly from the Parallel Mine and partly from the József Mine towards the Corund Creek. The driving force behind the seepage is the water stage gradient (slope) in the Corund Creek, which reaches 2-3 m in the area (between the two ends of the Salt Canyon), depending on the water level, but also exceeds 1.5 m in the mining area. This driving force induces leakage towards the mine areas on the upstream side and discharges the mine cavities on the downstream side, which induces continuous freshwater infiltration, salt dissolution and then saltwater outflow.

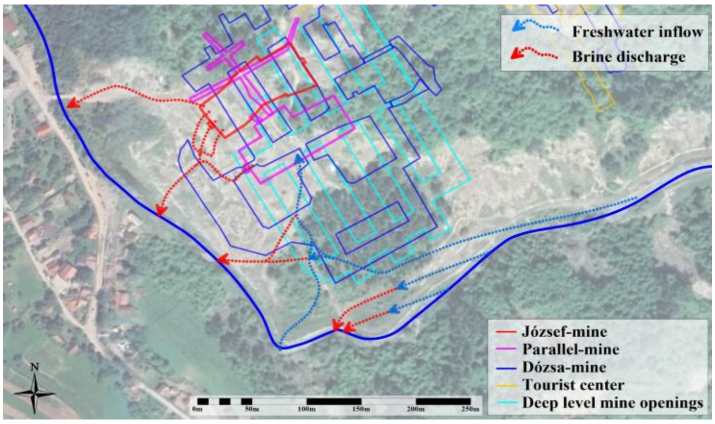

Figure 7

The recently possible directions of freshwater recharge and salty water discharge based on the surface relief survey of underground cavities (evaluation based on photogrammetry-based DSM by Babes-Bolyai University, Cluj-Napoca made on 14. 06. 2025)

This also means that until the water of the Corund Creek is completely isolated from the mining areas, continuous salt dissolution will occur partly from the alluvium of the Salt Canyon area and partly from the mine cavities (Figure 7).

In addition to this constant slow salt leaching, fluctuations in the water level of the Corund Creek also generate salt yields, as the water level in the mine cavities follows the changes in the water level of the creek with a delay of at most half an hour to an hour, so that during floods, fresh water pushes towards the mine, and during low water levels, salt water seeps out of the mine cavities.

The salt loss intensity from the mine area can be estimated based on the actual discharge, sodium and chloride ion concentrations of the Corund Creek and the Târnava Mică river. The sodium and chloride concentrations can generally be determined based on electric conductivity (EC) measurements. Assuming that the change in EC is caused solely by the dissolution of sodium chloride, then 0.336 times the conductivity measured in µS/cm is equal to the chloride content in mg/dm^3, and keeping in mind that mainly sodium chloride is dissolved, then based on the molar mass ratio of Na and Cl atoms, the sodium ion concentration is 64.8% of the chloride ion concentration and the "concentration" derived from the leached NaCl is 1.366 times the chloride ion concentration. The total yield of sodium chloride dissolution from the mine can be calculated as the product of brine concentration and the discharge of the creek or river.

Based on the salt loss intensity calculations, it appeared that the initial salt dissolution rate of 1300 t/d at the end of May (just after the mine flood) had decreased to 170 t/d due to the initial measures and the trend of decreasing Corund Creek discharge and water levels, which was temporarily and suddenly raised to 3900 t/d by riverbed relocation and related construction works. This large excess dissolution caused the damage to wildlife observed in the Târnava Mică river (Máthé et al., 2025).

Máthé and his co-authors (2025) simultaneously measured the EC of the Corund Creek and the Târnava Mică river and found that the concentration of the Târnava Mică river decreased only to nearly one-fifth (21.3%) due to dilution. The brine concentration of the Corund Creek decreased from 10 g/dm^3 to 3 g/dm^3 during the initial period mentioned before, which suddenly increased to a concentration of 30–80 g/dm^3 during the initial construction works and relocation of riverbed, then decreased to between 8 and 5 g/dm^3 during the period of June 20 and 30 2025, and later fluctuated between 2–6 g/dm^3 until July 20, based on the conversion of EC data available in public communications (Maszol.ro, Szekelyhon.ro, ZiarHarghita.ro, HargitaNepe.ro) referring to announcements of Romanian authorities. The magnitude of the mentioned concentrations is well illustrated by the fact that the average salt content of seawater is 35 g/dm^3, meaning that during peak periods, the concentration was 2-2.5 times higher than that value. Due to the nature of calculations, the mentioned values are only estimates. Máthé and his co-authors (2025) stated that above 1 g/dm^3 sodium chloride concentration there is a relevant effect on the biodiversity of invertebrate fauna, and prolonged brine concentrations exceeding 1.5 g/dm^3 caused the complete extinction of macroinvertebrates and fish populations along the affected sections of the Corund Creek and the Târnava Mică river. Drinking water standards prescribes the chloride concentration below 250 mg/dm^3 therefore all surface water discharge operations for public water supply for over 40 thousand inhabitants downstream from the mouth of Corund Creek had to be stopped (Rákóczi, 2025).

There is another interesting aspect to the hydrodynamics of the system, namely, due to the increase in density caused by the dissolution of salt, a zone with a higher potential than the surrounding area is formed in the mine cavities during dissolution, given that the hydraulic, i.e., seepage potential depends not only on the reference height of the water level but also on the density of the liquid.

As long as the salt continues to dissolve, the continuously increasing potential levels within the mine cavities are higher than their surroundings, which can be balanced out if the salt leaks out from the mine cavities through existing cracks and not completely closed fracture zones. As these waters are nearly saturated, their further dissolving effect is negligible, but they do represent a form of underground salt transport. This phenomenon may result in a local increase in the electrical conductivity of groundwater and, presumably, in its sodium and chloride content upstream in the Târnava Mică river's alluvial deposit, in the area north of Salt Hill.

Once the hydraulic balance of the mine cavities and the surrounding area is established, this salt transport ceases due to the lack of driving force. All this confirms that isolating the Corund Creek from the mining areas is critical for the environmental condition of the area, because until then, water inflow, saltwater seepage and the continuous disruption of the hydraulic balance will continue, affecting not only the Corund Creek valley and, through it, the lower reaches of the Târnava Mică river, but also the zone along the Salt Hill in the Târnava Mică valley upstream from its mouth.

However, these dissolution processes following the filling of the mine cavities only affect the uppermost zones of the shallower mine cavities near the surface, as the higher-density, saturated salt solution fills the deeper mine cavities, so no dissolution processes are currently taking place at greater depths.

The formation of the salt diapir described above and its existence over millions of years mean that the diapir is completely isolated from the groundwater laterally and from the depth below the diapir (partly due to the surrounding clays and marls, and partly due to the soluble but surprisingly impermeable salt rocks), so that the saturated water containing sodium chloride that seeps into the deeper mine cavities cannot move either sideways or downwards. Accordingly, these deeper mine cavities are stable, as further salt dissolution is theoretically impossible and the cavities previously filled with air are now filled with a high-density saturated salt solution.

This salt solution not only does not break down the walls of the mine cavities, but also supports them with its pressure. Assuming a water column height of 300 m in deep mines due to flooding, this supports the walls with a pressure of 30 bar in the case of pure water, but over 35 bar in the case of brine (Figure 8). Since these walls were stable even under atmospheric pressure, it stands to reason that they will not collapse even with an additional 35 bar of support. As it approaches the surface, this supporting effect naturally decreases, but strangely enough, the current situation is definitely more favorable from a geotechnical (stability) point of view than the situation prior to the water inrush. For the reasons mentioned above, in the deeper mine areas (i.e., everywhere except the József and Parallel Mines), dissolution and deterioration of stability conditions are not to be expected in the current situation.

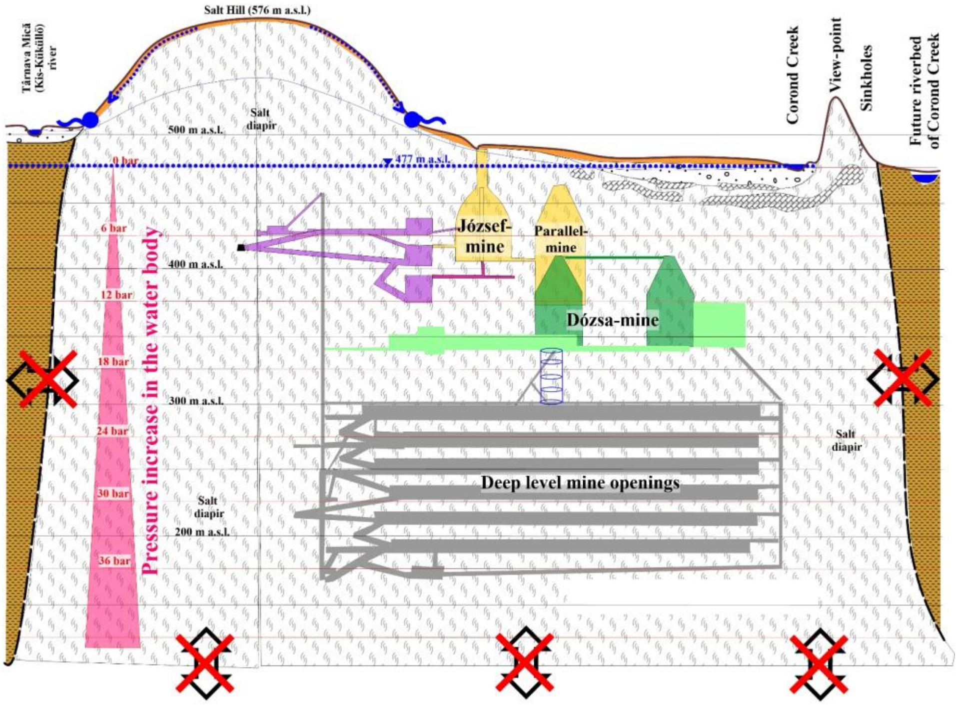

Figure 8
Explanatory chart of elevated liquid pressure in the flooded mine

Unfortunately, there may be minor or major collapses in the Parallel and József Mines, which are connected to or may be connected to surface waters, and, with very low probability, in the Dózsa György Mine due to its more direct connection to the surface and the Parallel Mine through the shafts. Dissolution near the surface is gradually eroding the salt rock of the dome and ceiling of the Parallel Mine and, to a lesser extent, the József Mine, which, as it thins, is less and less able to bear the weight of the rock above it, which could lead to collapse.

Fortunately, as Deák et al. (2009) have demonstrated with triaxial measurements, salt rocks behave differently from other rocks when bearing loads. In general, rocks undergo continuous deformation as they bear increasing loads, and then, after failure, their load-bearing capacity decreases suddenly and radically, with up to 90–95% of their load-bearing capacity being lost.

Salt rocks, on the other hand, behave differently. In the case of samples from the Praid salt mine, despite the aforementioned layering and contamination, they take loads slowly and, after reaching a maximum, are still able to bear and retain loads, i.e., most of their load-bearing capacity is retained while the salt rock undergoes deformation. The slower the loading, the greater the residual strength of the rock, and the more it is able to undergo the deformation most appropriate to the current stress state. For all these reasons, in the event of slow weakening of structures and slow increase in loads, salt rocks will be able to take on additional loads, which minimizes the possibility of sudden major collapse. Rather, slow, trend wise minor collapses can be expected.

6. Discussion and Conclusions

Solving the problems arising from the unfortunate flooding of the Praid salt mine is an ongoing challenge for hydrologists, hydrogeologists, geotechnical engineers, and environmental experts. In this study, we presented the mine and the events that took place, summarized the geological and hydrogeological conditions, and based on this, we presented the hydrodynamic and salt transport processes that occurred after the flooding.

Initial analyses predicted the rapid collapse of the mine cavities and the formation of a salty lake at the site of the mine. In addition, it was apparent that the salt content of the Corund Creek was no longer tolerable for higher organisms, and even the water quality of the Târnava Mică river was periodically intolerable for fishes and other animals. Furthermore, the drinking water supply of the settlements downstream nearby the Târnava Mică river became impossible, as the water extraction facilities had been installed on surface waters that had previously been of adequate quality. In addition to the salt content of surface waters, the salt content of groundwater has also increased locally in alluvial deposits connected to the salt dome, which also threatens the long-term use of groundwater. All these problems can be traced back to the formation and persistence of water circulation between the Corund Creek and the salt dome (Figure 7).

Based on our analyses, the deeper levels of the flooded mine have reached a new state of equilibrium, which means that only very slow and negligible changes can occur in these areas. However, the shallower mine areas, especially the area of the Parallel Mine's roof structure, to a lesser extent the cavities near the surface of the József Mine, and least of all the parts of the Dózsa Mine close to the aforementioned mines and the shaft, are exposed to a continuously increasing level of risk over time. In these areas, fresh water seeps into the mine cavities, partly due to the fall of the Corund Creek and partly due to the driving forces caused by changes in the water level of the stream, which has a dissolving effect there, reducing the load-bearing capacity of the supporting pillars and structures, which partly causes a risk of collapse and partly causes civil protection problems through the leakage of saturated salt water corresponding to the volume of infiltrating fresh water, as well as the aforementioned environmental protection and water supply difficulties.

This dissolution of salt can only be prevented by isolating the waters of the Corund Creek from the mining areas, the ultimate solution being to divert the Corund Creek outside the Salt Hill (Figure 9). Once the majority of fresh water, including rainwater, has been excluded, decisions can be made regarding the future of the mining areas. Based on our current knowledge, there are no scientific obstacles to the partial or complete drainage of the mining areas after the isolation of surface waters from the mine. The partial drainage of the mining areas would also be important due to the elimination of outward hydraulic potential levels, but at the same time, if the experience is favorable, it would also be possible to drain the higher-elevated Telegdy mine and the tourist center. The treatment and desalination of the extracted salt water pose a serious challenge, and an economical solution needs to be developed.

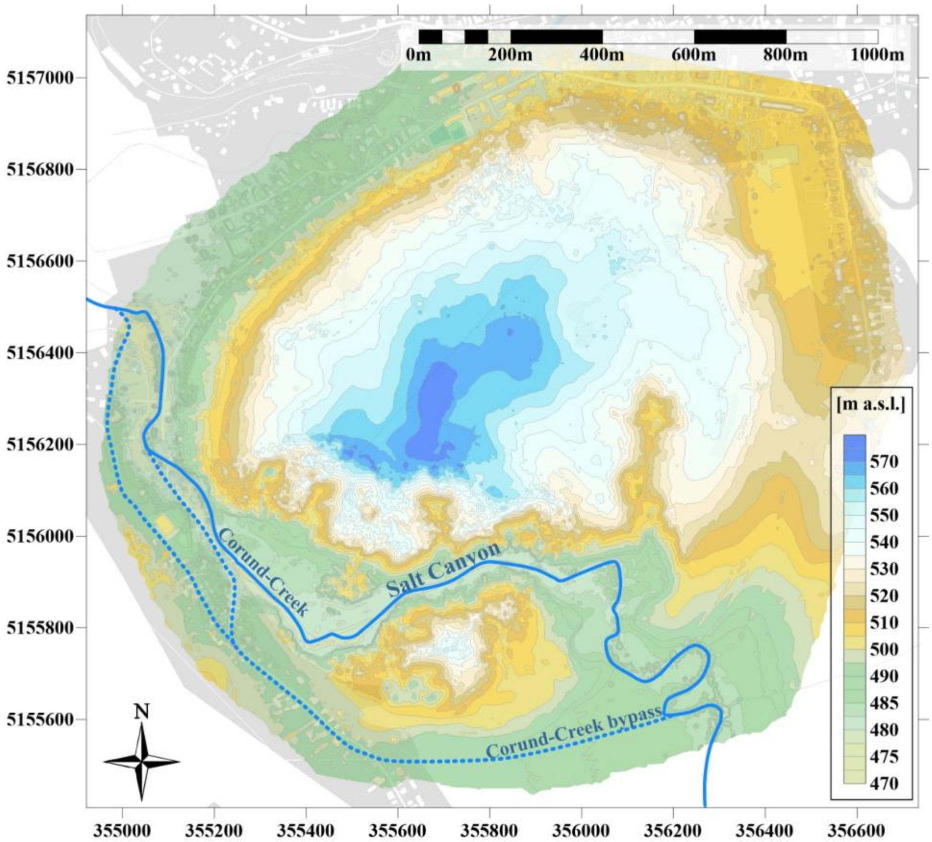

Figure 9
A possible track of Corund Creek bypass

As the current situation is clearly unfavorable for the mine, the population, and the natural environment due to the continuous leaching of salt and the reduction in the load-bearing capacity of the mine cavities, measures should be taken as soon as possible to exclude fresh water. Over time, the impact on the environment, the population, and society will increase, and the measures to be taken to mitigate them may become increasingly complex and costly.

ACKNOWLEDGMENTS

The author had the opportunity to gain a more detailed understanding of the region and the issues involved through the work of an international expert group (EU CPT) organized by the EU Civil Protection Mechanism (EU CPM) following Romania's request for assistance, consisting of four Hungarian, two German, one Dutch, and one Spanish expert, as well as a Romanian professional liaison. I would like to take this opportunity to thank the EU ERCC, the National Directorate General for Disaster Management in Hungary, the Hungarian and foreign experts involved in the expert work, the Romanian official bodies, ministries, and companies for their goodwill and helpful cooperation. I would also like to highlight the support and work of the Technical University of Cluj-Napoca, the Babes-Bolyai University of Cluj-Napoca and the University of Petroșani, as well as SALROM-Salina Praid, Grupul GeoPraid, the Romanian Water Authority, and the Romanian Disaster Management Agency, who, with tremendous effort over a few days, provided the systematic information and data necessary to understand the behavior of the system.

This paper has been prepared in accordance with the EU ERCC publication guidelines and is therefore based solely on publicly available information from newspaper articles, website information, official communications, professional publications, and basic scientific knowledge.

REFERENCES

Deák Gy., Mihai S., Deák Ş. E., Oancea I. (2007a). How to prevent the risk of surface water intrusion in the old Praid salt mines (Romania). *Proc. of IMWA Symposium 2007: Water in Mining Environments*. R. Cidu & F. Frau (eds.). 27th–31st May 2007, Cagliari, Italy, pp. 65–69.

Deák Gy., Mihai S., Deák S. E., Oancea I. (2007b). Addressing the Risk of Surface Water Intrusion in Old Romanian Salt Mines. *Mine Water Environ*, 26, pp. 251–255. https://doi.org/10.1007/s10230-007-0011-7

Deák Gy., Deák Şt., Agioutantis Z., Mavrigiannakis S. (2009). Assessment of rock salt micro-properties using PFC-2D modelling. *Sustainable exploitation of natural resources – Proceedings of the Third International Seminar ECOMINING – Europe in 21st Century*, Milos Island, September 4–5, 2009. Greece. pp. 126–133.

Horváth I. (1998). *A székely sóbányászat rövid története*. (Short history of the Transylvanian salt mining [in Hungarian]) pp. 1–80. Parajdi Sóbánya, Parajd.

Horváth I. (2011). A Parajdi medence földtana II. (Geology of the Praid basin (in Hungarian)) Zöld sarok. *Sóvidék*, 3. évf., 2. sz. (2011. december) pp. 30–33. https://epa.oszk.hu/01900/01975/00005/pdf/EPA01975_sovidek_2011_03_01_30-33.pdf

Kovács B. (2025). Hydrogeological (hydrodynamic) aspects of the water intrusion into the Praid salt mine (in Hungarian). *Proceedings of the 19th International Scientific Conference on Mineral Waters of the Carpathian Basin*, Kosice, Slovakia, 2025 august. pp.17–26.

Máthé I., Imecs I., Nagy A. A., Kelemen A., Zsigmond A. R., Szép S. (2025). A parajdi bányaelárasztás következtében megnövekedett sótartalom hatása a Kis-Küküllő élővilágára (Effects of increased salinity from the flooding of the Praid mine on the biota of the Kis-Küküllő river) (in Hungarian). *Proceedings of the 19th International Scientific Conference on Mineral Waters of the Carpathian Basin*, Kosice, Slovakia, 2025 august. pp. 27–45.

Rákóczi K. (2025). Sótalanítás – A Kis-Küküllő mentén még mindig nem iható a csapvíz, (Desalination – Tap water still undrinkable along the Târnava Mică river) (in Hungarian). *Maszol.ro portal*, https://maszol.ro/belfold/Sotalanitas-A-Kis-Kukullo-menten-meg-mindig-nem-ihato-a-csapviz (last accessed: 05. 09. 2025)

Salina Praid (2025). A parajdi sóbánya bemutatása (Történelem, Kitermelés, Geológia, Földrajz) (Intorduction to Praid salt mine – History, Excavation, Geology) (in Hungarian) – (Compiled by I. Horváth). https://www.salinapraid.ro/ (last accessed: 04. 09. 2025)

Széchely I. (2015). Parajdi szintváltások. *Erdélyi Napló*, https://erdelyinaplo.ro/aktualis/riportok/parajdi-szintvaltasok (last accessed: 04. 09. 2025)

Tamas, D. M., Dohan, D., Barabasch J., Tamas A., Schleder Zs., Krezsek Cs., Urai J. L. (2025). A review of salt tectonics in Romania’s Transylvanian Basin and implications for energy transition. *Geological Society*, London, Special Publications, https://doi.org/10.1144/sp555-2024-9

Geosciences and Engineering, Vol. 13, No. 2 (2025), pp. 49–64.
https://doi.org/10.33030/geosciences.2025.02.004

SOME ASPECTS OF THE RADIO-MAGNETOTELLURIC METHOD AND INSTRUMENTATION DEVELOPMENT

LÁSZLÓ VINCZE
Department of Geophysics, University of Miskolc
laszlo.vincze@student.uni-miskolc.hu
https://orcid.org/0000-0002-9272-0560

Abstract: In recent decades, the demand for shallow geophysical methods and instruments has changed significantly. Today, there is a need for methods and instruments that can provide a large amount of accurate measurement results in a short time, which are suitable for developing effective inversion procedures. Only contactless methods can meet the speed requirement. The measurement technique is significantly simplified if we can use a signal source that is of natural origin or an artificial source created for other purposes (e.g. radio transmitters). The radio-magnetotelluric method (RMT), which can be considered an extended variation of the popular very low frequency (VLF) method in terms of frequency range, is exactly such a method. Another advantage is that the created field can be considered a plane wave, thus simplifying the data processing and interpretation procedures. This study presents a brief history of the development of VLF-RMT methods, the evolution of instruments, the development of processing methods, the characteristics of modern inversion methods, and then summarizes the aspects of designing a modern RMT instrument.

Keywords: *VLF, RMT, software defined radio, SDR, digital signal processing, DSP*

1. INTRODUCTION

In the early 1960s, electromagnetic methods were already in full use in exploration geophysics. The theory of magnetotellurics – where the electromagnetic field serving as the basis of the method can be considered as a plane wave – was summarized by Cagniar (1953). In Canada, the Scandinavian countries, mainly Sweden and Finland, and the Soviet Union, induction electromagnetic (Slingram) methods were used to investigate well-conducting massive sulphide ore bodies. The behavior of radio waves and their geological utilization have been studied for a long time by several researchers: Wait (1953), Dosso (1962), Dosso (1965a, 1965b). The theoretical foundations are summarized by McNeil and Labson (1991).

The antennas of VLF and LF radio transmitters can be considered as short vertical electric monopoles on a horizontal conductive plate. Electromagnetic waves propagate directly, as surface waves at the earth-air interface and by reflection from the ionosphere. Since the reception location is usually a long distance, multiples of the wavelength, from the transmitting antenna, the electromagnetic field there can be considered as a plane wave, similar to magnetotelluric phenomena, therefore the procedures developed there can be applied to the VLF and RMT methods as well. Almost regardless of the angle of incidence at the air-earth interface, due to the high refractive index, the plane wave travels downwards perpendicular to the surface in the subsurface layers. Moving downwards, depending on the resistivity of the medium, the electromagnetic field strengths decrease exponentially. The penetration depth, or skin depth, is the depth at which the amplitude measured at the surface decreases by 1/e (approx. 37%)

$$\delta = \sqrt{\frac{2}{\mu\sigma\omega}} = 503\sqrt{\frac{\rho}{f}} \tag{1}$$

where δ is skin depth, μ is magnetic permeability, σ is conductivity, ρ is resistivity, ω is angular frequency, f is frequency.

Table 1

Skin depth at different frequencies and resistivities

f \ ρ	10 Ohmm	30 Ohmm	100 Ohmm	300 Ohmm	1000 Ohmm
15 kHz	**13 m**	**22.5 m**	**41.1 m**	**71.2 m**	**129.9 m**
30 kHz	**9.2 m**	**16 m**	**29.1 m**	**50.4 m**	**91.9 m**
75 kHz	5.9 m	10.1 m	18.4 m	31.9 m	58.1 m
155 kHz	4.1 m	7 m	12.8 m	22.2 m	40.5 m
240 kHz	3.3 m	5.7 m	10.3 m	17.8 m	32.5 m

It can be seen from Table 1 that the narrow VLF band (bold), depending on the resistivity, allows a depth penetration of a few tens of meters. In the case of bedrock with high resistivity, the penetration depth can reach 100 m depth-selective evaluation of the measurements, even if we measure at all possible frequencies, is only possible to a limited extent. By supplementing the VLF measurements with LF range transmitters (RMT), more possibilities are available for the layer separation with inversion.

At a measurement point far from the VLF-LF transmitters, the electromagnetic field over a homogeneous half-space has horizontal and vertical electric components in the direction of transmission, and horizontal magnetic components perpendicular to the direction of transmission. The ratios of the components (E_x, E_z, H_y) are related to the conductivity (σ_1) of the half-space

$$W = \frac{E_x}{E_z} = \frac{1+i}{\sqrt{2}}\sqrt{\frac{\omega\varepsilon_0}{\sigma_1}} \tag{2}$$

$$Z = \frac{E_x}{H_y} = \frac{1+i}{\sqrt{2}}\sqrt{\frac{\omega\mu_0}{\sigma_1}} \tag{3}$$

where W is wave slope; Z – input impedance ; ε_0 – dielectric constant of a vacuum; μ_0 is magnetic permeability of the vacuum. The $1 + i$ factor in the equations indicates that there is a 45° phase difference between the components. Since all three field components in the equations can be easily measured, it is possible to determine the conductivity or resistivity of the half-space

$$\rho_a = \frac{1}{\mu\omega}\left|\frac{E_x}{H_y}\right|^2 \tag{4}$$

$$\rho_a = \frac{1}{\varepsilon\omega}\left|\frac{E_x}{E_z}\right|^2 \tag{5}$$

In the case of 2D and 3D effects, a vertical magnetic component is induced. The VLF-EM method uses only the magnetic components. Since the vertical magnetic component *(H_z)* is in phase shift *(ϕ)* with the tangential magnetic component *(H_x)*, the magnetic field is described by a polarization ellipse *(a, b, θ)*. Paterson and Ronka (1970) reported on the first experiences of the application of VLF-EM. Saydam (1981) wrote about the interpretation of inclination angle and ellipticity measurements

$$\text{tilt angle:} \tan(2\theta) = \frac{2^{H_z}/_{H_x}\cos\phi}{1-\left({}^{H_z}/_{H_x}\right)^2} \tag{6}$$

$$\text{ellipticity:} \varepsilon = \frac{b}{a} = \frac{H_z H_x \sin\phi}{\left|H_z e^{i\phi}\sin\theta + H_x\cos\theta\right|^2} \tag{7}$$

It is worth writing the relationships for the normalized real and quadrature H_z component as well. For small secondary magnetic components, the tilt angle is equal to the real component of the secondary magnetic field, while the ellipticity is equal to the imaginary component

$$H_z(I) = \frac{H_z}{H_x}\cos\phi \ ; H_z(Q) = \frac{H_z}{H_x}\sin\phi \tag{8}$$

$$\tan 2\theta = 2H_z(I)\frac{1}{1-\left({}^{H_z}/_{H_x}\right)^2} \cong 2H_z(I) \tag{9}$$

$$\varepsilon = H_z(Q)\frac{1}{(H_z(I)\sin\theta+\cos\theta)^2+(H_z(Q)\sin\theta)^2} \cong H_z(Q) \tag{10}$$

In the two-dimensional case, the relationship between the target orientation and the direction of the field components is of great importance. When the electric field is aligned with the structural strike of the target, the configuration is referred to as E-polarization. Conversely, when the magnetic field is parallel to the structural strike, it is referred to as H-polarization. If we measure with only one transmitter, with a VLF wave coming from a given direction, then we speak of scalar measurement. If we measure with VLF waves coming from several directions, then in addition to the slightly different frequency, the measured value will also differ due to the structure being different from 1D. In this case, we speak of tensor measurement. Farkas (1978) proposed a VLF invariant resistance method to eliminate the 2D effect. Pedersen (1998) mentioned the tipper vector for tensor VLF measurements (using at least two or more transmitters). At a given frequency, the vertical component of the magnetic field is linearly related to the horizontal components, where A and B are the components of the tipper vector

$$H_z = AH_x + BH_y \tag{11}$$

2. Interpretation Methods

In the early days of the VLF method, when only magnetic components were measured, the interpretation of the measurements was based on anomalies in the graphical representation of the measurements along the section. The first quantitative data processing was proposed by Fraser (1969). The original goal of the procedure was to filter the data. Four consecutive data are used for filtering. The average of the first two is subtracted from the average of the last two, but the divisions by two are omitted

$$f_{2,3} = (M_3 + M_4) - (M_1 + M_2) \tag{12}$$

where $M_i$denotes four measurement data *(i=1,2,3,4),*$f_{2,3}$, is the result of the Fraser filtering applied between points 2 and 3. This gives us the directional derivative of the average data. Filtering reduces noise, suppresses topographic effects, and simplifies the interpretation of anomalies by transforming an asymmetric (sign-changing) dip angle anomaly into an anomaly with a maximum peak.

Kaikkonen (1979) performed 2D numerical modeling for the anisotropic case using the finite element method. He investigated the effect of a tilted, finite plate covered with a layer. He found that in the case of a bad conductor, the inclination angle and the ellipticity polarity are the same, but in the case of a good conductor, the polarity and shape of the ellipticity also change. The inclination of the plate spoils the symmetry of the anomaly. Saydam (1981) reported relationships between the amplitude, width and simple acting parameters (depth, width, etc.) of inclination angle and ellipticity anomalies. Bezvoda and Segeth (1982) investigated the effect and detectability of two adjacent dykes, also using the finite element method. Teemull and Crossley (1982) described an inversion procedure for simple 2D structures where continuous, weak lateral changes can be described using harmonic functions. Karaous and Hjelt (1983) developed a linear filtering procedure for VLF inclination measurements. The result of the filtering is equivalent current densities for different depths. The filtering procedure can be considered an extension of the Fraser filter

$$H_{KH} = -0.201H_{-2} + 0.323H_{-1} - 1.446H_0 + 1.446H_1 - 0.323H_2 + 0.205H_3 \quad (13)$$

Olsson (1983) investigated a model of a plate in a horizontally layered half-space. McNeil (1991) has a RELACON filter like the Fraser filter but designed to convert VLF magnetic data into relative conductivity data. Ogilvy et al. (1991) investigated the detectability of 2D low-conductivity. They showed that in the case of H-polarization, a higher apparent resistivity and smaller phase (lower than 45°) can be measured above the target. In the case of E-polarization, the cavity cannot be detected. This highlights the importance of using at least two transmitters, oriented nearly perpendicular to each other, if it is possible. Takács et al. (2005) compared the current density pseudosection with 2D VLF-EM anomalies. Pethő et al. (2006) investigated the response of near-surface targets for plane waves (VLF) and electric dipoles in TE and TM modes. Pethő (2012) and Vincze et al. (2024) present the application possibilities of the VLF method in Hungary.

By measuring the electrical component, it became possible to determine the apparent resistivity and, at the same time, to apply the 1D inversion previously developed in magnetotellurics. From the apparent resistivity and phase difference data measured at a VLF frequency, the parameters of a two-layer model can be calculated by assuming one of the three parameters to be known. The calculations are facilitated by the fact that the forward modeling of the 1D layered half-space can be solved with a simple recursive formula. In the case of a horizontally layered n-layer half-space, the parameters ρ_n (layer resistivities) and h_{n-1} (layer thickness) can be used to calculate the data ρ_a (apparent resistivity) and φ (phase) using a recursive formula (see Tutorial). The calculation should start with the impedance of the lowest layer:

$$Z_n = \sqrt{i\omega\mu_0\rho_n} \quad (14)$$

then the reflection coefficient occurring at the boundary of the next layer is calculated as

$$R_{n-1} = \frac{\sqrt{i\omega\mu_0\rho_{n-1}} - \sqrt{i\omega\mu_0\rho_n}}{\sqrt{i\omega\mu_0\rho_{n-1}} + \sqrt{i\omega\mu_0\rho_n}} \quad (15)$$

after that the impedance of the next layer can be calculated

$$Z_{n-1} = \sqrt{i\omega\mu_0\rho_{n-1}} \frac{1 - R_{n-1}\exp(-2\sqrt{\frac{i\omega\mu_0}{\rho_{n-1}}}h_{n-1})}{1 + R_{n-1}\exp(-2\sqrt{\frac{i\omega\mu_0}{\rho_{n-1}}}h_{n-1})} \quad (16)$$

The reflection coefficient and impedance of the next layer boundary can be calculated, until we reach the topmost, first layer, from whose impedance the apparent resistivity and phase values can be calculated

$$\rho_a = \frac{1}{\mu_0 \omega} |Z_1|^2 \tag{17}$$

$$\varphi = \tan^{-1} \frac{\mathrm{Im}(Z_1)}{\mathrm{Re}(Z_1)} \tag{18}$$

Numerous nomograms, recursion formulas and computer programs have been developed to estimate the model parameters. It should be noted that in the two-layer case, the phase deviation from 45°carries valuable information about the resistivity relationship of the lower and upper layers. If $\varphi < 45°$, then $\rho_2 > \rho_1$, but for $\varphi > 45°$, then $\rho_2 < \rho_1$.

The need to extend the narrow frequency range of the VLF band arose early on. Takács (1971) used a frequency range of 155 kHz and 629 kHz to solve various geological tasks (limestone, andesite, sandstone exploration). Pethő and Újszászi (1975) investigated the applicability of the radio-kip method for cave exploration. Stiefelhagen and Müller (1979) performed measurements in the 15–300 kHz range and confirmed their hydrogeological usefulness. Beamish (2000) compared the VLF and RMT methods in terms of layer resolution, see Figure 1.

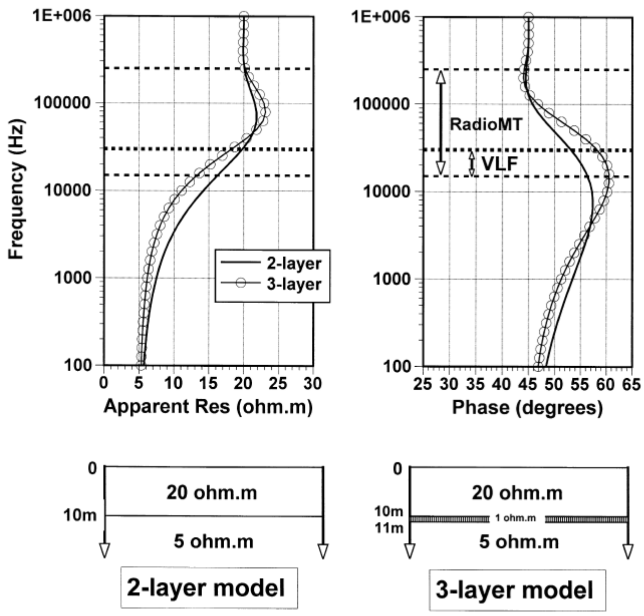

Figure 1

Evaluability analysis of two- and three-layer models in the case of VLF and RMT

The study demonstrates the importance of the extended frequency range of RMT in the investigation of 1D structures. In the case of two-dimensional effects, we find that in some cases even mono-frequency VLF measurements are able to approximate the structure.

Pirttijarvi (2006) developed a two-layer inversion with a known parameter-free lateral constraint for processing VLF-R measurements. This minimizes the model's roughness between neighboring points, resulting in a model with smooth variation (Occam inversion), see Figure 2.

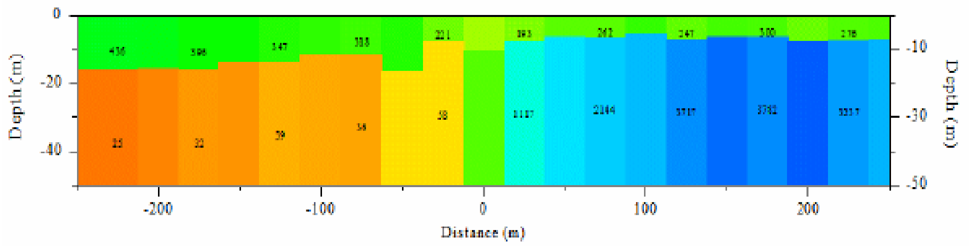

Figure 2

Laterally constrained two-layer inversion of VLF-R measurement data

Schmalz et al. (2007) published a similar inversion for radio-magneto-telluric data, where the number of layers could be increased. In addition, Rodi and Mackie (2001) also implemented a 2D inversion using the nonlinear conjugate gradient (NLCG) method.

Following in the footsteps of the previous ones, EMTOMO (2022) developed the VLF2DMF application, a program for 2D inversion of multifrequency VLF-EM data. 2D and 3D forward modeling is solved using finite element, finite difference, integral equation and scattering matrix formalism methods. For 2D and 3D inversion, linearized second-order Marquardt least squares (LSQ), nonlinear conjugate gradient (NLCG) or global optimization based very fast simulated annealing (VFSA) methods are commonly used.

3. Developments of VLF instruments

It is valuable to review the development of VLF instruments because the structure of the initial RMT instruments was completely identical to that of VLF instruments, only with an extended frequency range. The simplest VLF receivers resemble a straight-line radio receiver, see Figure 3. The selection of the desired frequency is provided by a parallel LC circuit, which is the antenna of the instrument itself. VLF receivers with such a system are the Scintrex SE-81 and the Phoenix VLF-2 instrument.

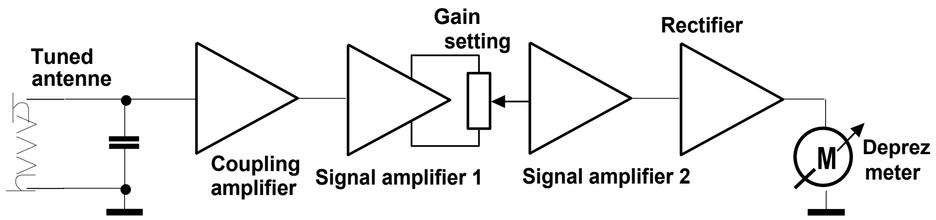

Figure 3

Block diagram of a straight-forward VLF receiver

The first widely used VLF receiver, the Geonics EM16/16R instrument, uses the so-called heterodyne principle to increase selectivity, see Figure 4.

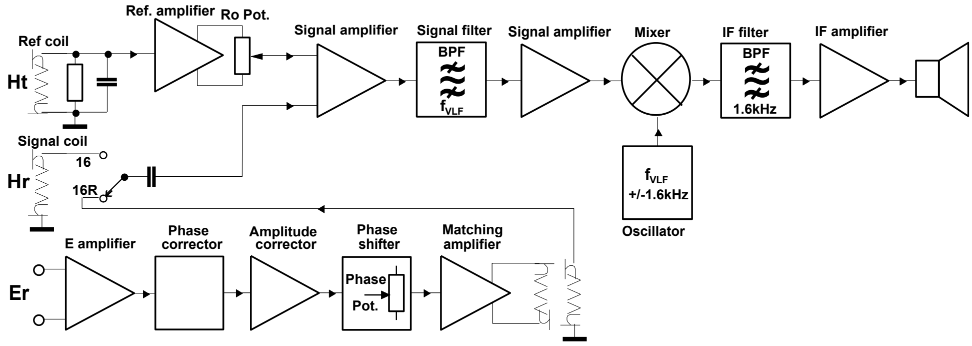

Figure 4
Schematic of Geonics EM16/16R

With the advent of digital CMOS circuits, various hybrid receivers were built, in which the selection of the reception frequency and the display of the measurement results are now done digitally, but the circuits ensuring selectivity still remain analog. Such VLF instruments include the Totem II instrument of Herz Instrument, the CNYN instruments of the University of Neuchatel, the Syscal VLF instrument of BRGM and the VDV-1 instrument of Geofyzika Brno. To ensure selectivity when using broadband antennas, hybrid filters and digital signal processing methods have begun to be used. Examples include the Iris Instrument T-VLF instrument, the ABEM Wadi instrument, the Scintrex Envi-VLF instrument, and the GEM System walking VLF sensor.

4. Developments of RMT instruments

In the early days, ordinary long-wave radio receivers were also used to receive signals from radio stations above the VLF band, e.g. by Takács (1971). The University of Neuchatel extended the frequency range of earlier VLF instruments to 240 kHz.

The first tensor RMT instrument was developed at Uppsala University in Sweden (Bastani, 2001) under the name EnviroMT. The five-channel recorder can measure all three magnetic and both surface electric field components. It is the first RMT instrument that broke with the frequency-selective measurement technique, which can process only one transmitter signal at a time, and applied the Fourier transformation processing of time-domain recordings, which was already used in magnetotellurics. The frequency range 1–250 kHz was divided into two parts. In the frequency range 1–25 kHz, the broadband signal is recorded with 200 kHz sampling, while in the range 10–250 kHz, the broadband signal is recorded with 20 MHz sampling. The lower 1–25 kHz range is used more with the CSMT transmitter, while the upper 10–250 kHz range is used with VLF-LF radio transmitters. The electric field is measured with grounded dipoles 5–10 m apart, while the magnetic field components are measured with 30 cm long, 7.5 cm diameter coils.

The four-channel RMT-F1 instrument was developed at Saint Petersburg State University in collaboration with the University of Cologne and MicroKOR Tezkan and Saraev (2008). Originally, the instrument was designed to have four channels, which allowed the recording of two electrical and two magnetic channels with a 16-bit A/D converter in the frequency range of 10–1000 kHz. It recorded 16kSample (16 × 1024 sample/sec) packets with a sampling rate of 2.5 MHz. The improved version of the instrument, the RMT-F, also received a fifth channel for recording the vertical magnetic component, the frequency range was extended to 1 kHz and the recording was done in 64kSample (64 × 1024 sample/sec) packets.

The latest extended application development of the instrument is called ARMT-5. The instrument is suitable for measuring in audio and radio frequency ranges in the range of 0.1 Hz–1 MHz. The recorder has two five 16-bit A/D converters for the 10–1000 kHz range with 400 and 4000 kHz sampling and 24-bit A/D converters for the 0.1–10000 Hz frequency range with 32 and 4 kHz sampling. A great advantage of the recorder is the continuous sampling up to 4 MHz and the online display of data in both the time and frequency domains.

Modern magnetotelluric instruments with antennas with an appropriate frequency range are also suitable for RMT measurements. The Metronix ADU-08E logger, for example, has a sampling rate of 256 Hz to 262 kHz, which in principle allows recording up to 131 kHz. The SHFT-02 sensor has a bandwidth of 1–300 kHz. The Geometrix Stratagem EH-5 instrument has a frequency range of 1 Hz to 96 kHz.

5. Design consideration for a modern RMT instrument

To exploit the full range of possibilities offered by the method, it is worth preparing to measure all possible field components. Three mutually perpendicular induction broadband antennas and three measuring channels are required for a complete measurement of the magnetic field strength. Measurement of the electric field strength can be made on the surface of the ground or in the air. No current can flow perpendicular to the interface between the conductive half-space and the air, thus two pairs of mutually perpendicular electrodes on the surface are sufficient for the complete determination of the electric field. This can be a ground electrode to be inserted into the ground, or a capacitive electrode that allows continuous measurements. In the conductive half-space, the vertical electric component is important for measurements in boreholes. In the air, however, the vertical electric component also appears when rising from the surface and the horizontal components also behave depending on the height. In the frequency range of the method, an electric dipole or rod antenna that is greatly shortened compared to the wavelengths can only be used to good effect. These have low sensitivity (effective height) and are very sensitive to proximity to humans or the ground. They are only suitable for aerial measurements.

The unambiguous determination of the position of the sensors can be solved by using three types of spatial sensors. The global position of the measurement point can be determined by GPS or now more commonly GNSS equipment, the deviation of the sensors from the horizontal can be determined by two perpendicular tilt-probe meters, and the angular position around the vertical axis can be determined by a magnetic compass. Recently, the precise determination of the global location coordinate was considered a very expensive and resource-intensive task. The location accuracy of simple, cheap and small solutions (car navigation), which was limited to approx. 5-10 m even under favorable reception conditions, in many cases did not satisfy the needs of high-resolution ground measurements. For sub-meter and sub-decimeter location accuracy, the use of larger and more expensive antennas and also additional cost-intensive RTK (real-time kinematic) was required. Nowadays, however, small GNSS modules have appeared and are rapidly spreading, capable of sub-meter accuracy in autonomous mode or sub-decimeter accuracy with RTK.

When reviewing the development of VLF and RMT instruments, we also saw that the most modern instruments have broadband magnetic antennas, high input impedance and low capacitance electrical input amplifiers and minimal additional analog circuits. The signals to be measured are digitized after a mandatory antialiasing low-pass filter, and then further signal processing is done digitally. Similar to the previously described analog principles ensuring frequency selectivity, mixing of the heterodyne system, bandpass filtering, and phase selective demodulation, all of these functions can also be performed in the digital space. If it is necessary to use an analog output device, for example a loudspeaker for acoustic indication, this can also be solved at the end of the signal processing, after digital-to-analog conversion, using minimal analog hardware elements (recombination filter, power amplifier). We have also shown earlier that the development of personal computers has long reached the level that real-time SDR (Software Defined Radio) in the RMT frequency range is not a problem. These capabilities have long been surpassed by laptops, notebooks, tablets and mobile phones. Many new geophysical instruments can be seen today equipped with field tablets. Moreover, these devices are equipped with almost unlimited data storage capacity and even the above-mentioned sensors (GNSS, compass, spirit level). In order to reduce consumption, weight and size, it makes sense to implement the aforementioned functions with target hardware. The new generation of 16/32-bit microcontrollers equipped with DSP (Digital Signal Processing) functions provides excellent opportunities for solving the aforementioned tasks. The great advantage of DSP is that, for example, the large-bit multiplication operation required for fast Fourier transformation is not performed by machine routines with hundreds of instructions, but is performed in cycles of a few hours. To demonstrate that a real-time radio receiver operating in the RMT band is feasible, an Italian radio amateur Alberto di Bene (online) built a simple radio receiver operating in the 8–900 kHz range using the Discovery development board built with the STM32F429 microcontroller and some additional analog circuitry, see Figure 5.

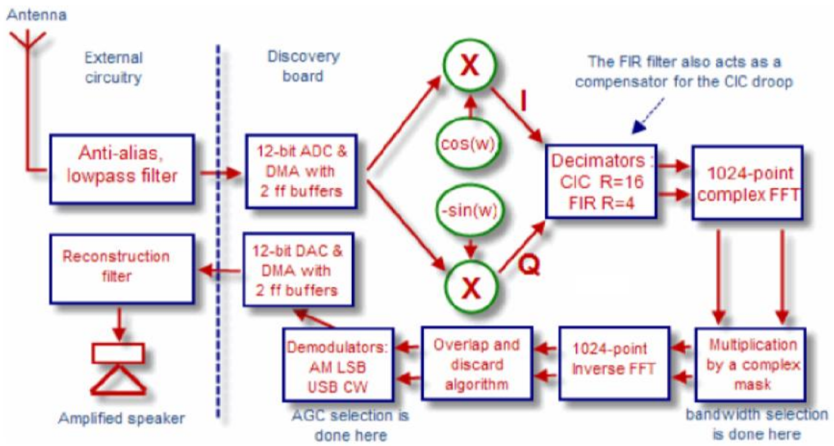

Figure 5
Direct receiver for a frequency of 8-900 kHz

6. Radio transmitters in the VLF and RMT band receivable in Hungary

The frequency range from 10 kHz to 1 MHz includes the VLF (very low frequency) band, which is used for submarine communications and includes time signal transmitters, as well as the LF (low frequency) and partly the MF (medium frequency) bands, which include broadcast transmitters and amateur bands.
Until the 70s and 80s, several transmitters operated continuously in the VLF band, in the 15.1–24.0 kHz range, which then ceased to operate one after another. Instead, a smaller number of new transmitters were launched in the 18.1–26.7 kHz range. There is also a stably operating transmitter station in the 40–100 kHz range. The best known of them is the DCF77 time signal transmitter (77.5 kHz).

There are also stable transmitters in the 100–153 kHz range, the source of which has yet to be investigated. The previously bustling life in the LF and MF bands has now died down, but a few usable transmitters remain.

It is clear from Table 2 that the distribution of frequencies that can be received in good quality in Hungary is not uniform. The frequencies that are close to each other, arriving from different directions, provide an opportunity to calculate the invariant apparent resistivity.

Table 2
Radio transmitters in the RMT band receivable in Hungary (based on own measurements)

Frequency	Power	Country	Region	Call Sign
18.1 kHz		Russia	Krasnodar	RDL
18.3 kHz		France	Rosnay	HWU
19.6 kHz	30 kW	UK	Anthorn	CQD
20.27 kHz		Italy	Tavolara	ICV
21.75 kHz		France	Rosnay	HWU

Frequency	Power	Country	Region	Call Sign
22.1 kHz		UK	Anthorn	CQD
23.4 kHz	800 kW	Germany	Rhauderfehn	DHO38
24.0 kHz	1000 kW	USA	Cutler, Maine	NAA
26.7 kHz		Turkey	Bafa	TBB
40.4 kHz		Sweden	Grimeton	SRC
44.2 kHz		Sweden		SAS3
45.9 kHz	250 kW	Italy	Niscemi	NSY
51.95 kHz		UK		
60.0 kHz	17 kW	UK	Anthorn	MSF
62.6 kHz		France	La Regime	FUG
65.8 kHz		France	Kerlouan	FUE
66.6 kHz	10 kW	Russia	Moscow	RBU
77.5 kHz	50 kW	Germany	Mainflingen	DCF77
81 kHz		UK		GYN2
81.8 kHz				
89.6 kHz				
112.0 kHz				
113.7 kHz				
128.9 kHz				
133.7 kHz				
135.4 kHz				
153 kHz	200 kW	Romania	Brasov	SSR Antena Sat.
162 kHz	800 kW	France	Allouis	TDF, ALS162
171 kHz	1600 kW	Morocco	Nador	Radio Méditeranée Internat.
189 kHz	300 kW	Iceland	Hellissandur	RÚV 1/2
198 kHz	500 kW	UK	Droitwich	BBC Radio 4 AM
225 kHz	1000 kW	Poland	Solec Kujawski	Polskie Radio
252 kHz	1500/750 kW	Algeria	Tipaza	Radio Algérie

7. Design consideration for RMT instrument sensor

To detect the magnetic components of the electromagnetic field, it is advisable to use a broadband antenna whose amplitude and phase shift are uniform or at least do not vary sharply in the required frequency range. Such a magnetic antenna can be produced using the principle of flux feedback. Figure 6a shows the amplitude and phase progression of an implementation. Figure 6b shows the circuit diagram of the implementation.

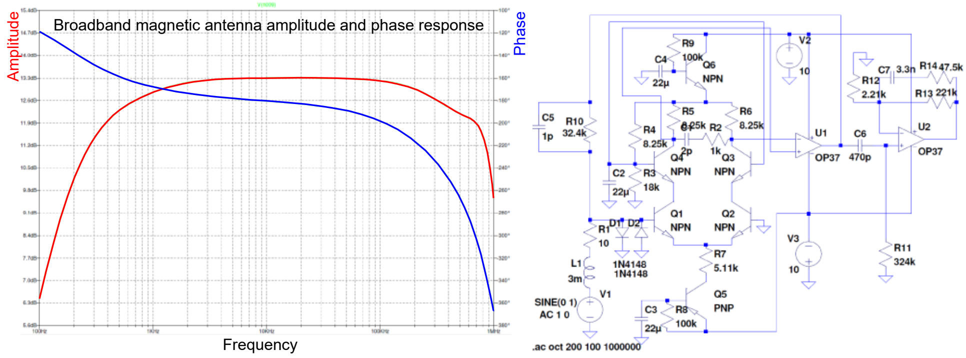

a *b*

Figure 6

Frequency and phase response (a) and circuit diagram (b) of H-sensor

A capacitive antenna with a suitable linear transfer can be realized with a preamplifier with a high input resistance and a small capacitance, which also has a low quiescent input current. In the figure below, we examine the transfer of the capacitive antenna with coupling capacitances of 1pF, 5pF, 10pF, 50pF, 100pF and 500pF. It is clear that the linear transition can be ensured with coupling above 5pF. Figure 7a shows the amplitude and phase progression of an implementation. Figure 7b shows the circuit diagram of the implementation.

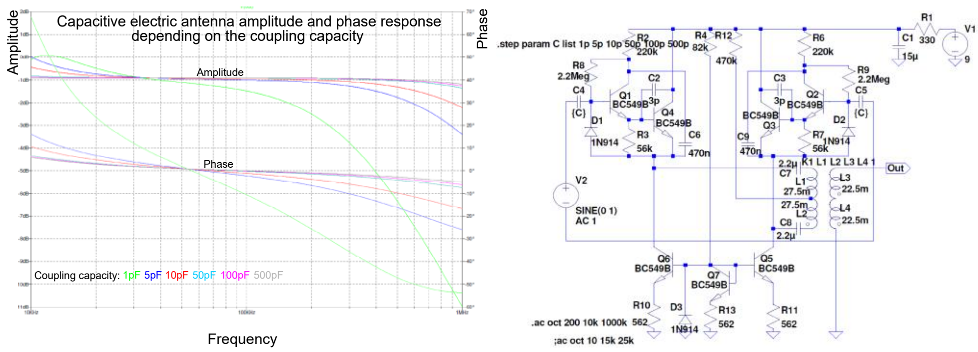

a *b*

Figure 7

Frequency and phase response (a) and circuit diagram (b) of the E-sensor

8. CONCLUSIONS

In a modern RMT instrument, it is advisable to measure as many parameters as possible, which are generally three magnetic and three electrical components. On land and water, only two electrical components can be conveniently measured. In the air, it is theoretically possible to measure all three electrical components, but in practice, it is more feasible to measure the three magnetic components. For measurements on the ground, the condition for moving measurements is the use of a capacitive electric dipole. With high input resistance and large capacitance preamplifiers, uniform transmission can be achieved if the coupling of the capacitive sensors to the ground is not worse than 5 pF. It is advisable to design the magnetic antennas to be broadband and provide them with a preamplifier based on the principle of flux feedback. Determining the position of the sensors is of fundamental importance. With modern GNSS modules, positioning accuracy of around 1 m can be achieved even in autonomous cases. The inclination of the sensors should be measured with two-way inclinometer sensors. The azimuth of the sensors can be determined with a semiconductor magnetic compass. It also provides a suitable solution for tensor measurements, recording short, broadband signal packets during measurements, and then digitally measuring the selected frequencies using SDR and DSP. An important goal is to create a profile or map image from the measurement results in real time. The use of 1D-LCI seems suitable for this purpose.

Acknowledgments

I am grateful to Professor Ernő Takács for introducing me to the exciting world of electromagnetic methods. I am grateful to the former ELGI for the opportunity to become familiar with the practical application of numerous electromagnetic instruments and methods. Finally, I would like to thank my supervisors, Professors Mihály Dobróka and Gábor Pethő, for their support in this topic.

References

Bastani, M. (2001). EnvitoMT: *A new controlled source/radio magnetotelluric system*. PhD dissertation, University Uppsala.

Beamish, D. (2000). Quantitative 2D VLF data interpretation. *Journal of Applied Geophysics*, 45, pp. 33–47.

Bezdova, V., Segeth, K. (1982). Onthe resolving power of the VLF method. *Pure and Applied Geophysics*, 120 (2), pp. 348–364.

Cagniard, L. (1953). Basic theory of the magneto-telluric method of geophysical prospecting. *Geophysics*, 18 (3), pp.603–635.

di Bene, A. *ARM Radio: a project for the ARM MCU Design Contest*. Available online: https//www.i2phd.org/code/ARM-Radio.pdf, (accessed on 1 December 2024).

Dosso, H. W. (1962). The magnetic field at the surface of a stratified flat conductor in field of planewaves with application to geophysics. *Canadian Journal of Physics*, 40 (11), pp.1583–1592.

Dosso, H. W. (1965a). The electric and magnetic fields in a stratified flat conductor for incident planewaves. *Canadian Journal of Physics*, 43 (5), pp.898–909.

Dosso, H. W. (1965b). A multilayer conducting earth in the field of planewaves. *Canadian Journal of Physics*, 44 (1), pp.81–89.

EMTOMO, (2022). VLF2DMF A *program for 2-D inversion of multifrequency VLF-EM data*. Operational Manual.

Farkas, I. (1978). *VLF invariáns ellenállás módszer*. A Magyar Állami Eötvös Loránd Geofizikai Intéztet 1978. évi jelentése, pp. 79–80.

Fraser, D. C. (1969). Contouring of VLF-EM data. *Geophysics*, 34 (6), pp. 958–967.

Kaikkonen, P. (1979). Numerical VLF modeling. *Geophysical Prospecting*, 27 (4), pp. 815–834.

Karous, M., Hjelt, S. E. (1983). Linear filtering of VLF dip-angle measurements. *Geophysical Prospecting*, 31, pp. 782–794.

McNeil, J. D., Labson, V. F. (1991). Geological mapping using VLF radio fields. *Electromagnetic Methods in Applied Geophysics*, Chp.7., pp. 521–640.

Ogilvy, R. D., Cuadra, A., Jackson, P. D., Monte, J. L. (1991). Detection of an air-filled drainage gallery by the VLF resistivity method. *Geophysical Prospecting*, 39, pp. 845–859.

Olsson, O. (1983). Computation of VLF response over half-plane and wedge models. *Geophysical Prospectings*, 31, pp. 171–191.

Paterson, N. R. and Ronka, V. (1970). Five years of surveying with the very low frequency electromagnetic method. *Geoexploration*, 9, pp.7–26.

Pedersen, L. B. (1998). Tensor VLF measurements: Our first experiences. *Exploration Geophysics*, 29, pp. 52–57.

Pethő, G. (2012). Geological application of the VLF method. *Geosciences and Engineering*, 1 (2), pp. 129–139.

Pethő, G., Ficsór, L., Szabó, I. (2006). Comparison of 2-D VLF and 2.5D HED's far field regime EM field. *microCAD Conference Paper*, 2006, Miskolc, pp. 35–40.

Pethő, G., Újszászi, J. (1975). Barlang kutatás radiokip módszerrel. *Magyar Geofizika*, 16 (5), pp. 181–186.

Pirttijarvi, M. (2006). *2LAYINV. Laterally constrained two-layer inversion of VLF-R measurements*. Operating Manual.

Rodi, W., Mackie, RL. (2001). Nonlinear conjugate gradient algorithm for 2-D magnetotelluric inversion. *Geophysics*, 66 (1), pp. 174–187.

Saydam, A. S. (1981). Verylow-frequency electromagnetic interpretation using tilt angle and ellipticity measurement. *Geophysics*, 46 (11), pp. 1594–1605.

Schmalz, T. et al. (2007). *1D-laterally constraint inversion (1D-LCI) of radio-magnetotelluric data, 22*. Kolloquium Electromagnetische Tiefenforshung.

Stiefelhagen, W, Müller, I. (1979). Radiofrequency electromagnetics (RFEM): VLF-EM extended to hydrogeological problems. *59th Meeting of EAGE*, Geneva, 1979.

Takács, E. (1971). Tapasztalatok a radiokip módszer alkalmazásában. *Magyar Geofizika*, 12 (4), pp.148–160.

Takács, E., Pethő, G., Szabó, I. (2005). Comparativ investigation about the applicability of current density pseudo sections in the interpretation of 2D VLF vertical magnetic anomalies. *Acta Geod. Geoph. Hung*., 40 (4), pp. 127–146.

Teemull, F. A., Crossley, D. J. (1982). Inversion of VLF data for simple lateral inhomogeneities. In: Geophysical Application of surface wave impedance measurements. *Geological Survey of Canada*, pp. 81–15, 79–86. https://doi.org/10.5006/C2013-02762

Tezkan, B., Saraev, A. (2008). A new broadband radiomagnetotelluric instrument – application to near surface investigation. *Near Surface Geophysics*, 6 (4), pp. 245–252.

Tutorial – 1D Forward Modelling (Magnetotelluric). Available online: https://www.digitalearthlab.com/tutorial/tutorial-1d-mt-forward/ (accessed on 1 December 2024).

Vincze, L., Németh. N., Pethő, G. (2024). Eredmények és tapasztalatok a VLF módszer területén. *Magyar Geofizika*, 65 (1), pp. 27–45.

Wait, J. R. (1953). Propagation of radio waves over a stratified ground. *Geophysics*, 18 (2), pp. 416–422.

Geosciences and Engineering, Vol. 13, No. 2 (2025), pp. 65–74.
https://doi.org/10.33030/geosciences.2025.02.005

INFLUENCE OF INJECTION RATE ON WORMHOLE MORPHOLOGY IN MATRIX ACIDIZING USING CARBONIC ACID

ABDULAMEER ALMALICHY[1]*, ZOLTÁN TURZÓ[2]
[1, *]*Institute of Mining and Energy, University of Miskolc;*
abdulameer.almalichy@student.uni-miskolc.hu
[2]*Institute of Mining and Energy, University of Miskolc;*
oljtz@uni-miskolc.hu
[1]*https://orcid.org/0009-0008-1772-9224*
[2]*https://orcid.org/0000-0002-7147-1163*

Abstract: This study examines the effect of varying injection rates on wormhole formation during matrix acidizing using a carbonic acid solution (30% CO_2 + 70% deionized water). Injection rates of 0.2, 0.5, and 1 cm^3/min were tested, and the resulting wormhole structures were visualized using CT scanning. Results show that lower injection rates produce single, more efficient wormholes with minimal branching, while higher rates generate more branched, less efficient structures. Optimizing the injection rate is key to achieving effective wormhole formation, which can enhance flow in carbonate reservoirs.

Keywords: *carbonic acid, wormhole, computed tomography scan, matrix acidizing*

1. INTRODUCTION

Recent advancements in CO_2 utilization have expanded its potential beyond traditional applications like enhanced oil recovery (EOR) and carbon capture and storage (CCS). One emerging application is using carbonic acid, derived from CO_2 and water, as a stimulation fluid for carbonate reservoirs. This method reduces greenhouse gas emissions and addresses tubular corrosion commonly associated with hydrochloric acid (HCl) usage. Carbonic acid offers a more sustainable and eco-friendly alternative for well-stimulation without compromising efficiency (Almalichy et al., 2024; Al-Yaseri et al., 2023; Ma et al., 2021).

Matrix acidizing, a widely used technique, enhances well productivity by injecting acid solutions below the formation's fracture pressure to remove formation damage and create flow channels known as "wormholes" (Alameedy et al., 2023; Almalichy et al., 2022). While HCl has been the primary acid in use since the 1890s due to its effectiveness in dissolving carbonate formations, it presents challenges such as high corrosivity, rapid reaction rates in high-temperature and high-pressure environments, and the need for costly corrosion inhibitors (Chacon and Pournik, 2022). As a result, alternative acids with slower reaction rates and reduced corrosivity are being sought (Rodrigues et al., 2021) to stimulate the heterogeneous carbonate revervoir (Mohammed and Velledits, 2024).

Organic acids, such as methanesulfonic acid (MSA) and acetic acid, are increasingly considered practical substitutes for conventional acid systems in matrix acidizing. MSA is notable for its reduced reactivity relative to hydrochloric acid (HCl), an attribute assigned to its weakened hydrogen ion (H^+) activity coefficient and elevated pKa value. These properties markedly reduce the acid's reaction rate with carbonate formations, facilitating deeper reservoir penetration. The reduced reactivity is beneficial for forming efficient wormholes, essential for increasing permeability and optimizing hydrocarbon flow pathways (Ortega, 2015; Shank and McCartney, 2013).

Like other weak acids such as formic acid, Acetic acid shows slower reaction kinetics than stronger acids such as HCl. This reduced reactivity facilitates a regulated acid-rock interaction, enabling the acid to penetrate deeper into the formation. The outcome is a more consistent stimulation and the possibility of enhanced acid infiltration into the reservoir matrix, which is especially advantageous for reservoirs characterized by significant heterogeneity or complex conditions. These organic acids provide customized solutions for effective stimulation while reducing unwanted near-wellbore reactions (Al-Douri et al., 2013; Chang et al., 2008).

The different retarded acid systems, including gelled acids, in-situ gelled acids, and emulsified acids, were developed and published as novel means of controlling acid reactivity for the stimulation of carbonate reservoirs. These are specially designed to retard the acid-rock reaction rate to improve the depth and uniformity of acid penetration and minimize the problem of premature acid spending near the wellbore. Gelled acids are among the most effective techniques. Gelled systems improve acid placement by reducing fluid loss and providing better coverage in the formation due to increased acid viscosity(AlOtaibi et al., 2020). This enhanced viscosity plays a vital role in overcoming problems in heterogeneous-permeability formations where conventional acid treatments often fail. Conventional acids tend to bypass into high-permeability zones and avoid areas of low permeability. Gelled acids can compensate for this deficiency by offering a more uniform distribution of the acid, with delivery into low-permeability zones that otherwise would not have been treated. Moreover, the high-viscosity nature of gelled acids prevents leak-off into the surrounding formation, which maintains the acid strength and allows deeper and more effective wormholes. Therefore, the gelled acid systems are perfect for stimulating carbonate reservoirs with dominantly complex rock properties such as variable porosity and permeability (Ratnakar et al., 2012).

Apart from their role in regulating reactivity and improving distribution, gelled acids contribute to operational efficiency and economy. Indeed, they require a smaller volume of acid to achieve similar or improved performances compared with the conventional acid systems. This, in turn, reduces the overall consumption of treatment fluids. They can minimize near-wellbore damage and provide even stimulation across the formation, translating this into higher well productivity and extended life of the treatment (Lynn and Nasr-El-Din, 2001; Zakaria and Nasr-El-Din, 2016).

Emulsified acids, comprising finely dispersed hydrochloric acid (HCl) droplets within a continuous oil phase, effectively regulate acid-rock interactions during matrix acidizing operations. The distinctive composition of these emulsions markedly inhibits the reaction between the acid and the carbonate rock, facilitating deeper penetration of the acid into the reservoir before the reaction. This regulated reactivity is essential for enhancing acid distribution and attaining more consistent stimulation. Surfactants are necessary for preserving the stability of emulsified acids by facilitating the formation and stabilization of the emulsion structure. Surfactants effectively control acid release at the rock surface by capturing the acid droplets within the oil phase. This mechanism decreases acid consumption near the wellbore. It mitigates premature acid expenditure, thereby facilitating a larger volume of acid to penetrate deeper into the formation, where it can generate effective wormholes. (Al-Anazi et al., 1998; Maheshwari et al., 2014).

Besides effectiveness related to the improvement of wormhole formation, several advantages of emulsified acid are associated with its own nature. The oil phase in the emulsion may act like a seal, significantly reducing leakoff of the acid into the formation matrix and preserving the acid for intended reaction zones. This characteristic is especially welcome in reservoirs with sharp permeability contrasts, where conventional acid systems often fail to yield balanced stimulation. Emulsified acids enable more resource efficiency and better treatment outcomes by reducing the active agent loss to a minimum and optimally applying the acid. Moreover, the tunable properties of the emulsified acid systems enable modifications in properties for matching conditions in specific reservoirs. The type of surfactant, formulation of the oil phase, and acid concentration can be changed in order to optimally develop the emulsion for various operational conditions. The versatility of emulsified acids makes them amenable to addressing most of the problems associated with heterogeneous carbonate formations (Buijse and van Domelen, 1998; Crowe and Miller, 1974).

Emulsified acids economically provide a means of cost savings through the reduction of the total amount of acid required for effective stimulation. Their capability to increase the penetration depth, reduce near-wellbore acid lost, and improve treatment efficiency gives them long-term production benefits, thus making them an important component in acidizing today (Adewunmi et al., 2022).

Chelating agents such as ethylenediaminetetraacetic acid (EDTA) and nitrilotriacetic acid (NTA) have been extensively studied to enhance deep acid penetration and promote uniform distribution within carbonate formations. These chemicals form very stable complexes with calcium ions; therefore, they offer very good control of the acid reaction rate and a drastic reduction of excessive acid consumption near the well-bore. This controlled reaction mechanism provides a particular advantage in applications to high-temperature carbonate reservoirs, where the use of conventional acidizing methods is commonly limited. (Frenier et al., 2000; Yan et al., 2019).

Foamed acid systems, prepared conventionally by adding nitrogen gas to hydrochloric acid, represent an innovative and efficient technology in acid reactivity control for carbonate reservoirs. The entrapment of gas within the acid reduces the contact between the acid and the rock surface while significantly reducing the overall reaction rate. This reactivity control will allow deeper and more efficient wormhole formation with less excessive acid consumption and, therefore, a more economical process (Al-Nakhli et al., 2020, 2021). Besides, foamed acids are very effective against the numerous problems of heterogeneous carbonate formations. The specific structure of the foamed acids allows for better distribution of the acid in rocks with different permeabilities, thus ensuring more balanced stimulation of the formation. This homogeneity enhances the depth of acid penetration, even at low injection rates, which is of particular help in formations where uneven acid distribution or near-wellbore spending may reduce the effectiveness of the treatment. Foamed acids, therefore, besides helping to improve stimulation efficiency, also contribute to well productivity in the long term (Bernadiner et al., 1992; Cheng et al., 2002; Zerhboub et al., 1994). This approach has received growing interest in the last decade due to its promising potential for better optimizing acidizing treatments in heterogeneous reservoir environments (Cao et al., 2021).

Numerous studies have investigated wormhole formation using strong acids such as HCL, organic acid, gelled acid, emulsified acid, and chelating acid systems. This study investigates the use of carbonic acid for carbonate reservoir stimulation, focusing on the impact of varying injection rates on wormhole formation. A carbonic acid solution (30% CO_2, 70% deionized water) was injected at rates of 0.2, 0.5, and 1 cm^3/min, with the resulting wormhole structures visualized through CT scanning. Results show that lower injection rates produce more efficient, single wormholes with minimal branching, while higher rates result in more branched, less effective structures. Optimizing the injection rate is essential for improving wormhole efficiency and enhancing flow in carbonate reservoirs.

2. Materials and Methods

2.1. Experimental procedure

The experimental process (Figure 1) began by measuring porosity using a helium porosimeter and estimating permeability with Autoscan. The core sample was dried at 100 °C, vacuumed for three hours, and saturated with fresh water at 2000 psi for 24 hours. Core flooding was then performed, and differential pressure (DP) and pore volume were recorded for breakthrough (PVBT). After flooding, the core was dried, porosity was re-measured, and a CT scan was used to visualize the wormhole.

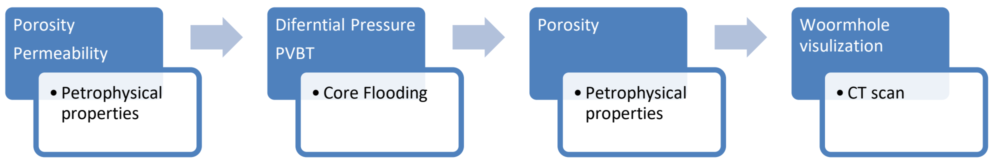

Figure 1
The experimental workflow

2.2. Investigated samples

Three Indiana limestone core samples (2.5 inches long, 1.5 inches in diameter) were used in this study. Initial porosity, measured with helium porosimetry (AP-608) (Table 1). Permeability ranged from 3 to 7 mD. XRD analysis confirmed that the limestone consists entirely of calcite. Each core was wrapped in a shrink tube to prevent cross-flow.

Table 1

Core sample characteristics and properties

Core No.	IR (cm^3/min)	Porosity (%)	Permeability (mD)
IL8	0.2	14.91	3.4
IL12	0.5	15.32	7
IL10	1	15.17	4

2.3. Core flooding

The core flooding experiments involved injecting carbonic acid into Indiana limestone samples to study their behavior under high pressure and temperature. The core samples were housed in a Hastelloy core holder, with an ISCO pump controlling the injection rates of carbonic acid at 0.2, 0.5, and 1 cm^3/min. Before the experiments, the core was sealed, loaded, and subjected to 3,500 psi and 2,000 psi confining and back pressures, respectively. Fresh water was initially injected at varying flow rates to measure the core's permeability. The process was stopped when the acid breakthrough occurred.

2.4. Computed tomography scan

CT scanning uses X-rays to create 2D images, forming a 3D model of the rock. It helps analyze porosity, permeability, and pore structure (Al-Marzouqi, 2018). After flooding, CT scans visualized wormholes, with their volumes estimated through software analysis

3. RESULTS

The core flooding experiments showed significant changes in porosity and permeability across the samples (Figure 2). Sample IL8, subjected to a 0.2 cm^3/min injection rate, had an initial porosity of 14.91%, which increased to 16.01%. The permeability rose from 3.4 mD to infinity, indicating a substantial increase in fluid flow capacity. Similarly, Sample IL12, with an injection rate of 0.5 cm^3/min, showed an increase in porosity, from 15.32% to 16.05%, while its permeability increased from 7 mD to infinity. Sample IL10, injected at a higher rate of 1 cm^3/min, experienced porosity rising from 15.17% to 16.27%, with its permeability reaching infinity. This consistent increase in porosity shows that the injection process was quite effective for pore space enhancement in each of these samples, which can lead to a substantial increase in fluid flow and permeability. The wormhole formation is an important factor in enhancing fluid flow pathways in rock samples. The wormhole formation results derived from core flooding experiments conducted highlight how variations in injection rates may cause wide differences in the extent of the formation and the complexities of the formed wormhole networks. Sample 8 had the lowest injection rate of 0.2 cm³/min and presented a wormhole volume fraction of 0.74%, indicating a more concentrated network that is less branched.

Inlet face after core flooding		
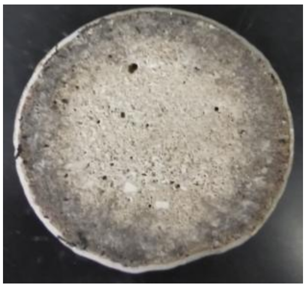		
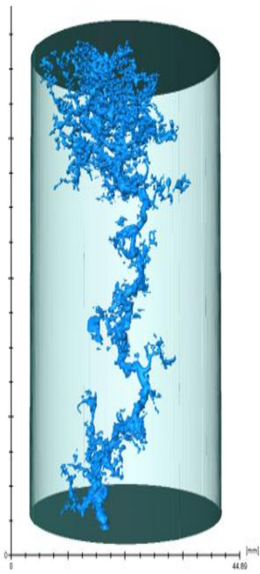	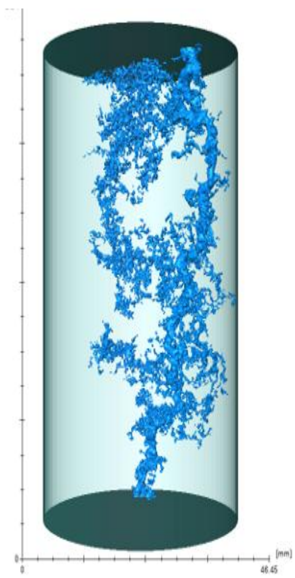	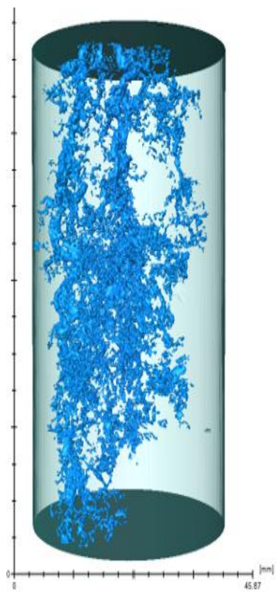
IR = 0.2 cm^3/min	IR = 0.5 cm^3/min	IR = 1 cm^3/min
(A)	(B)	(C)

Figure 2

Wormhole of single core flooding experiments, (A) IL8 (B) IL12 (C) IL10

Sample 10 was treated with the highest injection rate of 1 cm³/min and developed the most in wormhole extent, with a volume fraction of 1.65%. It was characterized by highly branched wormholes all over the core, indicating aggressive fluid penetration. Sample 12, with the middle range injection rate of 0.5 cm³/min, showed a moderately higher wormhole volume fraction of 1.08% with a relatively well-balanced distribution in the wormhole network. These changes represent that with the increase in injection rates, more complicated and highly expanded wormhole structures could be developed, which also coincides with the change rule of permeability and porosity.

4. Discussion and conclusions

The obtained results of core flooding experiments are revealing and mightily informative about the effect of carbonic acid injection into Indiana limestone under high-pressure-high-temperature conditions. The experiments carried out lead to the interpretation that the injection rate largely influences the injected core samples in porosity, permeability, and hence in wormhole formation. Higher injection rates, such as in Sample 10, created incredibly complex and extensive wormhole networks, thus resulting in large increases in permeability. The infinite permeability values for all the samples after flooding reflect this increase, showing that the wormholes greatly enhance the pathways for fluid flow. The porosity increased in all samples, which directly correlates with the formation of wormholes, contributing to the overall void space within the rocks. Higher wormhole volume fractions observed for samples with higher injection rates reinforce this relationship since more aggressive acid injection promotes more aggressive rock dissolution and wormhole development.

The experiments have demonstrated that both higher and lower rates of carbonic acid injection significantly enhance porosity and permeability in Indiana limestone. However, the lower injection rate resulted in the formation of a more dominant and less branched wormhole, making it the more favorable injection rate. This will be important in understanding the behavior of carbonate reservoirs during the acid flooding process and could guide the optimization strategies in the stimulation of reservoirs and enhanced oil recovery operations.

References

Adewunmi, A. A., Solling, T., Sultan, A. S., & Saikia, T. (2022). Emulsified acid systems for oil well stimulation: A review. *Journal of Petroleum Science and Engineering*, 208, p. 109569. https://doi.org/10.1016/j.petrol.2021.109569

Alameedy, U., Al-Haleem, A., Al-Saedi, A., Kadhim, H., & Khan, D. (2023). An experimental study of the effects of matrix acidising on the petrophysical characteristics of carbonate formation. *Materials Today: Proceedings*. https://doi.org/10.1016/j.matpr.2023.04.128

Al-Anazi, H. A., Nasr-El-Din, H. A., & Mohamed, S. K. (1998, February 18). Stimulation of Tight Carbonate Reservoirs Using Acid-in-Diesel Emulsions: Field Application. *SPE Formation Damage Control Conference*. https://doi.org/10.2118/39418-MS

Al-Douri, A. F., Sayed, M. A., Nasr-El-Din, H. A., & Aften, C. (2013, April 8). A New Organic Acid To Stimulate Deep Wells in Carbonate Reservoirs. *SPE International Symposium on Oilfield Chemistry*. https://doi.org/10.2118/164110-MS

Almalichy, A., Aljawad, M. S., Turzo, Z., & Al-Yaseri, A. (2024). A study of the optimum injection rate of carbonic acid during matrix acidizing of carbonate reservoirs: Implications for reducing CO2 emissions. *Heliyon*, 10 (21), e39955. https://doi.org/10.1016/j.heliyon.2024.e39955

Almalichy, A., Turzó, Z., & Alameedy, U. (2022). *Carbonate Rock Matrix Acidizing: A Review of Acid Systems and Reaction Mechanisms*. In: Molnár, Dániel; Molnár, Dóra; Nagy, Adrián Szilárd (szerk.) Tavaszi Szél 2022 / Spring Wind 2022 Tanulmánykötet II. Budapest, Magyarország : Doktoranduszok Országos Szövetsége (DOSZ) (2022) 584 p. pp. 303-313. , 11 p.

Al-Marzouqi, H. (2018). Digital Rock Physics: Using CT Scans to Compute Rock Properties. *IEEE Signal Processing Magazine*, 35 (2), 121–131. https://doi.org/10.1109/MSP.2017.2784459

Al-Nakhli, A., Gizani, M., Baiz, A., & Yami, M. (2021, December 15). An Innovative Acid Diversion Using In-Situ Foam Generation: Experimental and Successful Field Application. *SPE Middle East Oil & Gas Show and Conference*. https://doi.org/10.2118/204879-MS

Al-Nakhli, A., Zefzafy, I., Ahmed, D., & Kharrat, W. (2020, November 9). A Novel Approach to Improve Acid Diversion Utilizing In-Situ Foam Generating Fluids. *Abu Dhabi International Petroleum Exhibition & Conference*. https://doi.org/10.2118/203330-MS

AlOtaibi, F., Dahlan, M., Khaldi, M., AlGhamdi, A., & Al-Hulail, I. (2020, February 12). Evaluation of Inorganic-Crosslinked-Based Gelled Acid System for High-Temperature Applications. *SPE International Conference and Exhibition on Formation Damage Control*. https://doi.org/10.2118/199258-MS

Al-Yaseri, A., Al-Mukainah, H., Yekeen, N., & Al-Qasim, A. S. (2023). Experimental investigation of hydrogen-carbonate reactions via computerized tomography: Implications for underground hydrogen storage. *International Journal of Hydrogen Energy*, 48 (9), pp. 3583–3592. https://doi.org/10.1016/j.ijhydene.2022.10.148

Bernadiner, M. G., Thompson, K. E., & Fogler, H. S. (1992). Effect of Foams Used During Carbonate Acidizing. *SPE Production Engineering*, 7 (04), pp. 350–356. https://doi.org/10.2118/21035-PA

Buijse, M. A., & van Domelen, M. S. (1998, February 18). Novel Application of Emulsified Acids to Matrix Stimulation of Heterogeneous Formations. *SPE Formation Damage Control Conference*. https://doi.org/10.2118/39583-MS

Cao, C., Zhou, F., Cheng, L., Liu, S., Lu, W., & Wang, Q. (2021). A comprehensive method for acid diversion performance evaluation in strongly heterogeneous carbonate reservoirs stimulation using CT. *Journal of Petroleum Science and Engineering*, 203, 108614. https://doi.org/10.1016/j.petrol.2021.108614

Chacon, O. G., & Pournik, M. (2022). Matrix Acidizing in Carbonate Formations. *Processes*, 10 (1), Article 1. https://doi.org/10.3390/pr10010174

Chang, F. F., Nasr-El-Din, H. A., Lindvig, T., & Qiu, X. W. (2008, September 21). *Matrix Acidizing of Carbonate Reservoirs Using Organic Acids and Mixture of HCl and Organic Acids*. SPE Annual Technical Conference and Exhibition. https://doi.org/10.2118/116601-MS

Cheng, L., Kam, S. I., Delshad, M., & Rossen, W. R. (2002). Simulation of Dynamic Foam-Acid Diversion Processes. *SPE Journal*, 7 (03), 316–324. https://doi.org/10.2118/79639-PA

Crowe, C. W., & Miller, B. D. (1974, May 15). New, Low-Viscosity Acid-In-Oil Emulsions Provide High Degree Of Retardation At High Temperature. *SPE Rocky Mountain Regional Meeting*. https://doi.org/10.2118/4937-MS

Frenier, W. W., Wilson, D., Crump, D., & Jones, L. (2000, October 1). Use of Highly Acid-Soluble Chelating Agents in Well Stimulation Services. *SPE Annual Technical Conference and Exhibition*. https://doi.org/10.2118/63242-MS

Lynn, J. D., & Nasr-El-Din, H. A. (2001, February 13). *A core based comparison of the reaction characteristics of emulsified and in-situ gelled acids in low permeability, high temperature, gas bearing carbonates*. SPE International Symposium on Oilfield Chemistry. https://doi.org/10.2118/65386-MS

Ma, L., Fauchille, A.-L., Ansari, H., Chandler, M., Ashby, P., Taylor, K., Pini, R., & Lee, P. D. (2021). Linking multi-scale 3D microstructure to potential enhanced natural gas recovery and subsurface CO2 storage for Bowland shale, UK. *Energy & Environmental Science*, 14 (8), pp. 4481–4498. https://doi.org/10.1039/D0EE03651J

Maheshwari, P., Maxey, J., & Balakotaiah, V. (2014, November 10). Simulation and Analysis of Carbonate Acidization with Gelled and Emulsified Acids. *Abu Dhabi International Petroleum Exhibition and Conference*. https://doi.org/10.2118/171731-MS

Mohammed, A., & Velledits, F. (2024). Microfacies impacts on reservoir heterogeneity of early Cretaceous Yamama carbonate reservoir in South Iraq. *Scientific Reports*, 14 (1), p. 24184. https://doi.org/10.1038/s41598-024-74640-w

Ortega, A. (2015). *Acidizing High-Temperature Carbonate Formations Using Methanesulfonic Acid* [Thesis]. https://oaktrust.library.tamu.edu/handle/1969.1/155026

Ratnakar, R. R., Kalia, N., & Balakotaiah, V. (2012, May 14). Carbonate Matrix Acidizing with Gelled Acids: An Experiment-Based Modeling Study. *SPE International Production and Operations Conference & Exhibition*. https://doi.org/10.2118/154936-MS

Rodrigues, M. A. F., Arruda, G. M., da Silva, D. C., da Costa, F. M. F., de Brito, M. F. P., Antonino, A. C. D., & Wanderley Neto, A. de O. (2021). Application of nonionic surfactant nonylphenol to control acid stimulation in carbonate matrix. *Journal of Petroleum Science and Engineering*, 203, p. 108654. https://doi.org/10.1016/j.petrol.2021.108654

Shank, R. A., & McCartney, T. R. (2013, March 17). Synergistic and Divergent Effects of Surfactants on the Kinetics of Acid Dissolution of Calcium Carbonate Scale. *CORROSION 2013*. https://dx.doi.org/10.5006/C2013-02762

Yan, Y., Xi, Q., Una, C., He, B., Wu, C., & Dou, L. (2019). A novel acidizing technology in carbonate reservoir: In-Situ formation of CO2 foamed acid and its self-diversion. *Colloids and Surfaces A: Physicochemical and Engineering Aspects*, 580, p. 123787. https://doi.org/10.1016/j.colsurfa.2019.123787

Zakaria, A. S., & Nasr-El-Din, H. A. (2016). A Novel Polymer-Assisted Emulsified-Acid System Improves the Efficiency of Carbonate Matrix Acidizing. *SPE Journal*, 21 (03), pp. 1061–1074. https://doi.org/10.2118/173711-PA

Zerhboub, M., Ben-Naceur, K., Touboul, E., & Thomas, R. (1994). Matrix Acidizing: A Novel Approach to Foam Diversion. *SPE Production & Facilities*, 9 (02), pp. 121–126. https://doi.org/10.2118/22854-PA

Geosciences and Engineering, Vol. 13, No. 2 (2025), pp. 75–94.
https://doi.org/10.33030/geosciences.2025.02.006

ASSESSING FLASH FLOOD CONTROL USING UNIVERSAL RISK MATRIX

ANDRÁS DOBAI[1]*, TAMÁS DEÁK[2], ENDRE DOBOS[3]
[1, *]*Institute of Geography and Geoinformatics, University of Miskolc;*
andras.dobai@uni-miskolc.hu
[2]*Institute of Geography and Geoinformatics, University of Miskolc;*
tamas.deak@uni-miskolc.hu
[3]*Institute of Geography and Geoinformatics, University of Miskolc;*
endre.dobos@uni-miskolc.hu
[1]https://orcid.org/0000-0002-5268-0728
[2]https://orcid.org/0009-0001-1360-4159
[3]https://orcid.org/0000-0002-9798-6376

Abstract: Flash floods have a significant impact on both natural and economic environments, making it essential to analyze their causes and develop mitigation strategies. This study evaluated flood mitigation in a selected area using a risk map created through the application of a risk assessment framework and the Analytic Hierarchy Process method, while risk levels were assessed with the Universal Matrix of Risk Analysis. No similar mapping approach and risk assessment had been used in the region before. The resulting map identified the Cseres Valley as a high-risk area. Analysis showed that implementing the proposed mitigation measures could reduce the negative effects of flash floods by about 65%, demonstrating the potential effectiveness of targeted flood protection strategies.

Keywords: *flash flood, Analytic Hierarchy Process, Universal Matrix of Risk Analysis, risk assessment*

1. INTRODUCTION

From the early 2000s to the present, countries worldwide have increasingly been affected by extreme weather events due to climate change. Both droughts, leading to water scarcity, and flash floods, resulting in excessive water accumulation, pose significant challenges to the sustainability of national economies. While drought management is typically handled by the state and can be addressed through water management tools and regulations, the sudden surges of flash floods often lack sufficient mapping methodologies and effective flood protection solutions. Moreover, no established risk assessment methodology applicable to these defense strategies has been developed. Flash floods are created by extreme storms, mostly caused by Mesoscale Convective System (MCS) in watersheds where watercourses may not necessarily exist or where measurable water flow data is missing. Consequently, due to the lack of watershed characteristics and precipitation measurements, considerable technical (engineering, statistical) uncertainty arises when determining the parameters necessary to study this phenomenon. The most significant damage caused by these flood waves occurs in confluence areas, typically in valley-bottom settlements and streambeds. In Hungary, protection against flash flood waves remains unresolved. Legally, these events are classified as *local water damage issue*, meaning that local municipalities are responsible for flood protection (Veres et al., 2021), however, technical assistance can be requested from the Water Management Authority and related agencies (Disaster Management, Civil Protection). These flash floods develop extremely rapidly (within six hours), unlike traditional river floods (such as those on the Sajó, Hernád, and Tisza rivers), where the lead time for preparation is typically 48–72 hours, depending on the forecast. This limited lead time is often insufficient for response agencies to prepare adequately (Szlávik and Kling, 2007; Pappenberger et al., 2006). Due to the lack of preparation time, various preventive measures need to be implemented during so-called peacetime, when no floods are expected (Kaliczka, 1998; Balatonyi, 2022; Szendrei, 2020; Dobai and Dobos, 2022). In addition to introducing new defense methods, local leaders and decision-makers face significant financial challenges in restoring flood-related damage. Furthermore, due to the periodic recurrence of flood events, newly repaired infrastructure (e.g., bridges, roads) may be damaged again by subsequent flood waves, leading to continuous and cumulative costs for municipalities. Therefore, the development of a comprehensive methodology for flash flood risk assessment is essential. Case studies on large watercourses and their catchments have contributed to the development of methodologies and decision-support systems (Zeleňáková, 2009; Zeleňáková et al., 2018; Vágó et al., 2019; Abdel and Islam, 2016; Blistánová et al., 2016). However, a standardized mapping methodology for small catchments has not yet been developed for Northern Hungary. Additionally, the impacts of flood defense measures (e.g., wooden structures, wickerwork, log barriers) and the implementation of flood defense systems have not yet been systematically evaluated. Therefore, the aim of this study is to provide a solution to this problem and assess the impact of potential hydraulic engineering interventions. The development of a flash flood susceptibility mapping and assessment methodology requires the establishment of an integrated GIS database that incorporates region-specific typological characteristics, along with the implementation of a flash flood-related risk assessment system. Since, as discussed earlier, these background databases are not available, the objective of this research is to develop a unique, practical mapping methodology applicable to flood defense and to assess green or brown engineering solutions and their risk evaluation for flood mitigation. A suitable method for mapping is the widely used Analytic Hierarchy Process (AHP), while the Universal Matrix of Risk Analysis (UMRA) is considered appropriate for validation and risk assessment. UMRA specializes in environmental impact assessments and has been proven useful for evaluating flood risks and protection methods in large catchments (Kubečka et al., 2014; Zeleňáková et al., 2017). The application of UMRA is based on the principle that similar risk factors (e.g., settlements, pollution sources) can be identified in small catchment areas as in large ones. However, significantly fewer stressors were considered in the context of flash floods. These methods can provide a reliable assessment for both database creation and risk evaluation.

2. Materials and methods

2.1. Study area

The study area, the Cseres Valley, is located within the watershed of the Harica Stream Basin, near the settlement of Kondó. Geologically, the area lies within the East-Borsod Coal Basin (Figure 1). This basin consists of alternating layers of Neogene marine and lacustrine sediments of various ages, interspersed with Miocene pyroclastic deposits, often exhibiting erosional discordance (Kozák and Püspöki, 1995, 1998; Kozák et al., 1998; Harangi, 2001). Most of the Quaternary sediments have formed because of weathering from these older rock formations. Due to sequential tectonic processes from the Miocene to the Quaternary period, the area has been fragmented into a mosaic-like structure (Kozák and Püspöki, 1995; Pelikán, 2002). These geological and structural characteristics fundamentally shape the area's topography (Sütő, 2001).

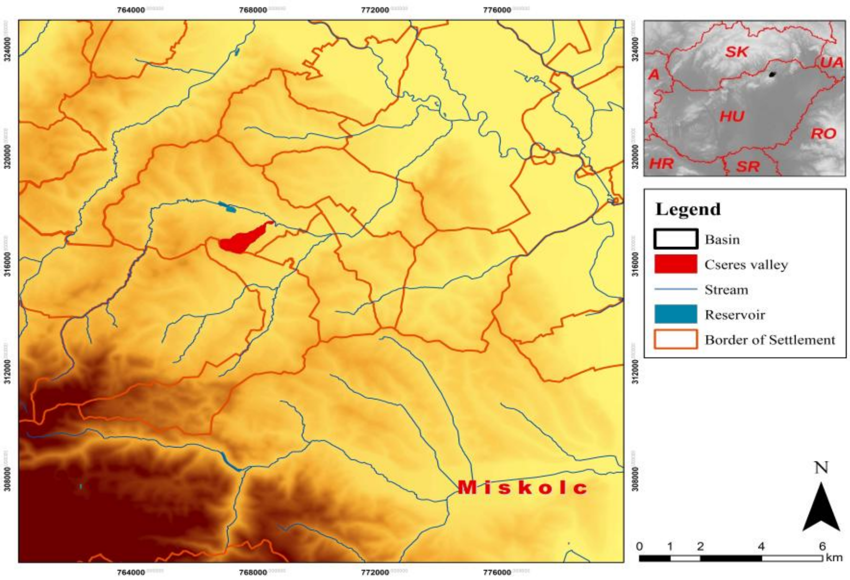

Figure 1
Location of the study area

The entire Cseres Valley belongs to the Egyházasgerge's Formation (eMK), where gravel conglomerate is found at greater depths, overlaid by sand, sandstone, and finer silt and clay near the surface (Gyalog, 1996). The valley itself is V-shaped, spanning 1.6 km in length and 665 m in width, gradually narrowing at the valley bottom, with a watershed area of 0.76 km². The valley is incised into the terrain to depths of 4–5 m in certain locations. Several erosional gullies of varying development levels, primarily caused by rainfall, accompany the valley. Since 2010, these features have also been shaped by periodic flash floods occurring from spring to autumn (Vágó, 2012). The morphometric characteristics of the catchment (Table 1) indicate that, due to the narrowing of the basin towards the outlet, the flash flood wave exhibits an asymmetrical shape, with a gradual rise followed by a rapid recession. This pattern emerges because sudden, high-intensity precipitation events generate large runoff volumes that reach the outflow point early in the event (Galgóczy, 2004).

Table 1

Morphometric characteristics of the Cseres Valley catchment

Catchment area (ca) name	**Cseres Valley, Hungary**		
Area (km^2)	**Water course length (km)**	**Max. length of ca. (km)**	**Max. width of ca. (km)**
0.76	1.80	1.90	0.60
Perimeter of ca. (km)	**Length-to-width ratio (Y)**	**Horton factor-(Rf)**	**Circularity of ca. (Rc)**
4.97	3.17	0.21	0.39
Gravelius factor (K)	**Channel gradient (%)**	**Manning's-n**	**Drainage density (km/km^2)**
1.61	7.17	0.035	2.37

The area falls within the forest soil zone. The soils identified so far being luvisols (Alfisol), stagnic luvisols (Epiaqualfs), and gleysols (Aqualfs). Their common characteristic is their high compactness attributed to land use. Most of the valley has been used primarily as pasture or orchards, with smaller forests found on steeper slopes and in the valleys. Cultivated fields and meadows are located on more suitable areas of the slopes, where the signs of machinery work (machine tracks) are evident and are also reflected in the structure of the soils. Archive maps of the area suggest that land use has remained unchanged for several centuries. The distribution of soil types from higher elevations to lower ones is as follows: strongly eroded brown forest soil with levisage near the hilltops and watershed ridges, predominantly anthropogenic colluvial soil in the middle of the slope due to its local position, eroded and heavily compacted Luvisol on the north- and south-facing slopes. At the valley bottom, Gleysoils repeatedly buried by cyclical flash floods are found, followed by deposited meadow soil rich in anthropogenic materials at the edge of the settlement zone (Dobai and Dobos, 2023). According to climate classifications projected for 2050, the study area is categorized as moderately warm and moderately dry. The annual average temperature ranges from 8.8 °C to 9.3 °C. During the hottest summer days, the average maximum temperature reaches 31–33 °C, whereas on the coldest winter days, the average minimum temperature drops to approximately –17 °C. Annual precipitation amounts to 550–600 mm. The prevailing wind directions are northwest (NW) and southeast (SE), in alignment with the terrain, with an average wind speed of 2.5 m/s (Bihari et al., 2018).

2.2. Presentation of the precipitation caused by extreme precipitation in the study area

Between 2010 and 2019 (with the exception of 2017) precipitation levels capable of causing flash floods were recorded annually in the sample area and its surrounding region (Table 2). The data were obtained from the Hungarian Meteorological Service database and the annual hydrometeorological reports issued by the General Directorate of Water Management of Hungary, as well as records included in the Vis Major protocols of the Hungarian National Bank. Although the table does not encompass all precipitation data (e.g., in 2010, a total of 177.7 mm of precipitation was recorded between May 15 and July 25), it effectively represents the precipitation amounts and characteristic periods impacting the region. The majority of damages were observed in privately owned properties and built infrastructure (e.g., public roads, bridges), with total damages estimated to exceed 50 million HUF (BAZ, 2020; Veres, 2021).

Table 2

24h precipitation totals recorded by GDWM's gauge network

Station	**Homrogd**			
Time of measurment	10. 08. 2018	13. 08. 2019	26. 06. 2020	23. 06. 2019
Precipitation (mm)	87,0	70	65	87,0
Station	**Jávorkút**			
Time of measurment	19. 04. 2017	10. 08. 2018	15. 05. 2010	23. 06. 2019
Precipitation (mm)	97,3	76,4	75	11
Station	**Miskolc-Sajópart**			
Time of measurment	29. 07. 2011	31. 03. 2022	22. 06. 2024	23. 06. 2019
Precipitation (mm)	52	46,9	46,7	28,3
Station	**Múcsony**			
Time of measurment	28. 07. 2016	13. 08. 2019	19. 08. 2015	23. 06. 2019
Precipitation (mm)	90,8	70	60,8	78,3
Station (based on Vis M. report)	**Varbó**			
Time of measurment				23. 06. 2019
Precipitation (mm)				94

Based on the Flood Calculation Guide issued by the General Directorate of Water Management of Hungary, the flood discharges calculated for the study area at the mouth of Harica-Nyögő Creek, with a specific discharge of $Q_5\%$ m³/s km², are as follows: $Q_1\% = 71.0$ m³/s, $Q_3\% = 54.6$ m³/s, $Q_{10}\% = 38.2$ m³/s (Koris, 2021). Although the general water yield data does not justify the construction in the Harica catchment area, which includes the Cseres Valley, a water reservoir with a surface area of 13.6 hectares and a storage capacity of 410,000 m³ was constructed to protect the settlement of Kondó following the flood events caused by the precipitation events of 2010. Although the stormwater reservoir fulfills its purpose and, in accordance with its engineering design, retains and channels the flood waves caused by runoff precipitation, the settlement has continued to experience flooding from smaller surrounding catchments (e.g., the Cseres Valley, Varrom-stream) even after its construction. The causative link, however, has not been conclusively demonstrated, this conclusion could only be drawn based on observations derived from flood protection practices. The solution was provided by a basic mapping methodology (Dobai and Dobos, 2022), which is further developed in current research.

2.3. Presentation of the AHP-based weighting for risk mapping

The Analytic Hierarchy Process (AHP), developed by Thomas L. Saaty, is a decision-making methodology designed for the structured and systematic analysis of complex problems. Within this framework, problems are represented in a hierarchical structure, with the decision goal positioned at the top level, followed by criteria and alternatives. A central feature of the method is pairwise comparison, whereby criteria and alternatives are evaluated along a predefined scale to express their relative importance (Choudhury et al., 2022; Costache et al., 2020). The evaluation process generates a comparison matrix, which is utilized for weight calculation and priority determination. Through its mathematical computations, the AHP method enables the objective ranking of alternatives. Additionally, a consistency ratio (CR) mechanism is incorporated to ensure the internal coherence of the pairwise comparisons (Eroglu and Meral, 2021). For the weighting of map classes, the scale proposed by Saaty was used. AHP-derived weights were calculated for each class in the flash flood susceptibility mapping process, and these weights were subsequently applied to classify the corresponding raster datasets.

2.4. Presentation of the flash flood risk mapping methodology

As the first step of the research, the input data required for mapping and the weights assigned to the classes of the risk map were established since no flash flood susceptibility or risk map had been previously developed for the region. The aim was to produce a minimal yet informative, high-resolution map suitable for practical defense applications. Terrain-derived surface indices (e.g., DEM, channel distance, curvature, aspect) and indices derived from remote sensing (e.g., satellite images, NDWI, NDVI) were utilized, as they are fundamental in risk mapping methodologies (Youssef et al., 2011). However, inclusion of excessive and closely correlated variables (redundant data) was avoided to prevent overburdening the model and reducing predictive performance. Therefore, only parameters contributing novel information to the map were retained. This optimization of input data has been widely documented in the literature (Bui et al., 2019; Youssef and Hegab, 2019; Ngo et al., 2018; Khosravi et al., 2018; Khosravi et al., 2016; Youssef et al., 2016). Layers such as hillshade, which do not provide additional information, and those causing redundancy, such as Stream Power Index (SPI) and Sediment Transport Index (STI) (both based on slope and flow accumulation), were excluded. The aspect layer was also omitted due to the lack of meteorological forecasting systems capable of determining prevailing storm directions. Radar images from the Hungarian Meteorological Service indicated that MCS storm fronts approached the study area from the south on 23. 06. 2019, while on 13. 08. 2019, the front arrived from the east-northeast. Despite these observations, no characteristic storm direction or typical topographical exposure could be determined for this study. Thus, only eight rasters were included: slope, derived from a 5 m-resolution DEM; classified Normalized Difference Vegetation Index NDVI (Dalezios et al., 2001); classified land use/landcover (LULC) layers, generated using Sentinel-2B satellite bands B2 (blue), B3 (green), B4 (red), B8 (NIR), and resampled B5 (VNIR) at 10m resolution; average soil thickness from the AGROTOPO hungarian soil database, Topographic Wetness Index (TWI), slope-weighted flow length (SWFL); time of concentration (Costache 2014), also a texture layer obtained from the E-Soter digital soil mapping methodology with 430 m spatial resolution, covering the CEU area. The E-Soter system, which integrates remote sensing morphological classification and classifies soils according to the WRB system (Dobos et al., 2007), was utilized. Flash floods were found to develop under precipitation intensities above 30 mm/h, depending on initial surface conditions, particularly soil moisture (Luong et al., 2021). During the mapping process, weights were assigned to each class using the Analytic Hierarchy Process (AHP) method. The weights were applied to each raster layer using the ArcMap-Lookup function of the Spatial Analyst toolset, which had been previously prepared and divided into appropriate categories. Then, the weighted values of the various factors were summed using the Spatial Analyst – Raster Calculator to create the weighted index of the hazard map in ArcMap. To homogenize the spatial units, the majority function of the Focal Statistics tool was employed, merging values based on neighboring cells to ensure continuity in map representation and spatial coherence across the calculated zones.

2.5. Assessment of Universal Matrix of Risk Analysis for the proposed flood protection

The construction of the flood protection facility (dam, sheet pile walls) discussed in the introduction requires an Environmental Impact Assessment (EIA). The EIA generally serves as a tool to assist authorities in making decisions regarding project approval and determining the appropriate conditions. As a decision-making instrument, the EIA aims to identify and evaluate the expected environmental consequences of certain planned development activities, with the aim of facilitating informed decision-making and ensuring thorough environmental management (Zeleňáková and Zvijakova, 2011). Among the most appropriate methodologies for such assessments is the Universal Matrix of Risk Analysis (UMRA), a logical-numerical expert method that utilizes a matrix for risk evaluation, assessing the interaction between hazards and vulnerable segments (Zeleňáková et al., 2017). UMRA provides a comprehensive methodology for evaluating risks within environmental and hydrological systems. The framework is structured around three primary components — Probability Index (Pi), Consequence Index (Ci), and Risk Index (Ri) — which collectively enable a systematic quantification and visualization of risk levels. The fundamental principle of the approach is to calculate the Risk Index, which represents the estimated level of risk posed to the environment by the proposed activity (Zeleňáková et al., 2017).

The application of this methodology in the environmental impact assessment of flood mitigation measures enables the evaluation of construction interventions, facilitating the selection of the optimal option during the permitting process. For the calculation of UMRA, the ‘Pi’ probability (ranging from 0.25 to 1) and the ‘Ci’ consequence (ranging from 0.25 to 1) are required, which are then incorporated into the calculation of the individual risk ‘Ri’ for each identified stressor effect on environmental components. A probability indicator and criteria at various levels are proposed for this purpose. Probability is commonly expressed on a scale from 0 to 1, and this scale was applied across four categories (from 0.25 to 1). The calculation of individual risk, denoted as Ri, which is necessary for impact assessment, is conducted using the following equation

$$\mathrm{Ri} = \mathrm{Pi} \times \mathrm{Ci} \tag{1}$$

where
R_i – individual risk associated with the impact of each stressor on environmental components;
P_i – probability of occurrence;
C_i – consequences.

The probability (Pi) and consequence (Ci) of each impact are evaluated and combined to determine the individual risk posed by each stressor to environmental components. Individual risks (Ri) were calculated for all nine identified stressor impacts on environmental components. Risk levels are categorized into four semi-qualitative levels based on the universal matrix of risk analysis: negligible (Ri = 0.0625–0.25); low (Ri = 0.25–0.50); medium (Ri = 0.50–0.75); and high (Ri = 0.75–1.00). The resulting risk index (IR) as the sum of all individual stressor risks (Zeleňáková et al., 2017). The summation in Equation (2) is taken over all stressor impacts (i = 1…n), while j denotes the alternative under evaluation.

$$\mathrm{IR}_j = \sum_{\{i=1\}}^{\{n\}} (\mathrm{P_i} \times \mathrm{C_i}) \tag{2}$$

where
IR – risk index;
P – probability;
C – consequence;
j – rank of the alternative;
n – the number of stressor impacts on environmental components (n = 1… 70);
i – rank of probability and consequence.

In this study, a modified version of the UMRA methodology, adapted to small catchments and flash-flood processes, is applied for the general risk analysis. The modification consists of using a reduced set of flash-flood-relevant UMRA stressors with proportionally lower weights and calculating their effects and associated risks at finer resolution, thereby preserving the aggregated impact on overall risk while better reflecting the rapid and localized nature of flash-flood phenomena. The primary concern associated with flash-flood events is that, although they occur over limited spatial extents, they can generate severe impacts and may result in damage comparable to that caused by riverine floods (e.g., destruction of bridges, damage to wastewater treatment facilities, and further spatial socio-economic impacts).

3. RESULTS

3.1. Result of AHP method

The present study was prompted by practical experiences in flash flood protection, assuming a rainfall intensity above 30 mm/h, which is indicative of the occurrence of flash floods (Luong et al., 2021). Although the detailed analysis was carried out on a 1 km² sample catchment, the risk map was extended to the wider catchments of the Sajó, Bódva and Hernád rivers in order to provide the regional hydrological context of the study area. These larger catchments represent the upstream and downstream environments that influence both the boundary conditions and the potential propagation of flash-flood processes. By including the surrounding river catchments, the applicability of the proposed methodology could also be demonstrated at a broader spatial scale, beyond the small pilot area. The analysis conducted using variable-sized moving windows, together with the assessment of the catchments, is of particular importance, as our previous research demonstrated that six sub-catchments are situated around the settlement of Kondó (Dobai and Dobos, 2022). These catchments are located downstream of the flood-control detention reservoir and therefore constitute potential sources of flash-flood hazard. However, only three of them have critical surface-runoff characteristics. To enable a comprehensive hazard assessment and to accurately define the required input parameters, a detailed analysis encompassing nearly the entire Harica catchment is required. This example further demonstrates the crucial importance of high-spatial-resolution geospatial datasets for both risk mapping and the delineation of risk classes. Adequate spatial detail is essential to capture the heterogeneity of catchment characteristics, to represent local-scale hydrological responses accurately, and ultimately to produce reliable and operationally meaningful hazard assessments. The input raster layers and their flood risk hazard level (Table 3) and AHP values used for weighting were as follows (Table 4).

Table 3

Input rasters for flash flood mapping

Group name	Category (Qty)	Category range	Value range	Flood hazard risk level ranges
Slope (%)	5	min. <5% max. >25%	1–5	very low – very high /karst terrain
LULC	6	min. water max. concrete	0–5	none – very high /karst terrain
NDVI	10	min. water max. concrete	0–5	none – very high /karst terrain
Soil depth (cm)	5	min. >20 cm max. >100 cm	1–5	none – very high /karst terrain
Texture	6	min. water max. clay	0–5	none – high
TWI	5	min. 0.9 max >20	1–5	very low – very high / karst terrain
TCI	3	min. <1h max. >3h	0, 1, 5	none-very high / karst terrain
SWFL	3	min. <1000m	0, 1, 5	none-very high / karst terrain

Table 4

Result of AHP weights for Risk Map

Groups	Slope	NDVI	LULC	Soil depth	Texture	TWI	TCI	SW-FL
AHP weigths	0.36	0.18	0.08	0.035	0.030	0.19	0.09	0.03
Risk matrix statistics	**Consist. Ratio (CR)**	**Consist. Index (CI)**	**λ max**					
	0.022	0.028	8.1					

According to the AHP method, the CR value is 0.02, indicating that the matrix is consistent (Eroglu and Meral, 2021). The individual risk classes were multiplied by the AHP weights, and new classes were generated based on these weights. Finally, they were categorized into four flash flood susceptibility groups (no risk, low risk, medium risk, high risk/karst terrain).

The best results for the distribution of the classes were achieved using the geometric interval and the natural break (Jenks) methods. The Jenks natural breaks classification was particularly suitable because it adapts to the inherent variability of the dataset by identifying statistically meaningful discontinuities in the value distribution (Gui et al., 2025). This allowed the susceptibility classes to follow the actual clustering and skewness present in the flash-flood–related parameters, resulting in more realistic spatial delineation compared to uniform or quantile-based schemes. To further refine the map, manual threshold adjustments were also applied. The resulting map is shown in Figure 2.

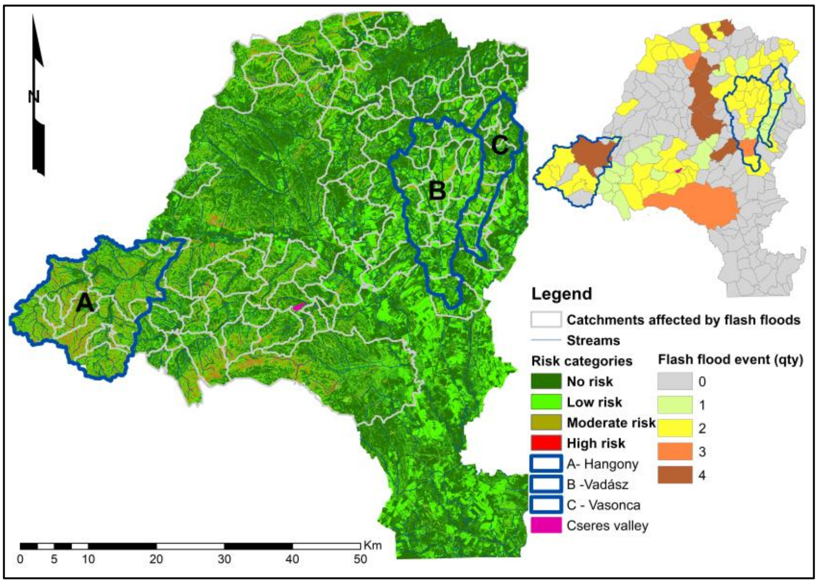

Figure 2

Results of risk mapping and flash flood events (2010–2024)

The results indirectly indicate the geological structure, with the most characteristic areas being the Lower Triassic and Permian limestone (gT1, avT1; nP2) in the Bükk Mountains, and the Middle-Upper Triassic limestone and dolomite (wT2-3m, wT2-3d) formations along the Bódva River (Gyalog, 1996). In contrast, the northern and eastern sections of the risk map (Figure 2) provide an adequate explanation for the occurrence of flash floods within the Hangony-Hódos, Vadász, and Vasonca catchments. For each category, recommended defense methods can be assigned.

In the No Risk and Low Risk areas, it is advisable to review the affected watershed, potentially examining historical records and archival data to verify any past damage caused by major storms or flash floods. In general, for these areas, the maintenance of municipal rainwater drainage systems and local infrastructure (such as road culverts and streambed regulation) is sufficient. It is worth noting, however, that even on small watershed scales (<100 km²), no areas fall exclusively into this category. Additionally, for agricultural lands, appropriate agrotechnology and adherence to plowing and soil cultivation boundaries are recommended to mitigate risks related to erosion and improve runoff conditions, as these factors pose significant risks to the watershed (Dobai and Dobos, 2023). In the Medium Risk category, it is advisable to construct small dams, weirs, and other hillside structures made from local materials, either at the target area or at runoff points, while considering the potential for water retention in the landscape. These structures, which may include permanent installations, could require water management permits (Balatonyi, 2022; Sušnik et al., 2022). For areas classified as High Risk, Very High Risk, or Karst Terrain, detailed surveys, risk assessments, and environmental impact studies are necessary. Water defense solutions in these areas must align with these evaluations and may also incorporate the measures suggested for the previous categories. Additionally, robust, low-maintenance, and cost-effective solutions should be identified. Such measures may include sills, sheet piles, or constructions made of building stones placed in Gabion mesh, designed to increase surface accumulation time and slow runoff. Among agrotechnological practices, the establishment of terraced cultivation is a viable option (Alessandro et al., 2002). Municipal defences should also be addressed. Due to the lack of preparation time, traditional labour-intensive methods, such as sandbag defences, are impractical. Instead, the construction of modern, temporary barriers made of plastic materials that can be easily and quickly deployed in urban areas is recommended. The hazard categories of the Cseres Valley and its surroundings, which constitute the study area, have been identified in previous studies: a total of six sub-catchments are located downstream of the aforementioned flood reservoir, three of which exhibit critical surface runoff characteristics based on runoff condition assessments (Dobai and Dobos, 2022). The results of earlier analyses have been further refined by the current mapping: the ‘no risk’ and ‘low risk’ categories together constitute 47.12% (361.45 m²) of the total watershed area, while the ‘medium risk’ category accounts for 50.88% (390.32 m²), the ‘high risk’ category for 1.92% (14.72 m²), and the ‘very high risk’ category for 0.08% (0.625 m²). The predominance of medium-risk areas, combined with the proximity of the valley’s discharge point to the settlement, explains the high level of vulnerability to flash floods in the region. Within the catchment, the most optimal solution for flash flood mitigation was found to be the multi-stage installation of 116 Larssen-type sheet piles, measuring 8.00 × 6.00 × 0.6 meters each, with a total length of 70 meters distributed across three locations (Dobai and Dobos, 2022). Following chapters, the risk-reducing effects of sheet pile walls installed in the Cseres Valley will be evaluated using the UMRA method.

3.2. Results of UMRA

Understanding flood-related risks requires a systematic assessment of the environmental, social, and landscape components that may be affected during an extreme hydrological event. Within this framework, the Cseres Valley serves as a representative case study, where the interaction between natural processes and human activities creates a complex risk environment. In this context, individual risk values (Ri) were calculated based on documented damage reports and existing flood-mitigation practices. These risks were evaluated through a set of environmental stressors identified in the literature (Zeleňáková et al., 2017). Accordingly, nine primary stress factors were defined (Table 5): population (1), water conditions (2), soil (3), flora, fauna, and their habitats (4), landscape structure (5), protected areas and their buffer zones (6), urban areas and land use (7), the territorial system of ecological stability (TSES) (8), and cultural and historical heritage, including intangible cultural values (9). Two scenarios were considered for each stressor: ver. 1, representing ineffective flood protection, and ver. 2, representing effective flood protection.

Table 5
Comparative assessment of flood risk for scenarios

The impact of the stressor on individual components	**Determining probabilities (Pi) ver 1 / ver 2** (ver. 1: ineffective flood protection / ver. 2: effective flood protection)		**Determining consequences (Ci) ver 1 / ver 2**		**Calculating risk (Ri) ver 1 / ver 2**	
Impact on 1	local flood hazard risk – medium		health consequences of flooding			
	0.25	0.25	0.75	0.75	0.19	0.19
Impact on 2	high-level flood alerts (qty/ per year)		water discharge Q (m³/s) – maximum Q			
	0.10	0.10	1	1	0.1	0.1
Impact on 3	condition of flood-protection structures		soil permeability			
	1	0.25	0.25	0.18	0.25	0.047
Impact on 4	local flood hazard risk – medium		vulnerability of fauna, flora, and their habitats (–)			
	0.25	0.25	0.125	0.125	0.0313	0.0313

Impact on 5	local flood hazard risk – medium		changes in landscape structure			
	0.25	0.25	0.25	0.25	0.063	0.063
Impact on 6	local flood hazard risk – medium		(ver. 1) / (ver. 2)		extent of impacts outside the buffer zone	
	0.25	0.25	0.75	0	0.188	0
Impact on 7	condition of flood-protection structures		impact on the local ecological stability system			
	0.75	0.25	0.13	0	0.09	0
Impact on 8	local flood hazard risk – in urban areas		(ver. 1) / (ver. 2)		flooded area: 1–50 km²	
	0.5	0.5	0.5	0	0.25	0
Impact on 9	local flood hazard risk – medium		quantity of affected values			
	0.25	0.25	0.25	0.25	0.06	0.06
Version 1 – without protection structure	∑ PI = 3.60		∑ CI = 4.01		∑ IR = 1.22	
Version 2 – with protection structure	∑ PI = 2.35		∑ CI = 2.56		∑ IR = 0.49	

Two distinct scenarios were analyzed: the current state, which lacks flood protection measures and has a baseline risk value of 1.22, and the scenario where a sheet pile wall system was installed, resulting in a risk value of 0.49 (it is 59.8% decrease), indicating a reduction to below the risk threshold. The validation of these results is performed by comparing them with previously occurred flood disasters. The Hungarian National Bank is legally mandated to prepare so-called vis Major reports for insurance companies and municipal leadership related to flash floods and other events (e.g., windstorm, earthquake). If the damage recorded in past events shows a similar pattern to the calculated Ri values, the modeled effect of the proposed measures (e.g., a sheet pile wall) can be considered reliable. That is, if the model predicts that the flood protection reduces the risk to 0.49, and the historical event data indicates that the Ri without effective protection would have been approximately 1.22, the consistency validates the accuracy of the estimation. Thus, the reports allow for the quantification of the direction of the flash flood wave and the extent of damage, which aligns with the findings obtained during the analysis.

Flash floods can be summarized in terms of probability and impact (Pi-Ci) for risk assessment as follows. The probability of the phenomenon has increased frequency in the last two decades, with an expected value ranging from 0.50 to 0.70, and, in the event of occurrence, it is associated with extreme water discharge. However, regardless of the probability of occurrence, the level of damage is consistently significant (ranging between 0.75 and 1), especially when the storm occurs on saturated or impermeable soil. Real storm events indicate that the greatest destruction is caused when MCR zones experience a return period of 12–24 hours (e.g., summer of 2010, 2019). Since the phenomenon primarily occurs from early to late summer, land cover — regardless of storm frequency — has a significant impact on surface runoff retention. Practical flood protection experience has shown that the flood wave predominantly flows along concentrated drainage networks (such as dirt roads, pedestrian paths, and roadways) in addition to streambed and watercourses, therefore, complex landscapes must be considered. Thus, with the construction of the flood protection system, a low-risk level (0.49) will be achieved for the valley and the surrounding natural and socio-economic landscapes. The implementation of the flood protection system will result in the elimination or significant reduction of the vulnerability of stressors, such as buffer zones, TSES, and man-made infrastructure (bridges, roads, etc.). The impact of the phenomenon could be reduced by the proportion of arable land; however, due to eroded surfaces, improper agrotechnological practices, and land management, agricultural areas (on different genetic soil types) are typically compacted and severely eroded. Similarly, the degree of forest cover could exert an effect, but the developmental stage of the forest associations and their age significantly affect surface infiltration. Collectively, these factors contribute to the determination of both preventive and reactive mitigation measures (such as risk mapping and natural embankments made of local materials), which can potentially reduce flood risk levels (Sušnik et al., 2022; Balatonyi, 2022).

4. Discussion and conclusions

Regarding the mapping methodology, the interpretation of the study results is limited to Hungarian territories, as local risk assessment maps lack a methodological framework that incorporates such diverse input data. An exception is the flood sensitivity mapping methodology proposed by Sarkadi et al. (2022), which, although targeting a national scale, also incorporates finer spatial resolution and is based on equally weighted conditional factors. A comparison of the two methodologies was conducted, and the general watershed-based flash flood susceptibility index (FFSI_ws) and the settlement-level index (FFSI_smax), based on the maximum raster value, showed similarity to the present method. These results suggest that, despite differences in the spatial resolution of the input data, the maps may still provide a suitable basis for the development of future risk mapping methodologies (Dobai and Dobos, 2025). At the level of international methodologies, the input data's AHP weights fall within a similar range (Grozavu et al., 2017; Kanani-Sadat et al., 2019). However, this research focuses on eight input variables rather than the average of 10–12, primarily concentrating on surface runoff to avoid redundant data. In this study, the detailed classification of NDVI and TCI layers proved to be particularly useful. The strengths of the methodology include improved spatial resolution, interpretability at the small catchment level, and the first-time use of a region-specific digital soil map in mapping rather than relying solely on general national soil databases. The methodology's weakness is that it requires further development. One potential solution is to analyze NDVI changes during the March–October period and only identify areas with stable floodwave-reducing characteristics as those where high NDVI values change minimally. Another potential improvement is comparing forestry databases with NDVI values, as forest types and planting ages may vary, making it inappropriate to treat specific areas as uniform forests (Korchagina et al., 2020). These refinements would require significant storage capacity and dedicated research. However, once addressed, they could provide a robust foundation for AI methodologies (e.g., neural networks, Random Forest). Despite its drawbacks, the methodology can significantly support flood defense agencies and municipalities, complemented by research findings specialized in calculating flash flood discharge (Dobai et al., 2024).

Municipalities, depending on the affected settlements, are responsible for flash-flood protection, as technical defense measures receive only partial support from the relevant authorities (e.g., water directorate, police, disaster management agencies, etc). Given economic sustainability concerns and the increasing frequency of extreme weather events, an innovative shift in perspective is necessary. This study presents an interdisciplinary methodology to mitigate the harmful impacts of flash floods in basin catchments. Using high-resolution spatial data, derived DEM indices, and statistical weighting methods (AHP), a reliable mapping database can be developed to identify flash flood hazards. The UMRA methodology demonstrates that its matrix properties enable effective application, particularly as stress factors (e.g., municipal waste storage, wastewater treatment plants, and critical infrastructure) are also present in smaller watersheds. The method generates mapping layers, assesses environmental risks, identifies locations, recommends defense strategies, and evaluates risks associated with proposed mitigation measures. Based on previous damage assessments (approx. HUF 50 million), mitigation costs could be covered for a fraction of the corresponding insurance payouts (approx. 8–10 million HUF) (Veres et al., 2021). As a result, this approach can significantly reduce municipal and national budgetary expenditures while positively impacting the natural systems across the region.

ACKNOWLEDGMENTS

The research was carried out with funding by the 2020-1.1.2-PIACI-KFI: Support for Market-Driven Research, Development, and Innovation Projects - Development of an ICT Platform for Supporting Soil Information-Driven Agriculture for Managing and Optimizing Agricultural Production and Monitoring the Effects on the Soil System and funding by the RRF-2.3.1-21-2022-00014 Climate Change Multidisciplinary National Laboratory for Climate Change.

REFERENCES

Abdel, R. E. and Eljack, I. H. (2016). DAM Site Selection Using GIS Techniques and remote sensing to Minimize Flash Floods in East Nile Locality (Soba Valley)-Khartoum State. *International Journal of Engineering Science Invention*, Vol. 5, Issue 12, December 2016, pp. 50–61.

Colombo, A. G., Hervás, J., Vetere Arellano A. L. (2002). *Guidelines on Flash Flood Prevention and Mitigation – NEDIES project*. EUR 20386 EN, 64 p.

Balatonyi, L., Lengyel B., Berger Á. (2022). Natura-based solution as water managment measure in Hungary. *Modern Geográfia*, Vol. 17, Issue 1, pp. 73–85. https://doi.org/10.15170/MG.2022.17.01.05

BAZ – Borsod-Abaúj-Zemplén Megyei Katasztrófavédelmi Igazgatóság (2020). „A", jelű Előzetes Helyszíni vizsgálat jegyzőkönyvei 2010–2020, Kondó település Polgármesteri Hivatalának adattára, pp 4–5. Magyar Állam Kincstár *94/2015 (XII.23) sz. Korm. rendelete – Vis maior rendelet alapján*

Bihari Z., Babolcsai Gy., Bartholy J., Ferenczi Z., Gerhátné, K. J., Haszpra L., Homokiné U. K., Kovács T., Lakatos M., Németh Á., Pongrácz R., Putsay M., Szabó P. and Szépszó G. (2018). Éghajlat. In KOCSIS K. (ed.): *Magyarország Nemzeti Atlasza 2. Természeti környezet. (The National Atlas of Hungary, Vol. 2: Natural Environment*). HUN-REN CSFK Földrajztudományi Intézet, pp. 58–69.

Blistánová, M., Zeleňáková, M., Blistan, P., Ferencz, V. (2016). Assessment of flood vulnerability in Bodva river basin, Slovakia. *Acta Montanistica Slovaca*, Vol. 21, No 1, pp. 19–28.

Bui, D. T., Tsangaratos, P., Ngo, P. T., Pham, T. D. and Pham, B. T. (2019). Flash flood susceptibility modeling using an optomized fuzzy rule based feature selection technique and tree based ensemble methods. *Sci. Total Environ.*, Vol. 668, pp. 1038–1054. 10.1016/j.scitotenv.2019.02.422

Choudhury S., Basak, A., Biswas, S., Das, J. (2022). Flash Flood Susceptibility Mapping Using GIS-Based AHP Method, *Spatial Modelling of Flood Risk and Flood Hzarads*, https://doi.org/10.1007/978-3-030-94544-2_8.

Costache, R. (2014). Using gis techniques for assessing lag time and concentration time in small river basins. Case study: Pecineaga river basin, Romania. *Geographia Technica*, 9, pp. 31–38.

Costache, R., Pham, Q. B, Sharifi, E., Linh, N. T. T., Abba, S. I., Vojtek, M., Vojteková, J. Nhi, P. T. T. Khoi, D. N. (2020). Flash-Flood Susceptibility Assessment Using Multi-Criteria Decision Making and Machine Learning Supported by Remote Sensing and GIS Techniques. *Remote Sens.*, 12, 106. https://doi.org/10.3390/rs12010106

Dalezios, N., Domenikiotis C., Kalaitzidis C. (2001). Cotton yield estimation based on NOAA/AVHRR produced NDVI. *Physics and Chemistry of the Earth, Part B: Hydrology, Oceans and Atmosphere*, 26, pp. 247–251. https://doi.org10.1016/S1464-1909(00)00247-1.

Dobai A. and Dobos E. (2022). Hegy és dombvidéki kisvízgyűjtőkön kialakuló árhullámok elleni védekezés támogatása térinformatikai módszerekkel. *Debreceni Egyetem, Térinformatikai Konferencia és Szakkiállítás kiadványa*, pp. 109–117.

Dobai A. and Dobos E. (2023). Beszivárgás vizsgálatok a Cseres-völgyben. *Talajvédelem*, pp. 40–55., 16 p.

Dobai A., Dobos E. (2025). A villámárvíz kockázati térképezési módszertan fejlesztése Észak-Magyarországi dombsági területeken. *Hidrológia Közlöny*, 105. évf., 2. https://doi.org/10.59258/hk.19231

Dobai A., Vágó J., Hegedűs A. Kovács K. Z., Pecsmány P., Seres A., Dobos E. (2024). GIS and soil property-based development of runoff modeling to assess the capacity of urban drainage systems for flash floods, *Hungarian Geographical Bulletin*, 73 (4), pp. 379–394. doi: 10.15201/hungeobull.73.4.3

Dobos, E., Daroussin, J. and Montanarella, L. (2007). A quantitative procedure for building physiographic units for the European SOTER database. In Peckham, R. and Jordan GY. (ed.): *Digital Terrain Modelling*. Lecture Notes in Geoinformation and Cartography. Berlin, Heidelberg, Springer, pp. 227–258.

Eroglu, E. and Meral, A. (2021). Evaluation of flood risk analyses with AHP, Kriging, and weighted sum models: example of Çapakçur, Yeşilköy, and Yamaç microcatchments, *Environmental Monitoring and Assessment*, 193 (8). https://doi.org/10.1007/s10661-021-09282-w

Galgóczy, Zs. (2004). Morfometriai paraméterek vizsgálata a Nagy-Szamos forrásvidékén. *Földrajzi Közlemények*, 128/1–4, pp. 89–103.

Gui, R., Song, W., Lv, J., Lu, Y., Liu, H., Feng, T., & Linghu, S. (2025). Digital Elevation Model-Driven River Channel Boundary Monitoring Using the Natural Breaks (Jenks) Method. *Remote Sensing*, 17 (6), p. 1092. https://doi.org/10.3390/rs17061092

Grozavu, A., Patriche, C., Mihai, F. (2017). Application of AHP method for mapping slope geomorphic phenomena. *Conference Proceedings (vol. 17) on Informatics, geoinfromatics and remote sensing*, Issue 23, pp. 377–384. https://doi.org/10.5593/sgem2017/23/S11.046

Gyalog, L. (1996). *A Földtani térképek jelkulcsa és a rétegtani egységek rövid leírása*. MÁFI kiadvány, Budapest, 187 p.

Harangi, SZ. (2001). Neogene to Quaternary Volcanism of the Carpathian-Pannonian Region. *Acta Geologica Hungarica*, 44 (2–3), pp. 223–258.

Jourde , H. Roesch A., Gunot V. Bailly-Compte V. (2005). Dynamics and contribution of karst groundwater to surface flow during Mediterranean flodd. *Proc. Int. Symp. Water Resour*, pp. 133–138. https://doi.org/10.1007/s00254-006-0386-y

Kaliczka L. (1998). *Hegy és dombvidéki vízrendezés*. Baja, pp. 90–95.

Kanani-Sadat Y., Arabsheibani R., Karimipour F., Nasseri M. (2019). A new approach to flood susceptibility assessment in data-scarce and ungauged regions based on GIS-based hybrid multi criteria decision-making method. *Journal of Hydrology*, 572, pp. 17–31. https://doi.org/10.1016/j.jhydrol.2019.02.034

Khosravi, K., Pourghasemi, H. R., Chapi, K. and Bahri, M. (2016). Flash flood susceptibility analysis and its mapping using different bivariate models in Iran: a comparison between Shannon's entropy, statistical index, and weighting factor models. *Environ. Monit. Assess*., p. 188.

Khosravi, K., Pham, B. T., Chapi, K., Shirzadi, A., Shahabi, H., Revhaug, I., Prakash, I., Tien Bui, D., (2018). A comparative assessment of decision trees algorithms for flash flood susceptibility modeling at Harazd watershed, northern. *Iran Sci. Total Environ*., 627 pp. 744–55. https://doi.org/10.1016/j.scitotenv.2018.01.266

Korchagina, I. A., Goleva, O. G., Savchenko, Y. Y., Bozhikov, T. S. (2020). The use of geographic information systems for forest monitoring. *Journal of Physics*, *Conference Series 1515*, p. 032077. https://doi.org/10.1088/1742-6596/1515/3/032077

Koris, K. (2021). The new Hungarian empirical flood calculation guide has been completed, the OVF-2020. *Hungarian Journal of Hydrology*, 101, pp. 13–19.

Kozák, M. and Püspöki, Z. (1995). Correlative relationship between denudational periods and sedimentation in the forelands of the Bükk Mts. (NE Hungary). In *CBGA XV. Congress*. Athen, CBGA, pp. 340–345.

Kozák, M., Püspöki, Z., Piros, O. and László, A. (1998). The structural position of the Bükk Mountains based on tectono- and pebble stratigraphic analyses. In *CBGA XVI. Congress*, Wien, CBGA, p. 303.

Kubečka K., Vlček O., Kubečková D., Pieszka D. (2014). Utilization of Risk Analysis Methods in Decision-Making Process on Fitness of Rehabilitation, *Advanced Materials Research*., 899, pp. 568–571.

Luong, T. T., Pöschmann, J., Kronenberg, R., Bernhofer, C. (2021). Rainfall Threshold for Flash Flood Warning Based on Model Output of Soil Moisture: Case Study Wernersbach, Germany. *Water*, 13. https://doi.org/10.3390/w13081061

Ngo, P. T., Hoang, N., Pradhan, B. (2018). A Novel Hybrid Swarm Optimized Multilayer Neural Tropical Areas Using Sentinel-1 SAR Imagery and geospatial data. *Sensors*, 2018 Oct 31, 18 (11), p. 3704. https://doi.org/10.3390/s18113704

Pappenberger, F., Matgen, P., Beven, K. J., Henry, J. B., Pfister, L. (2006). Influence of uncertain boundary conditions and model structure on flood inundation predictions. *Adv. Water Resources*, 29 (10), pp. 1430–1449. https://doi.org/10.1016/j.advwatres.2005.11.012

Pelikán, P. (2002). Földtani felépítés, rétegtani áttekintés (Geological structure, stratigraphic overview). In *A Bükki Nemzeti Park*. Ed.: Baráz Cs., Eger Bükki Nemzeti Park Igazgatóság, pp. 23–49.

Sarkadi, N., Pirkhoffer, E., Lóczy, D., Balatonyi L., Geresdi I., Fábián Sz., Varga G., Balogh R., Gradwohl-Valkay A., Halmai Á., Czigány Sz. (2022). Generation of a flood susceptibility map of evenly weighted conditioning factors for Hungary. *Geographica Pannonica*, 26 (3), pp. 200–214. https://doi.org/10.5937/gp26-3896

Sušnik, J., Masia, S., Kravčík, M., Pokorný, J., Hesslerová, P. (2022). Costs and benefits of landscape-based water retention measures as nature-based solutions to mitigating climate impacts in eastern Germany, Czech Republic, and Slovakia. *Land Degradation & Development*, 33 (16), pp. 3074–3087. https://doi.org/10.1002/ldr.4373

Sütő, L. (2001). A felszín alatti bányászat domborzatra gyakorolt hatásai a Kelet-Borsodi-szénmedencében (Effects of subsurface mining on topography in the Eastern Borsod Coal Basin). In *Magyar Földrajzi Konferencia: A földrajz eredményei az új évezred küszöbén*. Ed.: Dormány, G.I., Szeged, pp. 1–20.

Szendrei R. (2020). Új technológiák a vízkárelhárításban – Töltésfejlesztés során megnyitott védvonal árvízvédelmi készültséget megelőző visszazárása rossz helyi időjárási viszonyok esetén, *Nemzeti Közszolgálati Egyetem, Víztudományi Kar,* pp. 43–50

Szlávik, L. and Kling, Z. (2007). *Nagycsapadékok és helyi vízkárelhárítási események előfordulása hazánkban* (Occurrence of intense rainfall and hydrologic events in Hungary). MHT Országos Vándorgyűlés kiadványa, Budapest.

Vágó, J. (2012). *A kőzetminőség szerepe a Bükkalja völgy- és vízhálózatának kialakulásában*. PhD értekezés*,* Miskolc, pp. 18–20.

Vágó, J., Dobos, E., Blistan, P., Zelenakova, M., Ladányi, R., Kiss, L. (2019). Flood- and logistical modeling in the Hernad watershed (Műszaki Tudomány az Észak-keleti magyarországi régióban). Conference Book, pp. 420–423. https://doi.org/10.26649/musci.2019.003

Veres, D., Fejes, G., Danyi, R., Halmai, L., Hegyi, Z. (2021). *Vízmegtartó megoldások a hazai vízgazdálkodásban*. Megalapozó tanulmány, IFE16 CCA/ HU/000115 project, 32 p.

Youssef, A. M., Pradhan, B., Hassan, A. M. (2011). Flash flood risk estimation along the St. Katherine road, southern Sinai, Egypt using GIS based morphometry and satellite imagery. *Environmental Earth Sciences*, 62 (3), pp. 611–623. https://doi.org/10.1007/s12665-010-0551-1

Youssef, A. M., Pradhan, B., Sefry, S. A. (2016). Flash flood susceptibility assessment in Jeddah city (Kingdom of Saudi Arabia) using bivariate and multivariate statistical models. *Environ. Earth Sci.*, 75. https://doi.org/10.1007/s12665-015-4830-8

Youssef, A. M. and Hegab, M. A. (2019). Flood-Hazard Assessment Modeling Using Multicriteria Analysis and GIS: A Case Study — Ras Gharib Area, Egypt. *Spatial Modeling in GIS and R for Earth and Environmental Sciences*, pp 229–257. https://doi.org/10.1016/B978-0-12-815226-3.00010-7

Zeleňáková, M. (2009). Preliminary flood risk assessment in the Hornád watershed. *WIT Transactions on Ecology and the Environment*, Vol. 124, p. 32. https://doi.org/10.2495/RM090021

Zeleňáková, M., Zvijakova, L. (2011). Environmental Impact Assessment in context of water structures. *The 8th International Conference Environmental Engineering*, Vilnius, Lithuania, 19–20 May 2011, pp. 499–504.

Zeleňakova, M., Zvijakova, .L., Singovszka, Eva. (2017). Universal Matrix of Risk Analysis method for flood mitigation measures in Vysna Hutka, Slovakia, *Fresenius environmental bulletin*, 26 (2), pp. 1216–1224.

Zeleňáková, M., Dobos E., Kovácová L., Vágó J., Abu-Hashim M., Fijko R., Purcz, P. (2018). Flood vulnerability assessment of Bodva cross border river basin. *Acta Montanistica Slovaca*, Vol. 23, No 1, pp. 53–61.

Geosciences and Engineering, Vol. 13, No.2 (2025), pp. 95–103.
https://doi.org/10.33030/geosciences.2025.02.007

COMPARISON OF TRUSS BRIDGE STRUCTURES DESIGNED FOR CONVEYOR BELT SYSTEMS

ZOLTÁN VIRÁG[1], SÁNDOR SZIRBIK[2, *]
[1]*Institute of Mining and Energy, University of Miskolc; zoltan.virag@uni.miskolc.hu*
[2, *]*Institute of Applied Mechanics, University of Miskolc; sandor.szirbik@uni.miskolc.hu*
[1]https://orcid.org/0000-0003-2259-8878
[2]https://orcid.org/0000-0002-7757-3750

Abstract: In open-pit mines, the installation of conveyor belt tracks may require conveyor bridges to span the terrain or existing structures. The paper compares the structural design options for truss bridge structures, with a particular focus on existing, recycled structures and prefabricated, modular elements. Three-dimensional finite element simulations were used to verify the first option, which is an existing structure meant for reuse to look at the natural frequencies, stress distributions, and deformed shapes. These results highlight the importance of investigating the vibrations caused by the movement of the conveyor belt and the wear of the rollers. The other option examined is a commercial solution based on a Bailey bridge, which is a portable, prefabricated, modular truss bridge designed for quick assembly without heavy equipment. The advantage of the modular design is that the structure can be reinforced by combining the elements, thereby increasing operational safety and economy.

Keywords: *bridge for conveyor system, truss structure, FEA, modal analysis*

1. Introduction

In open-pit mining operations, the installation of a conveyor bridge may serve multiple purposes. Various materials can be efficiently transported using conveyor belts in mining operations, but site-specific terrain conditions, such as crossing working pits or other conveyor systems, often pose challenges during installation. The study focuses on comparing structural design options for the conveyor bridge truss used to support long-distance conveyor belts. The interconnected triangular arrangements in the truss make the structure strong and lightweight.

The bridging solution can be achieved either by reusing an existing truss structure, originally designed for different material transport purposes and requiring modification, or by employing rapidly deployable, prefabricated modular bridge frameworks. Truss bridges are primarily evaluated through strength calculations and buckling checks of compressed members. An additional consideration is the analysis of vibration effects, which are consistently problematic in conveyor belt routing. For rapidly deployable modular bridges made of mobile components, decision-making involves not only mechanical considerations but also economic factors alongside existing product specifications.

Ladányi (2018) presented results for an existing structure intended for reuse, where the spatial framework was simplified as a planar truss for strength verification.

The required parameters were determined primarily through manual calculations based on theoretical considerations. These calculations can be refined by reducing the load distribution obtained from finite element analysis (FEA) to a planar model of the bridge. Szirbik et al. (2023) further investigated the structure by making a 3D model, providing an opportunity to also study vibrational behavior (Szirbik et al., 2024).

The eigenvalue extraction used to calculate eigenfrequencies and mode shapes is based on the Lanczos iteration method (Bathe, 1996). The modal analysis starts with higher numerical accuracy eigenvalue calculations, followed by the generation of mode shapes. The natural frequencies and associated mode shapes can be used later to analyze the effects of dynamic loads on the structure, such as forced vibration analysis. The bridge structures under study support a conveyor system connected to framework elements, which are subjected to transient vibrations induced by the belt's motion. These vibrations may arise from the wear or failure of conveyor belt rollers, acting as excitation sources. Knowledge of the structure's natural frequencies is critical for managing the vibrations under any external effect. The slender member forming the bridge framework inherently causes low natural frequencies, making such structures easily excitable and requiring regular monitoring. In frameworks exposed to excitations due to conveyor-belt motion, resonance catastrophe may occur if the excitation frequency matches any structure's natural frequency. Such resonance can lead to failure, typically manifested as fractures in the weakest components, disrupting the mechanical transport system functionality. Due to the potential hazards of resonance catastrophes, vibration analyses are conducted on various mining equipment, such as excavators and disc-cutting rock extraction machines, as reported by Popescu et al. (2020) and Wijaya et al. (2022).

The costs of modifying an existing framework must be compared with the price, load-bearing capacity, installation costs, and dimensions of an alternative mobile bridge, as well as certain comparable mechanical properties.

2. STRUCTURAL DESIGNS

An alternative to design is an existing conveyor bridge that has been repeatedly utilized in open-pit mining operations to facilitate the installation of conveyor belts for transporting overburden and lignite. The other alternative is a solution constructed from mobile, prefabricated elements with specified manufacturer dimensions. The purpose of the structure is to avoid level intersections of conveyor belts and to bridge working pits during mining operations at low cost.

The truss structure of the first solution has undergone multiple modifications and reinforcements, resulting in its current examined configuration, which features an asymmetric design due to these developments. The structure, with principal dimensions of 23 m in length, 3 m in width, and 2.3 m in height, consists of ten equal-length segments. The diagonal cross-braces are oriented perpendicular to each other; however, unlike conventional designs, the arrangement is asymmetric, as illustrated in Figure 1. Specifically, the orientation of the cross-braces is identical in six cells but opposite in the other four. Wind bracing trusses are present at both the top and bottom of the structure. The conveyor bridge is reinforced at both ends by robust portal frames, and the entire structure is constructed using welded connections.

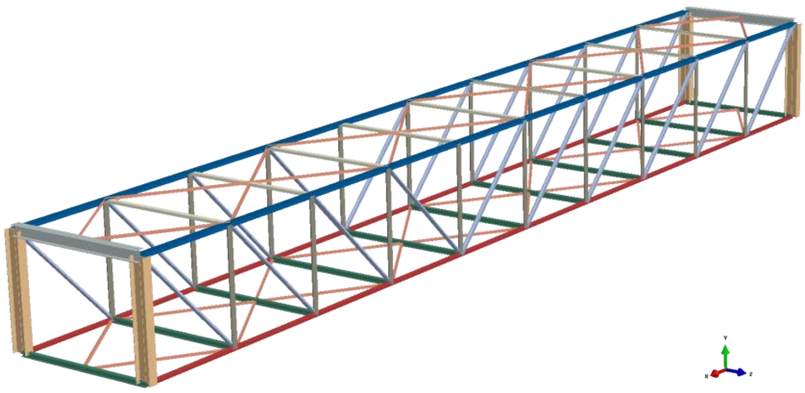

Figure 1
Geometry of the welded truss bridge structure in 3D

During the design of the welded truss framework, the lower cross-braces are constructed from W-section steel profiles with a height of h = 100 mm, while the upper cross-braces utilize T-section profiles with a height of h = 75 mm. The lower and upper longitudinal beams are also T-section profiles, with heights of h = 75 mm and h = 100 mm, respectively, and widths of t_f = 7 mm and t_w = 14 mm. The cross sections shown in Figure 2 have axes 1 and 2 that help to orient them in the 3D geometric model.

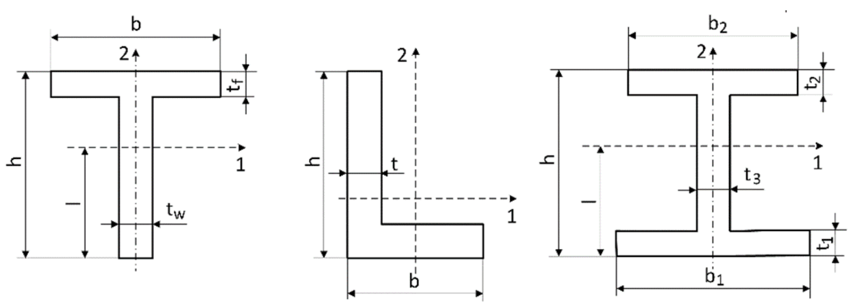

Figure 2
Cross sections of the members of the truss framework

The upper beams of the two portal frames, made from I-section structural steel, have a height of h = 200 mm, while the columns of the portal frames use stronger I-section beams with a characteristic height of h = 315 mm. The wind bracing trusses are formed from L 50 × 50 × 6 angle profiles. The truss columns have a more complex cross-section, consisting of multiple adjacent steel profiles. For analysis, these are approximated with an equivalent rectangular cross-section (h = 127.08 mm, b = 23.43 mm) exhibiting identical cross-sectional properties, as determined through simplified manual calculations.

Certain portions of the horizontal members include reinforcements from prior uses, but stiffeners were not modeled. Thus, these beams are assumed to possess uniform profiles in the three-dimensional structural model. Similarly, weather-related damage and corrosion of the structure were disregarded, as their effects were not considered significant factors influencing the mechanical properties of the structure.

This design can be used for open-pit mines where the distance between the banks of an open-pit mine is below 18–20 meters and the span of the bridge cannot be increased without significant modifications opposite the modular design. When a crane of sufficient capacity is available, the entire bridge structure together may be lifted on to take the right place.

The commercial solution is based on a Bailey bridge, which is a portable, prefabricated, modular truss bridge designed for quick assembly without heavy equipment. Figure 3 illustrates the conceptual design of a pre-assembled segment of the alternative modular bridge structure. The available in predefined manufacturer size increments of modular bridge and its components are picked from tables or catalogs tailored to list the various geometric properties, allowing the selection of mobile components with the required conveyor belt width. For a conveyor belt not exceeding a width of 3 meters, a suitable modular variant is also available, for example in Arcow 700XS technical handbook. Due to the conveyor belt width, the modular bridge element in Figure 3, which provides the roadway width and supports the conveyor platform, can be 3.67 meters in width according to the catalog. This available configuration allows sufficient space for an inspection walkway alongside the conveyor belt.

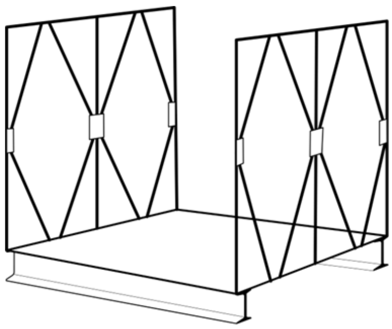

Figure 3
Design of assembled modular bridge elements

The modular bridge structure is assembled from prefabricated modules using detachable bolted connections or pins to mix and match the appropriate components creating the bridge. The bridge construction process can be assembled on site, where the bridge structure is built from one side by continuously adding and connecting pre-assembled modules, extending as a cantilever to reach the opposite support point. The standard truss configurations used for stiffening the bridge can be arranged in multiple rows alongside the bridge platform, thereby enhancing the load-bearing capacity.

3. COMPARISON OF STRUCTURES

The existing structure in Figure 1 meant for reuse is subjected without loading in the first load case (in load case A), i.e. without an installed conveyor belt system. In load case B, the loading is calculated based on the mass of the material transported on the conveyor belt, assuming a loose bulk density of $\rho_h = 1.4 \times 10^{-9}$ t/mm^3, as described in Ladányi (2018) and Ilic et al. (2017) with the specified material cross section. In load case B, based on Ladányi (2018), a continuous operational load is considered constant, accounting for the weight of the transported overburden rock, the conveyor belt, and associated framework elements, which is evenly distributed across the lower longitudinal beams. The load, calculated using the loose bulk density, is applied at the connection points of the lower cross-braces, distributed as downward forces of 15 kN at nine nodes on each side of the structure between the supports. The total load of 270 kN is represented by small downward vectors, as shown in Figure 4, indicated accordingly.

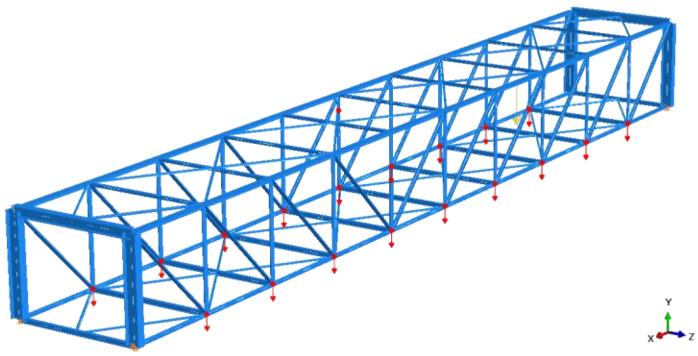

Figure 4
Distribution of loads and supports specified for welded bridge frames

The lateral planes of the conveyor belt intended for installation occupy nearly the entire width of the bridge framework, precluding the possibility of integrating a walkway within the truss structure for inspection purposes. One solution to ensure accessibility is to install a walkway on one side of the structure, supported by cantilever brackets. This configuration has proven effective in other operational mining equipment, such as bucket-wheel excavators, bucket-chain excavators, and spreaders. Due to the additional mass of the cantilever-mounted walkway on the truss structure, a slight increase in weight is introduced compared to load case B. This is addressed in calculation variant C by increasing the applied partial forces by 1.5 kN at the nine loading points on one side. Consequently, a uniformly distributed load of 148.5 kN acts on one side, while the other side retains a load of 135 kN.

Standard material properties for steel are assumed to be isotropic elastic, for which Young's modulus of $E = 2.1 \times 10^5$ MPa, Poisson's ratio of $\nu = 0.25$, and density of $\rho = 7.85 \times 10^{-9}$ t/mm^3 are given. Using finite element analysis, the dead weight of 6217 kg is obtained from the 3D beam structure and the specified density.

In the FEA using Abaqus 6.13, the boundary conditions for the first bridge structure were simplified supports at the four lower corner points to prevent rigid-body motion in space while avoiding over-constraint between any two support points. To achieve this, one support point was modeled as a spatial pinned support, constraining motion in all three directions, while the remaining three lower corner points were defined as spatial roller supports, allowing movement within their respective planes but restricting motion perpendicular to those planes. All specified supports permit rotational freedom about the three orthogonal axes.

The conveyor bridge is significantly reinforced at both ends by robust portal frames, which consist of considerably heavier I-beams compared to other elements. The calculations demonstrate that these portal frames substantially enhance the structure's robustness, both in terms of strength and vibrational properties.

In load case C, the asymmetric loading introduces torsional stress in addition to a slight increase in load magnitude on the three-dimensional structure. However, this does not result in significant changes in the strength analysis outcomes.

Modelling the static behavior of the structure is essential for the reusable welded framework. Since effective stresses in the main load-bearing elements occur below 89.86 MPa and the structure is made of grade S275 steel with a minimum yield strength of 275 MPa, the ratio, the actual safety factor for static loads in all three load cases (A, B, and C) exceeds $n = 3$. The maximum deflection at the midspan of the bridge is only 21.6 mm. The primary load-bearing members are the central sections of the lower longitudinal beams and the first cross-braces at the portal frames, as reported by Szirbik et al. (2023).

The loads acting on the conveyor belt during material transport can be determined through measurements or simulations based on the sag ratios of the bulk material and the belt, as described by Ilic et al. (2017). These allow for the calculation of the loads transmitted through the conveyor rollers to the framework due to material transport. The condition monitoring of conveyor rollers can also be achieved using acoustic sensors, as reported by Wijaya et al. (2022).

For simplicity, a 3D wireframe in Abaqus with beam elements was used for the modal analysis, neglecting damping to predict the natural frequencies and mode shapes of the structure. The natural frequencies are arranged in ascending order, summarized in Table 1 for load cases A, B, and C. If the suspended hanging roller sets are applied, the forces resulting from the loads are exerted in the vertical direction, uniformly distributed, at the midpoints of the piers, and considering an angle of the wing rolls of 30°, the perpendicular components also arise. The maximum value of the vertical displacement is 23.15 mm in the middle of the bridge; thus, the deflection ratio remains 0.01%. The results indicate that the structure is excitable at relatively low frequencies, a consequence of using slender members. Although the structure is subjected to loading, this has a minor impact on its vibrational behavior, as the primary load-bearing elements are the central sections of the lower longitudinal beams and the first cross-braces at the portal frames, as noted by Szirbik et al. (2024).

Table 1

Natural frequencies [Hz] for load cases A, B, and C

Modus No.	**Load cases**		
	A	**B**	**C**
1.	7.727	7.702	7.701
2.	9.285	9.285	9.284
3.	10.095	10.146	10.149
4.	14.480	14.477	14.476
5.	14.738	14.560	14.548
6.	16.004	15.405	15.361

It can be concluded that the applied loads do not significantly detune the structure, only slightly modifying the natural frequency values, as the preload in most structural members changes minimally. The linear perturbation performed on the FE model yields the natural frequencies, but the first few modes are dominant and are necessary for further analysis. Structural damage or deviations from the designed parameters can lead to changes in the natural frequencies, which may have unfavorable consequences.

The modular bridge's truss construction contains eight bays, resulting in a nominal span of 24.4 m, and can be substituted for the welded structure. Considering the roadway width of 3.67 m and the height of 1.74 m, the dead weight of the bridge is 16224 kg. Concluding that the selected modular design weighs more than the first welded version, which needs to be modified. The selected bridge designs can be reinforced by adding additional components. The modular bridge can be reinforced more easily with double-storey or two-panel tower constructions. The adequate load-bearing capacity and stability in the truss construction, associated with the conveyor belt system, can be ensured based on the technical specifications provided in the manufacturer's solutions published in the manufacturer's catalogs. The existing structure in Figure 1. meant for reuse can be damaged from the overloading and, etc. must be continuously monitored, which is why a sidewalk is also placed on the bridge on one side along the conveyor belt. Modular designs provide sufficient space for monitoring and are more resistant to vibrations caused by the movement of the conveyor belt than the welded truss structure.

4. CONCLUSIONS

A truss structure designed and built for the conveyor belt transporting lignite is reused for a new belt conveyor system, which applies a wider belt than the previously installed unit, and the total weight of the belt conveyor increases. The options included the reconstruction or use of a Bailey bridge-based commercial solution, which is a portable, prefabricated, modular truss bridge.

Finite element simulations on the three-dimensional wireframe model of the reusable bridge framework provide accurate insights into structural deformation and stress distributions, as well as the extraction of natural frequencies in the modal analysis. The FEA is essential for the preliminary verification of operational safety for the conveyor belt system installed on the truss bridge structure.

Finite element simulations for the existing structure have proved that the truss bridge is robust enough for the new conveyor belt and the material being transported is adequate based on the deflection and safety factor. Furthermore, the I-beam gates at the ends also strengthen the structure.

The conveyor belt system monitoring and the unexpected vibrations cause problems with the reuse of the truss structure. The investigation of vibrations induced by the conveyor belt motion and roller wear on the truss structure is unavoidable, as resonance must be prevented. The modal analysis provides the basis for investigations of excited vibrations to mitigate vibration-related issues in structures.

We have found that the weight of the optional modular design exceeds that of the existing welded structure, and bank abutments must also be constructed accordingly. But the advantages of the modular structure are also obvious, particularly in the combinatorial possibilities of the components, allowing the panel bridge to be reinforced with additional components if necessary, forming double-storey or two-panel tower constructions.

REFERENCES

Abaqus 6.13 Online Documentation; Dassault Systems, (2015). Available online: http://130.149.89.49:2080/v6.13/index.html

Acrow Bridge (2015). *Acrow Panel Bridging Technical Handbook. 700XS Modular Bridging System*. 4th ed., Acrow Corporation of America, Parsippany, USA.

Bathe, K. J. (1996) Finite Element Procedures; Prentice-Hall Inc.: Englewood Cliffs, NJ, USA.

Ilic, D., Wheeler, C. (2017). Measurement and simulation of the bulk solid load on a conveyor belt during transportation. *Powder Technology*, 307, pp 190–202.

Ladányi, G. (2018). Strength assessment of a truss bridge for belt conveyors, Annals of the University of Petroşani. *Mechanical Engineering*, 19, pp. 91–96.

Popescu, F. D., Radu, S. M., Andras, A., Brînas, I., Marita M. O., Rebedea, N. I. (2020). The modal analysis, using simulation and modelling, of the boom of the ERC-1400 Bucket Wheel Excavator during operation. *Applied Mathematics, Mechanics, and Engineering*, 63 (4), pp. 353–362.

Szirbik, S., Virág, Z. (2023). Finite element analysis of a steel bridge frame for belt conveyors. *Geosciences and Engineering: a Publication of the University of Miskolc*, 11 (1), pp. 114–119.

Szirbik, S., Virág, Z. (2024). Modal analysis of a bridge frame for belt conveyors. *Annals of the University of Petroşani, Mechanical Engineering*, 25, pp. 259–264.

Wijaya, H., Rajeev, P., Gad, E., Vivekanantham, R. (2022). Automatic fault detection system for mining conveyor using distributed acoustic sensor. *Measurement*, 187, 110330.

Geosciences and Engineering, Vol. 13, No. 2 (2025), pp. 104–124.
https://doi.org/10.33030/geosciences.2025.02.008

HEAVY MINERAL SAND FROM THE VICINITY OF TIBOLDDARÓC, BÜKKALJA REGION, NE HUNGARY

CSILLA BALASSA[1, *], NORBERT NÉMETH[2], FERENC KRISTÁLY[3], FERENC MÓRICZ[4], DÉLIA BULÁTKÓ-DEBUS[5]
[1, 2, 3, 4, 5]*Institute of Exploration Geosciences, University of Miskolc*
[1, *]csilla.balassa@uni-miskolc.hu
[2]norbert.nemeth1@uni-miskolc.hu
[3]ferenc.kristaly@uni-miskolc.hu
[4]ferenc.moricz@uni-miskolc.hu
[5]delia.bulatko-debus@uni-miskolc.hu
[1]https://orcid.org/0000-0001-6134-5262
[2]https://orcid.org/0000-0002-4264-5136
[3]https://orcid.org/0000-0002-0075-5994
[4]https://orcid.org/0000-0001-6708-3507

Abstract: Recent placer deposits of ilmenite-rich heavy sand were found in the Bükkalja region, in the vicinity of Tibolddaróc, sampled in a stream bed and in a rill on a dirt road. These placers consist mostly of plagioclase feldspars, quartz and ilmenite. In this paper, the composition of the sampled placer is studied, as well as the composition of some neighboring Miocene ignimbrite and tuff samples, potential source rocks of heavy minerals. The amount of ilmenite can reach 20-30 wt% in the bulk sample, but it is almost 50 wt% in the 0.212–0.3 mm grain size fraction. With simple magnetic separation, this enrichment can be increased to 70 wt%. In addition to ilmenite, heavy sand contains a relatively high amount of allanite and zircon as well.

Keywords: *Ilmenite, allanite, placer deposit, ignimbrite, tuff, Bükkalja*

1. INTRODUCTION

The ilmenite is a usual accessory both in igneous and metamorphic rocks and a common constituent of placer deposits, due to its high specific gravity (4.72). In addition to rutile, it is the main source of Ti, whose metallic form is a critical element in the European Union (Bowles et al., 2011). Most of the ilmenite is mined from placer deposits, but there are also hard rock deposits (ultramafic to mafic layered intrusions or anorthosite massifs) (Murphy and Frick, 2006). The most significant ilmenite placer deposits are marine, situated in coastal areas, like in India, Bangladesh, Brazil, Australia, New Zealand, South Africa, Egypt (Angusamy et al., 2005; MacDonald and Rozendaal, 1995; Nayak et al., 2012; Prates Hallal et al., 2025; Rahman et al., 2020; Ramakrishnan et al., 1997; Roy, 1999; Wassef, 1981; Wells and Haverkamp, 2020), but for example in Virginia alluvial deposits occur (Herz et al., 1970). Less significant ilmenite placer deposits are situated even in European countries, such as Ukraine and in Greenland (eluvial, alluvial and marine placers as well) (Ganzha et al., 2023; Kolb et al., 2016). Non-formula element content in ilmenite is often a useful indicator of the provenance area, especially the Mn/Mg ratio and the Ni, Cr, V, Co concentration (Bhattacharyya et al., 1997). The Ti/(Ti + Fe) ratio in ilmenites refers to the degree of alteration, due to Fe removal from the structure in the presence of water, in acidic environment. Leached ilmenite then alters to pseudorutile, finally to leucoxene (Mücke and Bhadra Chaudhuri, 1991).

Ilmenite is known as a common accessory mineral in certain Miocene volcanic rocks of the Bükkalja region (e. g. Czuppon et al., 2012; Harangi et al., 2005; Lukács et al., 2022). Small-scale ilmenite-rich placers were found in the region, near Tibolddaróc, as a proximal weathering product of the volcanic formations redeposited by runoffs. In addition to ilmenite, the sands have a small enrichment of allanite and zircon as well. Although the extension of these recent heavy mineral accumulations detectable on the surface is far smaller than the economic placers, probably it is the indication of bigger alluvial deposits in the sole of the valleys. This study introduces the composition of a sampled deposit in the stream bed of the temporary runoff Száraz-tó-ér, with a comparison of the heavy mineral content of the potential source rock types and a local recent natural concentrate. The current state of research does not aim to investigate the extent and economic significance of a potential resource, only to indicate its existence.

2. GEOLOGICAL SETTING

The Bükkalja region is an extensive outcrop area of Miocene volcanics in NE Hungary. The magmatism responsible for its generation was the result of the subduction of Vardar / Magura microplate under the ALCAPA microplate, which also carried volatiles (Kovács and Szabó, 2008). Due to the rotation of the microplates, lithospheric thinning occurred (Csontos et al., 1992). The Bükkalja region is characterized by silicic ignimbrite units, supplemented with fall-out deposits and paleosols (Biró et al., 2020). Originally, three silicic horizons were identified with various tools, including K-Ar geochronology and paleomagnetic studies: the Lower, the Middle, and Upper Rhyolitic Tuff Complexes (Szakács et al., 1998). Newer, mainly zircon trace element chemistry and U/Pb dating-based studies indicate eight eruption phases (Lukács et al., 2018), based on which the Miocene volcanic sequence was divided into four lapilli tuff formations, namely Tihamér Rhyolite Lapilli Tuff (18.2–17.1 Ma), Bogács Dacite Lapilli Tuff (16.8–16.2 Ma), Tar Dacite Lapilli Tuff (15.1–14.8 Ma) and Harsány Rhyolite Lapilli Tuff (14.7–14.4 Ma) Formations (Lukács et al., 2022). In another division, Hencz et al. (2024) identified a single formation with eleven lithological members and fourteen eruption events, mainly based on lithostratigraphic and geochemical signatures. Although the general composition of the rocks is silicic, in the case of the Bogács Tuff Formation primitive basic melts also had a role in the volcanism (Czuppon et al., 2012).

3. Materials and methods

3.1. Sample preparation and analytical methods

Collected rock samples were first crushed in a steel mortar up to 1 mm, then pulverized in porcelain and agate mortar up to 65 and 5 μm, respectively. Before grinding, ilmenite sand samples were first homogenized and rinsed with distilled water to remove the clay fraction. After that, the remaining heavy mineral fraction was dried and sieved with the following mesh sizes: 2 mm, 1 mm, 500 μm, 300 μm, 212 μm and 106 μm. From an ilmenite-rich fraction, the ilmenite was further enriched with a magnet. From the sample, TD-5K clay and heavy mineral separation was made with the application of gravitational settling in distilled water.

Thin sections and polished sections were embedded into two-component resin (Araldit, 2020), and after three days drying, they were polished with silicium carbide abrasive powder and paper. Thin sections were stuck on glass plates, and thinned to 30 μm, while polished sections were also polished with diamond-bearing abrasive gel. For chemical analyses of the samples, the 65 μm powder was used. Analyses were done by wavelength-dispersive X-ray fluorescence spectrometry (WD-XRF), with a Rigaku Supermini 200 WDXRF instrument (200W Pd X-ray tube, 50 kV accelerating voltage, 4 mA current, LiF200 / PET / XR25 crystals, 4 g pellets with CEREOX) to determine the concentration of major and minor elements, as well as some trace elements (e.g. Zr). Trace element concentrations of five samples (four ignimbrite and a tuff) were analyzed by the laboratory of ALS with ICP-MS (ME-MS81 analyses, based on Li-borate digestion and four acid dissolution), on the same powder, then XRF.

The mineralogical composition was determined by X-ray powder diffraction (XRD) on the 5 μm powders. For the measurement, a Bruker D8 Advance (40 kV, 40 mA Cu K-α radiation) instrument was used with a Vantec-1 position-sensitive detector, in parallel beam geometry using a Göbel mirror. The phase identification was carried out using DiffracPlus EVA software, based on the ICDD PDF2 2005 database, while the quantitative evaluation in Topas4 software with Rietveld refinement method [NIST SRM 640b Si calibration standard, crystal structure information from AMCSD (Downs and Hall-Wallace, 2003)].

Electron microprobe studies on the carbon-coated polished slabs were used to measure the chemical composition of individual grains (energy dispersive X-ray spectrometry, EDX point measurements and X-ray element maps) and to observe the distribution of the different minerals on back-scattered electron (BSE) images. For the electron microprobe studies, a SamX-controlled JEOL JXA 8600 Superprobe was used (20 kV accelerator voltage, 20 nA beam current), equipped with an SDD-EDX detector.

Textural characteristics and mineralogy were investigated also by optical microscopy on the thin sections in transmitted light (Zeiss Imager A2m AXIO polarization microscope, Zeiss AxioCam MRc5 camera). The flowchart of the research process is shown in Figure 1.

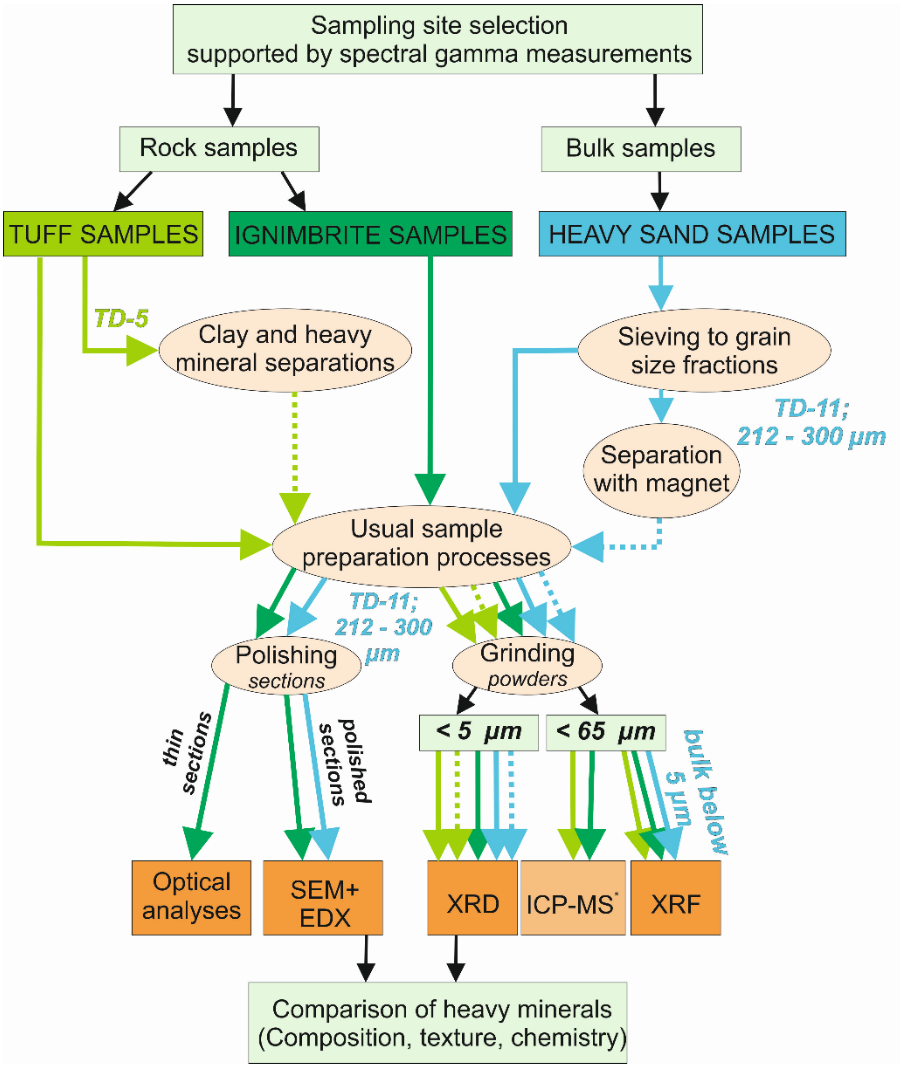

Figure 1

Flowchart of the research process

*(Analytical methods, except ICP-MS were performed
in the Institute of Exploration Geosciences, University of Miskolc)

3.2. Samples and sampling methods

Sampling was supported by natural gamma measurement (Gamma Surveyor portable scintillation detector). Sites of sampling and spectral gamma measurements are shown in Figure 2. Integral measurements indicate relatively homogenous gamma activity within the investigated area but higher activity over the sampled placer. At certain points, including sampled exposures spectral gamma analysis was performed. The K values in the territory are usually between 2–5 wt%, the equivalent

Th (eTh) values 15–20 ppm, while the maximum value of the equivalent U (eU) is around 8 ppm (Table 1). The stream bed with the heavy mineral accumulation stands out by high eTh value. Samples TD-2 and TD-3 are massive ignimbrites from the Bér-oldal quarry, from the vicinity of Tibolddaróc. (From measuring point TD-K-1 no sample was collected.) Both samples are welded and have a fiamme-bearing structure, but while the matrix of TD-2 is yellowish, TD-3 is pinkish. Sample TD-4 is taken from a nearby gully. It is very similar to the other two samples, as it is also a fiamme-bearing ignimbrite of brownish color. Samples TD-5A, 5K and 5F are pumice-rich lapilli tuff samples representing the lower (A), middle (K) and upper (F) bed groups of a ravine wall of the Száraz-tó-ér stream. The material is relatively loose, the most compact is the middle part. Sample TD-7 is a pumice-rich tuff, collected near Kőhodály, a historical artificial sheepfold carved into the cliff. Sample TD-10 is ilmenite-rich heavy sand collected from the depression of a dirt road. Sample TD-9 is a grey ignimbrite collected from debris in the vicinity of the TD-10. In the case of TD-9 and TD-10 spectral gamma data were not recorded, because the small volume of the sampled material is suppressed by the effect of the background. Sample TD-11 is heavy sand, from the bed of the Száraz-tó-ér stream. This sample showed the highest eTh-content in the area with 30 ppm eTh. A more in-depth test series would be required to determine the stratigraphic position with complete certainty, but the observed textural, chemical and mineralogical features and topographic situation of the outcrops suggest in case of most of the samples that the most likely candidate is the Bogács Dacite Lapilli Tuff Formation. This formation is increasingly mafic from bottom to top. The sampled tuffs probably belong to the Harsány Lapilli Tuff Formation, which was also described from the vicinity of Tibolddaróc. These two formations were described to contain zircon, apatite, ilmenite and allanite as accessories (Babinszki et al., 2024; Lukács et al., 2022).

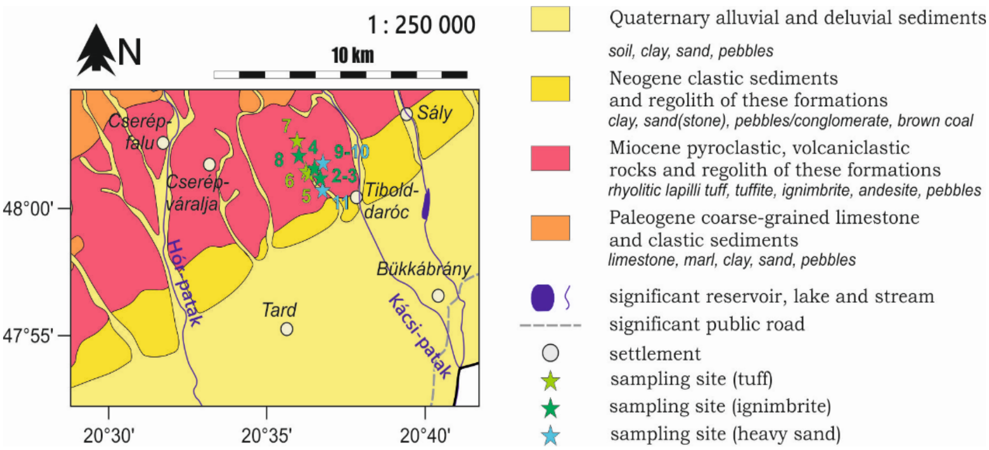

Figure 2

Schematic geological map of the surroundings of Tibolddaróc by marking the sampling sites with their number

Table 1
Location of the sampling sites and results of the spectral gamma ray measurements in the vicinity of Tibolddaróc

	EOV Y	EOV X	K [wt %]	eU [ppm]	eTh [ppm]	Dose rate[nGy/h]	comment
TD-1	767065	288400	3.93	3.4	19.45	119.55	Welded ignimbrite, quarry *(samples TD-2 and TD-3)*
TD-2	767035	288420	3.60	5.5	19.3	126.7	
TD-3			3.52	3.15	17.65	108.5	
TD-4	766835	288755	3.50	4.05	19.5	117.85	Welded ignimbrite, gully *(sample TD-4)*
TD-5A	766615	288545	4.87	5.5	19.35	143.35	Lapilli tuff, ravine *(samples TD-5A, TD-5K, TD-5F)*
TD-5K	766615	288545	4.01	7.9	19.65	146.6	
TD-5F	766615	288545	4.58	4.8	19.9	137.15	
TD-5b	766615	288545	3.68	5.9	19.9	131.65	
TD-6	766500	288650	4.25	6.45	18.35	138.35	Bomb-rich lapilli tuff, ravine *(no sample)*
TD-7	766145	289765	3.89	5.7	15.8	123.2	Lapilli tuff (Kőhodály) *(sample TD-7)*
TD-8	766220	289220	2.96	4.45	15.05	102.1	Welded ignimbrite *(no sample)*
TD-9	767170	288955	Gamma spectrum not measured				Welded ignimbrite *(sample TD-9)*
TD-10							Heavy sand *(sample TD-10)*
TD-11	767155	287960	2.19	5.15	29.6	131.9	Heavy sand in stream bed *(sample TD-11)*

3.3. Grain size distribution of heavy sand samples

Heavy sand samples were sieved into grain size fractions before any other sample preparation processes were made. The total weights of the samples before the sieving were about 150 g and 175 g, in the case of samples TD-10 and TD-11, respectively. As the fractions above 2 mm are partly composed of artificial material (brick and glass fragments) and lithoclasts, they were ignored during further analyses. Total sample weights excluding this fraction were 131 and 102 g, respectively. The grain size distributions are smooth enough in the case of both samples, but not the same (Figure 3). The dominant size fractions in sample TD-10 are the 212–300 μm and 300–500 μm, while in the case of sample TD-11 the 300–500 μm and 500 μm–1 mm fractions. The 0–106 μm fraction is insignificant in both samples (1.6 and 0.65 wt%).

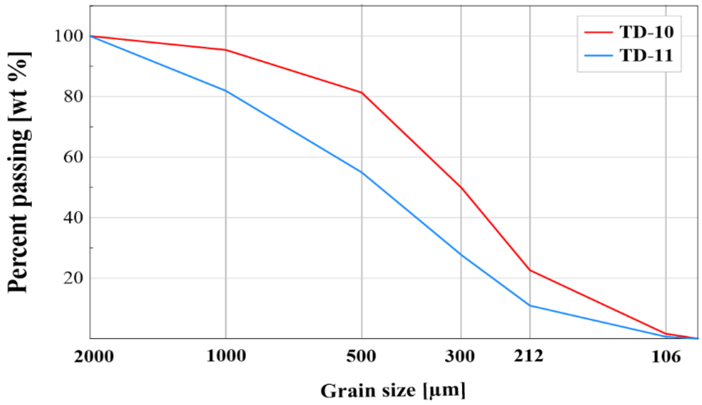

Figure 3

Grain-size distribution of samples TD-10 and TD-11

4. Results

4.1. Chemical composition

Major, minor and trace element concentrations of the studied samples measured by XRF are summarized in Tables 2 and 3. Major element concentrations of the ignimbrite and tuff samples are similar: about 70 wt% SiO_2, 14 wt% Al_2O_3, 0,5–0,6 MgO, 1–3 wt% CaO and Na_2O, 3–5 wt% K_2O and 2–3 wt% Fe_2O_3. This composition corresponds to the rhyolitic – dacitic fields in the TAS diagram (Figure 4a). The exception is sample TD-9, with its lower SiO_2 and K_2O and higher CaO and Fe_2O_3 concentrations (basaltic andesite composition). The REE+Y content of the samples studied (TD-2, TD-3, TD-9, TD-7) is between 180 and 310 ppm (Table 4) light REEs are more enriched than heavy ones. Negative Eu anomaly is characteristic. Zr concentration is between 180–300 ppm, Th between 9–19 ppm, Nb 11–14 ppm, TiO_2 0.1–1 %. The Zr and TiO_2 contents are generally higher in the ignimbrite samples examined than in tuff samples, but for other HFSEs the data is insufficient to establish such relationships. Trace element concentrations also indicate rhyolitic-dacitic composition in the Winchester-Floyd diagram (Figure 4b), except in the case of sample TD-9. The upper crust normalized (Rudnick and Gao, 2013) trace element plot and chondrite normalized (Anders and Grevesse, 1989) REE plots are shown in Figure 5. It is important to highlight that all indicated concentration data refer to the whole rock compositions, not for volcanic glass.

Table 2

Major and minor element concentrations of the analyzed samples based on XRF measurement

Sample	SiO_2	Al_2O_3	MgO	CaO	Na_2O	K_2O	Fe_2O_3	MnO	TiO_2	P_2O_5	S	TOTAL
	%											
TD-7	72.4	13.7	0.61	2.16	1.89	3.87	2.14	0.036	0.276	0.045	0.01	97.1
TD-2	67.7	14.1	0.63	2.32	2.82	3.31	2.91	0.020	0.406	0.068	0.01	94.3
TD-3	68.8	14.1	0.66	2.41	2.74	3.35	3.00	0.040	0.321	0.055	0.01	95.6
TD-4	66.1	14.2	0.54	2.94	2.80	3.22	3.60	0.023	0.427	0.082	0.02	94.0
TD-5 A	73.1	13.0	0.52	1.03	1.10	4.52	2.07	0.058	0.236	0.010	0.02	95.7
TD-5 F	73.3	13.1	0.51	0.98	1.06	4.35	1.91	0.053	0.216	0.009	0.01	95.5
TD-5 K	69.9	13.8	0.93	1.15	0.85	3.90	3.03	0.076	0.267	0.013	0.02	94.0
TD-9	56.8	16.5	1.63	5.41	1.83	1.73	7.33	0.073	1.091	0.175	0.01	92.5
TD-10*	26.3	5.5	1.74	1.98	0.94	0.63	23.7	0.319	**32**	0.171	0.02	93.3
TD-11*	27.5	5.6	1.25	1.65	0.96	0.69	20.5	0.305	**36**	0.095	0.02	94.5

*bulk sample below 300 µm

Table 3

Trace element concentrations of the analyzed samples based on XRF measurement. F and As are always below detection limit (<0.3 and <10 ppm, respectively)

Sample	Cu	Zn	Pb	Rb	Sr	Ba	Cr	Co	Ni	Zr
	ppm									
TD-7	22	59	21	169	306	1080	23	<10	20	172
TD-2	20	53	17	126	222	932	25	<10	17	254
TD-3	20	56	19	154	230	998	25	<10	18	230
TD-4	13	54	19	130	247	1017	25	<10	17	299
TD-5 A	17	175	30	283	136	1218	17	<10	21	164
TD-5 F	20	61	24	283	127	1151	18	<10	18	161
TD-5 K	19	68	18	254	134	1106	19	<10	24	168
TD-9	23	77	45	57	264	521	65	16	22	226
TD-10*	<10	108	<10	<10	39	1893	294	39	25	417
TD-11*	<10	80	<10	<10	36	2072	204	36	21	437

*bulk sample below 300 µm

Table 4

Concentration values of some selected trace elements, based on ICP-MS

Sample	Ba	Cr	Nb	Rb	Sn	Sr	Ta	Th	U	V	∑REE+Y
TD-3	1030	20	13.6	119	3	223	1.6	18.05	4	45	279.34
TD-2	909	21	13.6	108	2.5	190.5	1.1	19.25	3.48	51	312.97
TD-4	995	18	13.45	115	2.7	219	1.1	17.15	3.8	44	272.64
TD-9	505	71	14.2	60.2	18.3	292	1	8.76	2.31	196	183.56
TD-7	1070	13	11.25	141.5	3.6	250	1	17.6	4.34	29	182.35

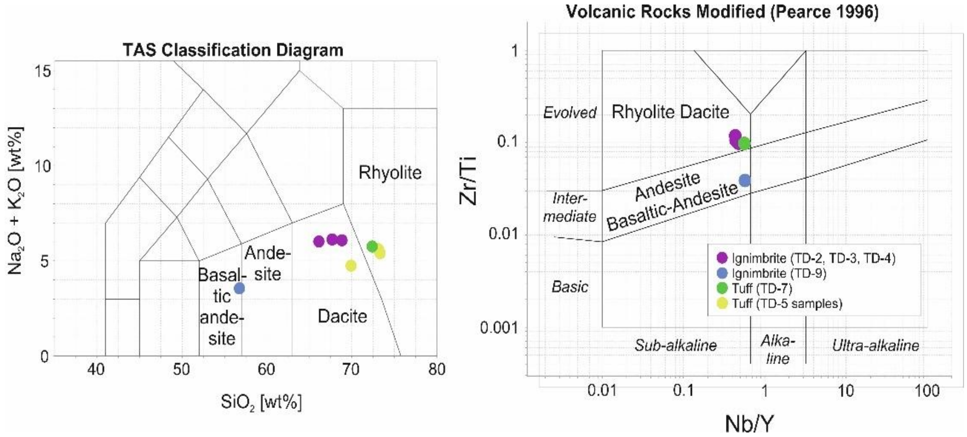

(a) (b)

Figure 4

Rock classification plots for the studied samples. (a) TAS diagram, (b) Winchester-Floyd diagram

From samples TD-10 and TD-11 XRF analyses were performed only on the <300 μm fractions. Based on it, about 35-40 wt% of the samples are composed of TiO_2, with approximately 20 wt% Fe_2O_3, 30 wt% SiO_2 and 5 wt% Al_2O_3. MnO (~0,1 wt%) and Cr (60-70 ppm) are also enriched in these samples, compared to the upper crust. TiO_2 values in TD-10 and TD-11 are not reliable, as the XRF instrument is not calibrated to such high values. Most of the trace elements have not been measured yet.

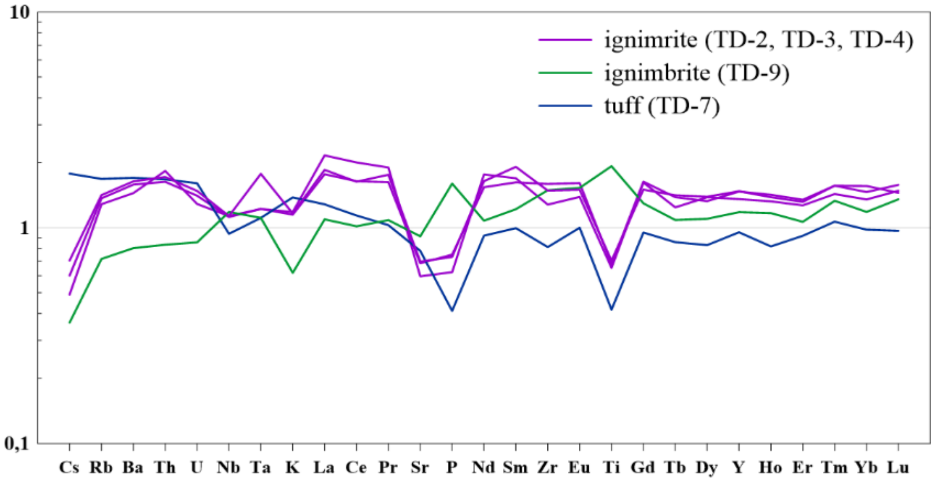

(a)

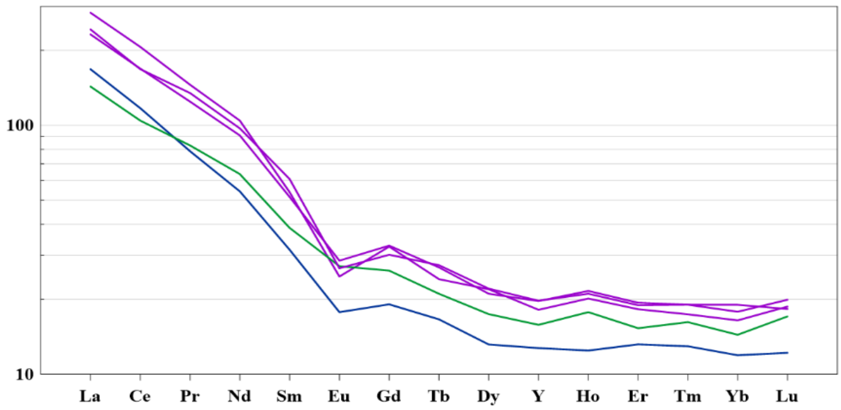

(b)

Figure 5

Upper crust normalized trace element (a) and chondrite normalized REE concentrations(b) of some selected samples

4.2. XRD analysis of the heavy sand samples

All six sample fractions were separately pulverized for XRD analyses for both samples. Mineral constituents are the same in every fraction (ilmenite, hematite, zircon, allanite, apatite, quartz, cristobalite, plagioclase feldspars, sanidine, pyroxenes), but their ratios vary (Table 5).

Table 5

Mineralogical composition of each fraction of the heavy mineral sand samples (in wt%, based on XRD; nd: not detected)

	TD-10						**TD-11**					
upper mesh size [µm]	**2000**	**1000**	**500**	**300**	**212**	**106**	**2000**	**1000**	**500**	**300**	**212**	**106**
Quartz	25.37	28.07	9.95	5.90	7.04	15.84	28.08	33.88	14.80	9.02	11.87	24.21
Cristo-balite low	13.04	8.18	2.06	1.43	1.08	0.70	11.27	5.94	1.82	1.52	1.27	0.53
Anorthite	1.89	1.08	1.00	0.95	1.80	1.64	1.08	0.83	0.81	0.63	1.18	0.64
Andesine	5.50	1.85	0.23	0.11	0.17	13.13	6.36	6.79	0.55	0.35	1.32	7.29
Oligo-clase	14.01	10.74	2.30	1.91	1.82	4.50	15.95	10.14	1.78	1.36	2.12	5.83
Labra-dorite	0.90	11.46	18.54	15.26	17.45	5.20	1.98	8.00	17.75	16.42	19.01	4.60
Sanidine	17.93	11.39	3.16	2.33	0.61	2.18	14.75	8.48	3.55	1.73	2.31	1.53
Biotite 1M	0.39	0.63	0.13	0.48	0.00	0.00	0.50	0.70	0.07	0.06	0.00	0.00
Enstatite	1.12	5.64	10.05	10.22	7.55	5.51	0.84	8.68	11.39	5.37	3.53	5.02
Augite	0.14	0.48	1.74	1.36	1.37	0.77	0.12	0.42	1.37	1.20	0.48	1.54
Ilmenite-(Mg)	0.17	8.78	30.50	37.86	35.45	23.17	0.05	3.37	29.76	45.10	39.71	25.35

	TD-10						TD-11					
upper mesh size [µm]	**2000**	**1000**	**500**	**300**	**212**	**106**	**2000**	**1000**	**500**	**300**	**212**	**106**
Rutile	0.01	0.01	2.11	2.96	3.26	nd	nd	nd	1.27	2.32	2.27	nd
Hematite	1.03	2.08	4.63	6.62	6.40	5.72	0.29	0.42	2.11	4.36	3.65	3.37
Magnetite	1.03	1.00	3.09	3.61	3.99	0.09	0.40	0.36	0.57	0.27	0.52	0.09
Allanite-(Ce)	1.75	1.03	1.79	1.37	1.44	3.13	2.06	1.05	0.87	0.99	0.85	0.72
Zircon	0.69	0.70	0.53	0.37	0.47	3.66	0.80	0.45	0.46	0.69	0.59	3.88
Amor-phous	15.04	6.88	8.19	7.26	10.10	14.86	15.46	10.50	11.07	8.61	9.31	15.50

Mineral composition of the complete samples below 1 mm was not measured but calculated using the weights and the mineral compositions of the individual fractions. Based on that, the total ilmenite content in the samples (excluding materials over 2 mm) is around 30 wt% (sample TD 10) and 20 wt% (sample TD 11), with significant feldspar (almost 30 wt%) and quartz (10–20 wt%) content Based on the XRD results, the most characteristic plagioclase feldspar is the labradorite in both samples. As for the individual factions, the highest ilmenite concentration is present in the 106–212 µm fraction and 212–300 µm fractions (35–45 wt%), but generally the concentration of the ilmenite is above 20 wt% in every fraction below 500 µm. Compared to these fractions, the ones above 500 mm are relatively poor in ilmenite, but they have a high ratio of quartz, cristobalite and feldspars. Zircon is usually low, but it can reach almost 4 wt% in the finest fractions of the samples.

Based on the concentration data and the grain size distribution, we could calculate the distribution of the various minerals within different fractions (assuming that the total amount of each mineral is 100%). About 30–40 wt% of the ilmenite is in the fractions 212–300 µm and 300–500 µm, while 20–25 in the 0.106–0.212 fractions (Figure 6).

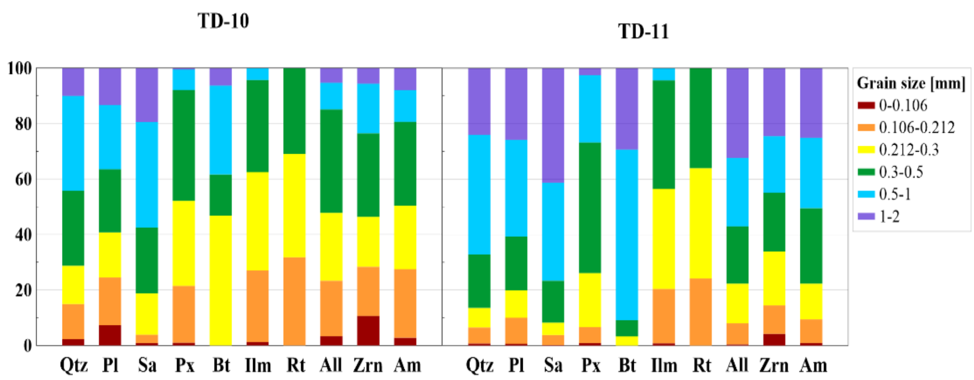

Figure 6

Distribution of some minerals between the different grain size fractions in the heavy sand samples (Qtz = quartz, Pl = plagioclase, Sa = sanidine, Px = pyroxene, Bt = biotite, Ilm = ilmenite, Rt = rutile, All = allanite, Zrn = zircon, Am = amorphous)

The 212–300 µm fraction of sample TD-11 was further separated with a magnet. In the magnetic subfraction the ratio of the ilmenite reached almost 70 wt%. Hematite, rutile, magnetite, and pyroxene, as well as allanite are also enriched in this fraction. The non-magnetic fraction is dominated by feldspars and quartz. Figure 7 compares the XRD diffractograms of the magnetic and non-magnetic fractions, while Table 6 summarizes the mineral quantities.

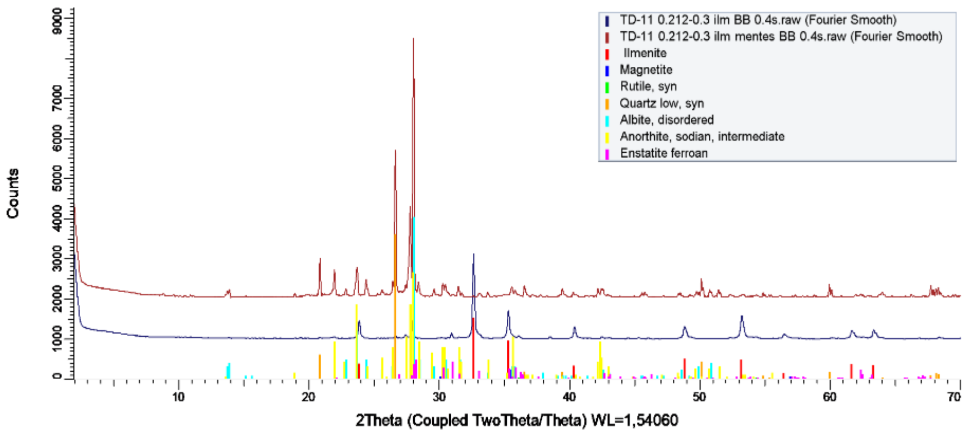

Figure 7

XRD diffractograms of the non-magnetic (red line) and magnetic (dark blue line) fractions of sample TD-11 (grain size between 212 and 300 µm)

Table 6

Mineral composition of the magnetic and non-magnetic fraction of sample TD-11 (grain size between 212 and 300 µm), based on XRD analyses (amorphous is neglected)

	magnetic fraction [wt%]	non-magnetic fraction (wt%)
Quartz	1.69	25.55
Cristobalite low	1.59	2.04
Plagioclase	2.22	58.09
Sanidine Na0.1		6.57
Enstatite	8.76	2.93
Augite Px	4.40	1.02
Ilmenite (Mg)	66.38	
Rutile	3.40	
Hematite	6.81	1.17
Magnetite	1.45	
Allanite-(Ce)	3.18	1.96
Zircon	0.13	0.68

4.3. XRD analysis of rock samples

The rock samples collected from the lapilli tuff and ignimbrite contain mostly the same rock-forming minerals and accessories. Main components are cristobalite, plagioclase feldspars and sanidine, as well as pyroxenes (Table 7). There is no significant difference between samples TD-2, TD-3 and TD-4. Quartz content is near zero, and most of the SiO_2 can be identified as cristobalite (5–13 wt%), which is a usual product from the alteration of volcanic glass (Schipper et al., 2020). Plagioclase feldspars constitute about 30 wt%, supplemented with 20% sanidine, pyroxene content is 4–9 wt%. Biotite (1.3–1.7 wt%), as well as smectite (0.6–3 wt%) usually occur in low concentrations. TD-9 is also similar but with lower cristobalite and higher smectite concentration. The amorphous composites of the samples take around 20-40 wt%.

Samples TD-5A, 5K and 5F have high smectite content with a low amount of halloysite and pyrophyllite. The middle part of the section (5K) has the lowest smectite content. Their feldspar association is dominated by plagioclase with a lower amount of sanidine. They do not contain pyroxenes but are extremely rich in amorphous material (almost 80 wt%). Similarly, sample TD-7 lacks pyroxenes, but it also lacks smectites. It does not contain sanidine, but microcline and orthoclase instead.

From TD-5K a gravitational separation experiment was made. The amorphous material is enriched in the coarser fractions, while smectite, halloysite, pyrophyllite, potash feldspars and hematite are in the clay fraction. No ilmenite, zircon or allanite enrichment can be detected in any of the fractions.

Table 7

Mineral composition of the examined samples, based on XRD analysis (in wt%)

	TD-5A	TD-5F	TD-5K	**TD-7**	**TD-2**	**TD-3**	**TD-4**	**TD-9**
Quartz	3.01	2.98	3.48	5.85	0.17	0.89	0.19	0.03
Cristobalite low	2.07	1.38	3.62	1.19	13.07	6.57	10.55	3.37
Anorthite	*1.91*	*2.22*	*2.12*	*0.50*	*2.65*	*3.11*	*1.29*	*2.05*
Labradorite An65	*0.06*	*0.04*	*3.64*	*9.69*	*17.65*	*9.91*	*9.22*	*18.30*
Oligoclase An25	*0.85*	*1.10*	*0.00*	*4.86*	*3.72*	*12.37*	*21.47*	*8.48*
Albite	*3.10*	*2.57*	*1.85*	*0.40*	*5.15*	*0.69*	*4.46*	*3.50*
∑ Plagioclase	**5.93**	**5.93**	**7.61**	**15.44**	**29.17**	**26.08**	**36.46**	**32.32**
Orthoclase				1.55				
Sanidine	3.11	2.86	4.34		19.48	17.39	19.38	20.43
Microcline intermediate				0.69				
Biotite 1M	0.31	0.00	0.28	2.72	1.73	1.33	1.52	0.62
Smectite 15A	5.52	6.50	1.21		2.98	0.65	0.61	5.29
Halloysite 7A	0.04	1.33	0.04					
Pyrophyllite 2M	1.17	1.10	1.68					
Augite				*0.21*	*6.35*	*1.76*	*4.50*	*4.24*
Enstatite				*0.56*	*2.55*	*1.98*	*2.13*	*5.80*

	TD-5A	TD-5F	TD-5K	**TD-7**	**TD-2**	**TD-3**	**TD-4**	**TD-9**
∑ Pyroxene				**0.77**	**8.90**	**3.74**	**6.63**	**10.04**
Ilmenite (Mg)	0.02	0.02	0.03	0.00	0.00	0.00	0.01	0.02
Hematite	0.26	0.53	0.36	0.02	0.03	0.60	0.15	1.48
Zircon				0.03	0.25	0.07	0.31	0.22
Allanite-(Ce)				0.16	0.65	0.01	0.27	0.02
Amorphous	78.56	77.38	77.35	71.57	23.56	42.67	23.93	26.17

4.4. EDX analysis of heavy sand sample

EDX analyses were performed on the 212–300 μm fraction of sample TD-11. EDX confirmed that a significant ratio of this fraction consists of ilmenite (Figure 8). The ilmenite grains are generally euhedral to subhedral, angular, or only slightly rounded. Ilmenite contains rare inclusions (apatite, volcanic glass) and intergrowths with other minerals (apatite, feldspars). Chemically it always contains Mg and Mn. The Mn/Mg ratio varies between 0.1 and 0.3, with an outlier value of 0.8. Occasionally V content can also be detected. The Ti/(Ti+Fe) ratio of the ilmenite crystals in atomic percent is generally close to 0.5, meaning that these ilmenites are chemically unaltered. Ilmenite also occurs in the lamellae of a spinel-type Fe- or Fe-Ti-oxide mineral (Ti-bearing magnetite or ulvöspinel). In the opinion of Lattard (1995), in the case of terrestrial rocks, this spinel-ilmenite intergrown texture is most often the result of oxidation processes, which might connect to the reduction of another subsystem of the same rock. Feldspar minerals are also angular. Measured composition of a few randomly chosen grains corresponds to sanidine, albite, and oligoclase. Subhedral, or slightly rounded allanite-(La) crystals are usual, with about 3 atomic % REE-concentration.

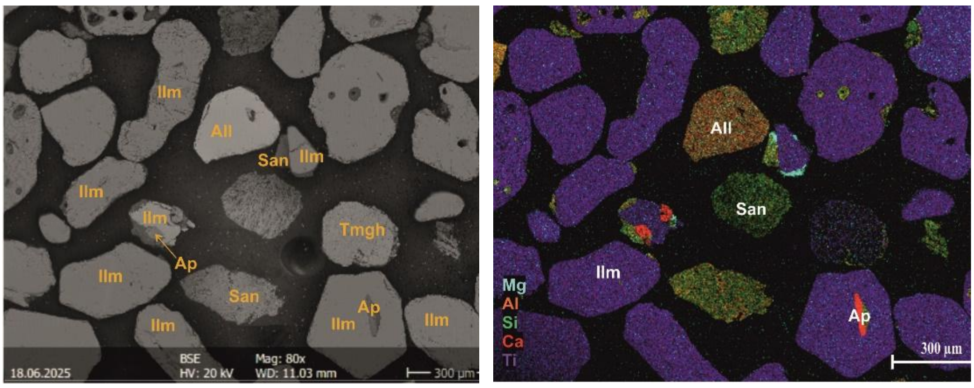

(a) (b)

Figure 8

BSE image (a) and element map (b) of the heavy sand sample, showing the abundant ilmenite grains, with some other characteristic minerals. (All = allanite, Ap = apatite, Ilm = ilmenite, San = sanidine, Tmgh = titanomaghemite?)

4.5. EDX and optical microscopic analysis of ignimbrite samples

Welded ignimbrite samples from the Tibolddaróc quarry and from the neighborhood have fluidal-vitrophyric texture (Figure 9 a–b). The main phenocrysts are sanidine and plagioclase feldspars which are most often euhedral-subhedral, elongated or stocky tables. Oscillation zoning as well as twinning are usual. They can be weathered and fractured. EDX suggests the composition of sanidine, oligoclase, andesine and labradorite. Cristobalite crystals are usually isometric. Biotite is common (except in sample TD-9). They occur as elongated or stocky plates up to several 100 of μm and can be deformed. In most cases, biotite is Fe-dominant and has Ti (1–1.4 atomic %), Mn (~0.1 atomic %), V (up to 0.1 atomic %) and Cl (0.1–0.3 atomic %) content. In samples TD-4 and TD-2 fiammes are dominated by fibrous, radial clay minerals, but smectite is an ordinary rock-forming mineral in all the other samples. Smectite is Fe-dominant. In sample TD-9 two special compositions can be distinguished: the first one is richer in Mg, Fe and Si, and associated with pyroxene, while the second is Si-rich, and associated with feldspars (Figure 9 c). The composition of smectite from the Tibolddaróc quarry is more homogenous, and intermediate between these two compositions. Pyroxene is especially characteristic of sample TD-9, with a composition corresponding to enstatite. Important accessories in all samples are apatite, zircon, allanite and ilmenite.

Apatite is usually between some 10 s of μm and 100 μm. It can be associated with zircon or ilmenite (Figure 9 d). In the first case, it is F-dominant, while in the second case, it is probably OH-dominant (based on F + Cl content lower than stoichiometrically required), although it usually has a low Cl-content as well. Zircon occurs as euhedral to subhedral, usually isometric grains. Its maximum grain size is around 100 μm and occasionally can be detected even with an optical microscope. Allanite from the quarry is partly decomposed along its edge and surrounded by submicrometric monazite crystals (Figure 9 e), which are probably generated from the remobilized REE of the allanite crystals. The chemical composition of the allanite from the quarry differs from the ones from the heavy sand: it is slightly more enriched in REEs, has higher Fe and lower Si and Al concentrations. Ilmenite is usually subhedral. Its size can reach the same 100s of μm. Its Mn/Mg ratio is relatively high (0.5 – 1.4) and sometime have also a small V concentration. Based on the Fe/Ti ratio these ilmenites are also chemically unaltered. In sample TD-9 individual ilmenite crystals are rare, but the presence of intergrown grains with spinel-type Fe-oxides, Fe-Ti-oxides and Ti-oxides with ilmenite is usual. In such kind of composite grains rarely micrometric monazite and cassiterite inclusions can occur (Figure 9 f). Rarely, samples from the quarry also have spinel-type Fe-Ti-oxides, but it is less common. Only one heavy REE-dominant phosphate mineral was detected, in sample TD-9. As the electron beam was able to burn a hole in it, it is possible that this grain was not xenotime-(Y), but its water-bearing variety, churchite-(Y). It should be mentioned that earlier a postvolcanic hydrothermal Sn mineralization was detected in ignimbrite samples from the same quarry as the one sampled for this article (Szakáll and Kristály, 2021).

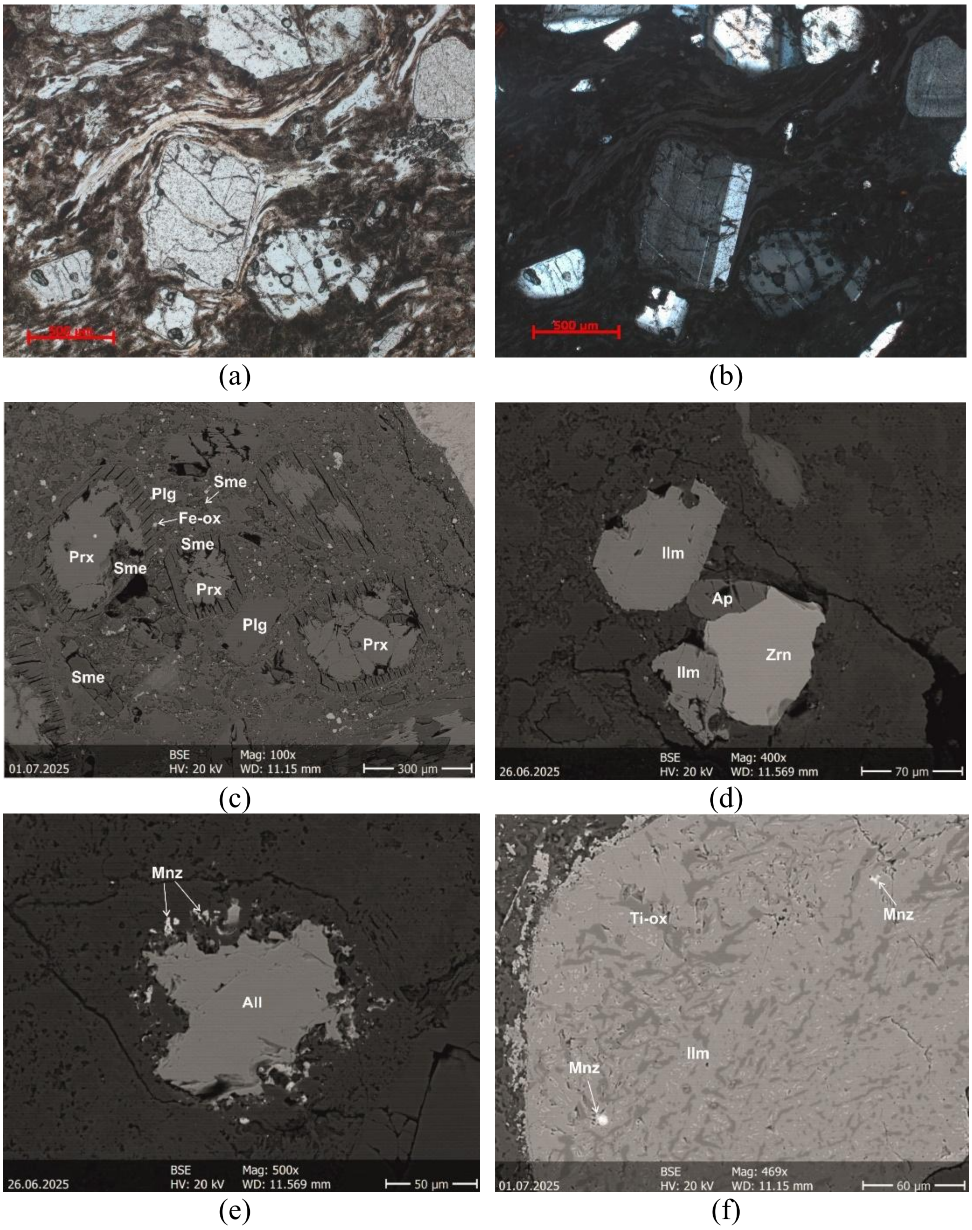

Figure 9

Optical microscopic (a–b) and BSE images of ignimbrite samples (c–f). (a–b): Typical texture of welded ignimbrite from the Tibolddaróc quarry with 1N and XN. (c) Weathered pyroxene and plagioclase crystals (d) Association of ilmenite, apatite and zircon. (e) Allanite with resorbed edges, surrounded by micrometric monazite crystals. (f) Intergrown texture of ilmenite and Ti-oxide, with monazite inclusions. (All = allanite, Ap = apatite, Ilm = ilmenite, Mnz = monazite, Plg = plagioclase, Prx = pyroxene, San = sanidine, Sme = smectite, Zrn = zircon)

5. Discussion and conclusions

The placer deposit studied near Tibolddaróc is enriched in heavy minerals, especially in ilmenite. All heavy minerals of the placer have angular grain shape, and the chemical composition of the ilmenite crystals is pure, without any sign of alteration (Fe/Ti ratio is stoichiometric). Based on these, the provenance territory is in the vicinity of the placer.

The Bükkalja region is characterized by Miocene volcanic formations, with variable erodibility. Generally, welded layers are less prone to being eroded than the unwelded ignimbrites and tuffs. This difference makes the landform of the area so diverse, with elevated plateaus and valleys (Biró et al., 2022). The rock varieties, which are more affected by the physical weathering processes can be the main source of heavy mineral accumulation in the short term. However, in the longer term the welded layers can also serve as a host, as they are more enriched in heavy minerals than tuff layers.

EDX analyses indicate different Mn/Mg ratios for ilmenite crystals from the studied welded ignimbrite samples from Tibolddaróc quarry and from the heavy sand. Similarly, the composition of allanite crystals is also not the same. Another heavy sand sample was collected and studied from the vicinity of Cserépváralja from a stream bed before this study (unpublished results). This sample is not so rich in ilmenite, but it contains similar minerals, again with slightly different composition. For example, allanite from this sample has a higher Fe content and a higher La/Ce ratio than in the ignimbrite from Tibolddaróc quarry.

The above findings indicate that the Miocene volcanic formations of the Bükkalja region in general can be an effective source of heavy mineral accumulation, but heavy mineral crystal chemistry within the Miocene volcanic formations is diverse. Systematic testing of the exact composition of the heavy minerals can be used as a tracer to identify the particular volcanic units and provenance territories of the placer deposits. Although the economic significance of the heavy mineral deposit is currently unknown, the high concentration of ilmenite in the heavy sand samples near Tibolddaróc makes it a potential raw material for future Ti-extraction, if its sufficiently large volume can be confirmed by subsequent research.

Acknowledgments

The work was supported by the University Research Scholarship Program of the Ministry for Culture and Innovation from the source of the National Research, Development and Innovation Fund. The authors thank the reviewers for their useful suggestions for improving the manuscript.

References

Anders, E., Grevesse, N. (1989). Abundances of the elements: Meteoritic and solar. *Geochim, Cosmochim, Acta*, 53, pp. 197–214. https://doi.org/10.1016/0016-7037(89)90286-X

Angusamy, N., Sahayam, J. D., Gandhi, M. S., Rajamanickam, G. V. (2005). Coastal placer deposits of Central Tamil Nadu, India. *Marine Georesources and Geotechnology*, 23, pp. 137–174. https://doi.org/10.1080/10641190500192102

Babinszki, E., Piros, O., Csillag, G., Fodor, L., Gyalog, L., Kercsmár, Z., Less, G., Lukács, R., Sebe, K., Selmeczi, I., Szepesi, J., Sztanó, O., Tóth, E. (eds.) (2024). *Lithostratigraphic units of Hungary II. – Cenozoic formations.* Szabályozott Tevékenységek Felügyeleti Hatósága, Budapest.

Bhattacharyya, S., Sengupta, R., Chakraborty, M. (1997). Elemental Chemistry of Ilmenite - An Indicator of Provenance? *Journal of the Geological Society of India*, 50, pp. 787–789. https://doi.org/10.17491/JGSI/1997/500616

Biró, T., Hencz, M., Németh, K., Karátson, D., Márton, E., Szakács, A., Bradák, B., Szalai, Z., Pécskay, Z., Kovács, I. J. (2020). A Miocene Phreatoplinian eruption in the North-Eastern Pannonian Basin, Hungary: The Jató Member. *Journal of Volcanology and Geothermal Research*, 401, p. 106973. https://doi.org/10.1016/J.JVOLGEORES.2020.106973

Biró, T., Hencz, M., Telbisz, T., Cseri, Z., Karátson, D. (2022). The relationship between ignimbrite lithofacies and topography in a foothill setting formed on Miocene pyroclastics – a case study from the Bükkalja, Northern Hungary. *Hungarian Geographical Bulletin*, 71, pp. 213–229. https://doi.org/10.15201/HUNGEOBULL.71.3.1

Bowles, J. F. W., Howie, R.A., Vaughan, D. J., Zussman, J. (2011). Non-silicates: volume 5A. Rock-forming minerals 920.

Csontos, L., Nagymarosy, A., Horváth, F., Kovác, M. (1992). Tertiary evolution of the Intra-Carpathian area: A model. *Tectonophysics*, 208, pp. 221–241. https://doi.org/10.1016/0040-1951(92)90346-8

Czuppon, G., Lukács, R., Harangi, S., Mason, P. R. D., Ntaflos, T. (2012). Mixing of crystal mushes and melts in the genesis of the Bogács Ignimbrite suite, northern Hungary: An integrated geochemical investigation of mineral phases and glasses. *Lithos*, 148, pp. 71–85. https://doi.org/10.1016/J.LITHOS.2012.06.009

Downs, R.T., Hall-Wallace, M. (2003). The American Mineralogist crystal structure database. *American Mineralogist*, 88, pp. 247–250.

Ganzha, O., Okholina, T., Kroshko, Y., Kuzmanenko, H., Kovalchuk, M. (2023). Structural and Lithological Models of Ilmenite Placer Deposits in Ukraine. *Anuario do Instituto de Geociencias*, 46. https://doi.org/10.11137/1982-3908_2023_46_55949

Harangi, Sz., Mason, P. R. D., Lukács, R. (2005). Correlation and petrogenesis of silicic pyroclastic rocks in the Northern Pannonian Basin, Eastern-Central Europe: In situ trace element data of glass shards and mineral chemical constraints. *Journal of Volcanology and Geothermal Research*, 143, pp. 237–257. https://doi.org/10.1016/J.JVOLGEORES.2004.11.012

Hencz, M., Biró, T., Németh, K., Szakács, A., Portnyagin, M., Cseri, Z., Pécskay, Z., Szabó, C., Müller, S., Karátson, D. (2024). Lithostratigraphy of the ignimbrite-dominated Miocene Bükk Foreland Volcanic Area (Central Europe). *Journal of Volcanology and Geothermal Research*, 445, p. 107960. https://doi.org/10.1016/j.jvolgeores.2023.107960

Herz, N., Valentine, L. E., Iberall, E. R., Hickel, W. J., Pecora, W. T. (1970). Rutile and ilmenite placer deposits, Roseland district, Nelson and Amherst Counties, Virginia. *Bulletin*. https://doi.org/10.3133/B1312F

Kolb, J., Keiding, J. K., Steenfelt, A., Secher, K., Keulen, N., Rosa, D., Stensgaard, B. M. (2016). Metallogeny of Greenland. *Ore. Geol. Rev.*, 78, pp. 493–555. https://doi.org/10.1016/J.OREGEOREV.2016.03.006

Kovács, I., Szabó, C. (2008). Middle Miocene volcanism in the vicinity of the Middle Hungarian zone: Evidence for an inherited enriched mantle source. J *Geodyn*, 45, pp. 1–17. https://doi.org/10.1016/j.jog.2007.06.002

Lattard, D. (1995). Experimental evidence for the exsolution of ilmenite from titaniferous spinel. *American Mineralogist*, 80, pp. 968–981. https://doi.org/10.2138/AM-1995-9-1013

Lukács, R., Harangi, S., Gál, P., Szepesi, J., Di Capua, A., Norini, G., Sulpizio, R., Groppelli, G., Fodor, L. (2022). Formal definition and description of lithostratigraphic units related to the Miocene silicic pyroclastic rocks outcropping in Northern Hungary: A revision. *Geologica Carpathica*, 73, pp. 137–158. https://doi.org/10.31577/GeolCarp.73.2.3

Lukács, R., Harangi, S., Guillong, M., Bachmann, O., Fodor, L., Buret, Y., Dunkl, I., Sliwinski, J., von Quadt, A., Peytcheva, I., Zimmerer, M. (2018). Early to Mid-Miocene syn-extensional massive silicic volcanism in the Pannonian Basin (East-Central Europe): Eruption chronology, correlation potential and geodynamic implications. *Earth Sci. Rev.*, 179, pp. 1–19. https://doi.org/10.1016/J.EARSCIREV.2018.02.005

MacDonald, W.G., Rozendaal, A. (1995). The Geelwal Karoo heavy mineral deposit: a modern day beach placer. *Journal of African Earth Sciences*, 21, pp. 187–200. https://doi.org/10.1016/0899-5362(95)00082-5

Mücke, A., Bhadra Chaudhuri, J. N. (1991). The continuous alteration of ilmenite through pseudorutile to leucoxene. *Ore. Geol. Rev.*, 6, pp. 25–44. https://doi.org/10.1016/0169-1368(91)90030-B

Murphy, P., Frick, L. (2006). Titanium, in: Barker, J. M., Kogel, J. E., Trivedi, N. C., Krukowski, S.T. (eds.). Industrial Minerals & Rocks : Commodities, Markets, and Uses. *Society for Mining, Metallurgy, and Exploration*, Littleton, Colorado, pp. 990–991.

Nayak, B., Mohanty, S., Bhattacharyya, P. (2012). Heavy Minerals and the Characters of Ilmenite in the Beach Placer Sands of Chavakkad-Ponnani, Kerala Coast, India. *Journal of the Geological Society of India*, 79, pp. 259–266. https://doi.org/10.1007/S12594-012-0046-7

Prates Hallal, G., Porcher, C. C., Veettil, B. K., De Almeida Espinoza, J.M., Beatriz Alves Rolim, S. (2025). Distribution of ilmenite minerals in placer deposits along the middle coast of Southern Brazil using spaceborne and ground-based remote sensing. *PLoS One*, 20, e0314238. https://doi.org/10.1371/JOURNAL.PONE.0314238

Rahman, A., Tardio, J., Bhargava, S. K., Zaman, M. N., Hasan, A. S. M. M., Torpy, A., Pownceby, M.I. (2020). Comparison of the chemistry and mineralogy of ilmenite concentrates sourced from fluvial (Brahmaputra River) and beach placer (Cox's Bazar) deposits, Bangladesh. *Ore. Geol. Rev.*, 117, p. 103271. https://doi.org/10.1016/J.OREGEOREV.2019.103271

Ramakrishnan, C., Mani, R., Babu, D. S. S. (1997). Ilmenite from the Chavara deposit, India: a critical evaluation. *Mineral Mag.*, 61, pp. 233–242. https://doi.org/10.1180/MINMAG.1997.061.405.06

Roy, P. S. (1999). Heavy mineral beach placers in southeastern Australia; their nature and genesis. *Economic Geology*, 94, pp. 567–588. https://doi.org/10.2113/GSECONGEO.94.4.567

Rudnick, R., Gao, S. (2013). Composition of the Continental Crust. *Treatise on geochemistry*, 4. https://doi.org/10.1016/B978-0-08-095975-7.00301-6

Schipper, C., Rickard, W., Reddy, S., Saxey, D., Castro, J., Fougerouse, D., Quadir, M., Conway, C., Prior, D., Lilly, K. (2020). Volcanic SiO2-cristobalite: A natural product of chemical vapor deposition. *American Mineralogist*, 105, pp. 510–524. https://doi.org/10.2138/am-2020-7236

Szakács, A., Márton, E., Póka, T., Zelenka, T., Pécskay, Z., Seghedi, I. (1998). Miocene acidic explosive volcanism in the Bukk Foreland, Hungary: Identifying eruptive sequences and searching for source locations. *Acta Geologica Hungarica*, 41, pp. 413–435.

Szakáll, S., Kristály, F. (2021). Cassiterite in quartz-feldspar veinlets of ignimbrite (Southern Bükk Mts., Hungary). *Acta Mineralogica Petrographica Abstract*, Series 11, p. 42.

Wassef, S.N. (1981). Distribution and properties of placer ilmenite in East Rosetta beach sands, Egypt. *Miner Depos*, 16, pp. 259–267. https://doi.org/10.1007/BF00202739/METRICS

Wells, H. C., Haverkamp, R. G. (2020). Characterization of the Heavy Mineral Suite in a Holocene Beach Placer, Barrytown, New Zealand. *Minerals*, Vol. 10, p. 86. https://doi.org/10.3390/MIN10020086

Geosciences and Engineering, Vol. 13, No. 2 (2025), pp. 125–139.
https://doi.org/10.33030/geosciences.2025.02.009

GIS-BASED SPATIAL ANALYSIS OF THE KAKASVÁR ARCHAEOLOGICAL SITE

ANDRÁS DOBAI[1, *], TAMÁS DEÁK[2], ANDRÁS GÖMÖRI[3], ENDRE DOBOS[4]
[1, *] *Institute of Geography and Geoinformatics, University of Miskolc;*
andras.dobai@uni-miskolc.hu
[2]*Institute of Geography and Geoinformatics, University of Miskolc;*
tamas.deak@uni-miskolc.hu
[3]*Institute of Geography and Geoinformatics, University of Miskolc;*
gomori.andras@student.uni-miskolc.hu
[4]*Institute of Geography and Geoinformatics, University of Miskolc;*
endre.dobos@uni-miskolc.hu
[1]https://orcid.org/0000-0002-5268-0728
[2]https://orcid.org/0009-0001-1360-4159
[3]https://orcid.org/0009-0001-4323-5796
[4]https://orcid.org/0000-0002-9798-6376

Abstract: The Battle of Muhi (1241), widely regarded as a major national catastrophe in Hungarian history, has been a focal point of archaeological research for over seven centuries. Investigating the battlefield landscape and the associated 13th-century settlement system requires an interdisciplinary approach. This study presents a new GIS-based analytical method that integrates a high-resolution light detection and ranging (LiDAR)-derived digital elevation model and a Relative Elevation Model (REM), which were applied to enhance subtle micro-topographic contrasts within the low-relief floodplain environment. These tools were used to reconstruct former hydrological systems, enabling the precise spatial identification of the Kakasvár, which may have held regional historical significance.

Keywords: *GIS, Battle of Muhi, LiDAR, REM, spatial analysis, hydrological datasets*

1. INTRODUCTION

Research on the Battle of Muhi has constituted a defining component of archaeological and historical scholarship for more than a century. Over recent decades, this field has undergone a marked methodological shift towards increasingly integrative and data-driven approaches. Non-destructive survey techniques (e.g., metal-detecting survey), community archaeology, and LiDAR-based terrain modelling have become integral elements of archaeological research. These approaches have significantly expanded both the empirical basis and the interpretative potential of battlefield investigations (Laszlovszky J., 2003; P. Szabó S., 2022). As a result, a growing corpus of professional databases and synthetic studies is now available (Négyesi L., 1997; Wolf M., 2014; Laszlovszky J. et al., 2014; Pusztai T. 2014). Today, the events of the battle, which took place in the midthirteenth century, are documented through detailed and multidimensional analyses focusing on battlefield reconstruction, contemporary settlement networks, and a range of related thematic questions. Despite these advances, significant research potential remains unexploited, particularly regarding the systematic analysis of foreign textual sources (Laszlovszky J. et al., 2014; P. Szabó S., 2022). At the same time, the comprehensive investigation of the entire battlefield remains an open research challenge, for which advanced digital methodologies may provide promising solutions (Laszlovszky J. and Rácz T. 2020). One possible response to this demand is provided by the methodology of Archaeological GIS, or Archaeo-GIS for short (Sarris, A. 2024). To date, the number of GIS-based studies related to the Battle of Muhi remains limited. Existing works have primarily focused on descriptive and visual analyses or relatively simple spatial queries. Notably absent are studies employing complex spatial databases, surface-related indices, or explicitly formulated analytical questions, such as those addressing catchment areas, hydrological networks, or terrain-driven accessibility. These limitations can be attributed in part to the high cost or restricted availability of high-resolution digital elevation models and other relevant spatial datasets (e.g. flood inundation boundaries or flood models), as well as to the specialised expertise required to extract meaningful information from such data. Consequently, the analytical potential of GIS-based approaches and associated spatial databases has not yet been fully exploited in research on the battle. The present study introduce a further stage in a multi-phase research programme. The project integrates physical geographical and archaeological data through the application of advanced GIS techniques. While closely connected to other ongoing investigations, its primary objective is not to intervene directly in existing archaeological interpretations, but rather to explore spatial and environmental relationships using the Archaeo-GIS methodologies. The study therefore focuses on identifying environmental and spatial patterns (particularly those related to terrain morphology, hydrology, and accessibility) and on applying methodological solutions that may contribute to a more detailed contextualisation of archaeological data. In addition, this study asks whether REM-enhanced LiDAR and Archaeo-GIS techniques can reliably identify anthropogenic micro-topography, thereby enabling a more precise localisation of human-made features and their discrimination from natural fluvial forms.

2. Materials and methods

2.1. Study area

The study area (Figure 1) is located within the Sajó–Hernád Plain. The mesoregion is an alluvial fan plain situated at an elevation between 89.5–160 m a.s.l. Its northern part lies at a lower elevation, while the southern areas rise island-like by 8–10 m higher. The surface morphology has been shaped primarily by the Sajó and Hernád rivers. As a result of fluvial erosion, the area has developed into a piedmont-type landscape dissected by low interfluves, with an average relief of approximately 5 m/km². The Muhi Plain, forming the floodplain area of the two rivers, is characterized by low relative relief and consists of a gently undulating plain covered by loess deposits (Dövényi Z., 2010). The geological evolution of the area is highly complex; however, this study focuses on the key stages relevant to the formation of the Sajó alluvial fan. The development of this section of the Sajó Valley was strongly influenced by the structural evolution of the Bükk Mountains and the Cserehát Hills, as well as by their tectonic changes and the northwestward shift of the Tisza River during the Pleistocene. The formation of the present-day channel orientation of the Sajó River was largely controlled by the gradual but intensive uplift of the northern foreland of the Bükk Mountains, which began in the Miocene (Gábris Gy., 1970).

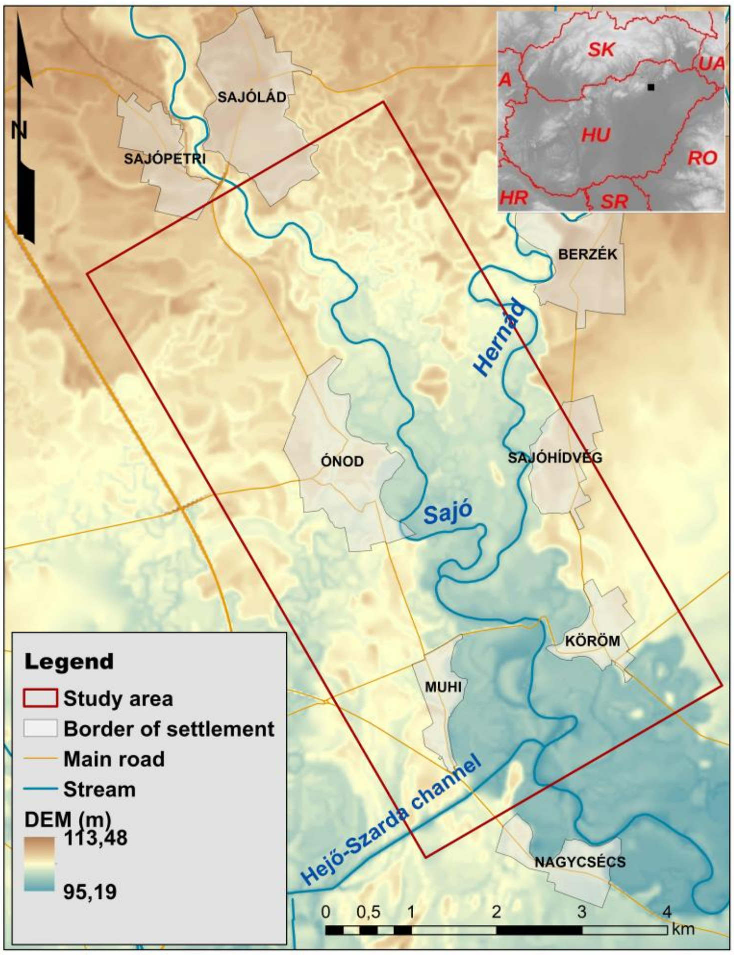

Figure 1.
Location of the study area

The establishment of the main channel direction of the Sajó started in the Late Miocene and continued into the Pliocene following Miocene volcanism (Mike K., 1972; Láng S., 1944). During this period, the Sajó and Hernád rivers joined the Tisza approximately 120 km south of their present confluence (Vadász E., 1960; Somogyi S., 1961). Due to the Pleistocene uplift of the initial section of the Sajó Valley, the river began gradual incision north of the Miskolc Gate, while strong aggradation commenced toward the south–southeast during the Pleistocene (Láng S., 1944). As a result of these processes, the lowland alluvial fan constructed by the two rivers was formed (Franyó F., 1966). During this period, the Sajó built an alluvial fan extending far into the Great Hungarian Plain. Surface aggradation of this fan was largely completed by the end of the Pleistocene, whereas sediment accumulation within the valleys continued until the Early Holocene. The development of the present hydrographic network of the Sajó River dates to the Holocene and, based on previous studies, is estimated to be approximately 5000 years old (Láng S., 1944). During the same period, both the Sajó and the Hernád rivers began to incise into their own alluvial fan deposits (Dövényi Z., 2010). The unified alluvial fan extends across the entire mesoregion. Its apex is located near Miskolc, and it stretches approximately 30 km southward with an average width of about 3 km (Dövényi Z., 2010; Csoma J., 1972). The section of the alluvial fan can be subdivided into several units representing different channel generations (Figure 2).

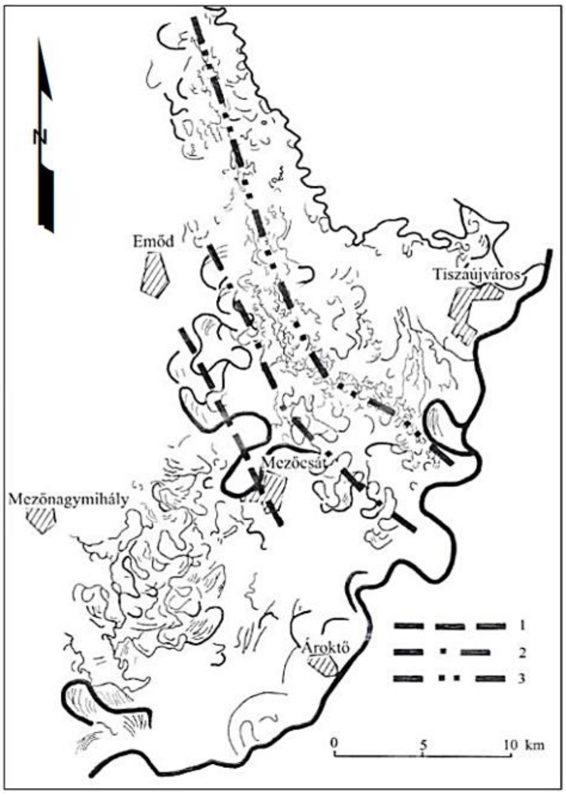

Figure 2
Palaeodrainage directions on the Sajó alluvial fan
during the Late Pleistocene–Holocene (Gábris Gy. 1970)

These form three distinct levels, separated by two phases of incision. The individual levels are delineated by well-defined erosional scarps. From the perspective of this study, the third channel-generation unit is of particular importance, as it demonstrates that during the subboreal humid phase of the Holocene, the Sajó–Hernád river system already flowed within its present channel. In subsequent periods, increased precipitation led to renewed incision into the alluvial fan on two occasions; however, neither the Sajó from the east nor the Hejő Stream from the west was able to completely breach the fan (Csoma J., 1972). Traces of these incision phases have been preserved despite aeolian modification and can be clearly identified on aerial imagery. The climate of the mesoregion is moderately warm and dry. The annual duration of sunshine ranges between 1850 and 1900 hours. Mean annual air temperature varies from 9.3–9.6 °C in the northern part of the area to 9.7–9.9 °C in the southern part. Approximately 60% of the annual precipitation falls between May and October, with maximum values occurring in June and minimum values in January–February. The spatial distribution of annual precipitation ranges between 540 and 580 mm. The aridity index is 1.20 in the northern part of the region and 1.30 in the southern part. The prevailing wind direction is from the north to northwest, with an average wind speed of 2.5 m/s (Dövényi Z., 2010). Soil types within the area show considerable spatial variability. Soils in the Sajó Valley are predominantly acidic, whereas those along the Hernád River are carbonate-rich or weakly acidic. On gravelly substrates, alluvial meadow soils and meadow soils have developed, with small patches of saline soils and steppe-like meadow solonetz soils. On loess-covered terraces, meadow chernozems and calcareous meadow chernozems are dominant, while brown forest soils occur toward the piedmont surfaces. Land use in the region is largely agricultural and closely reflects the natural environmental conditions described above (Dövényi Z., 2010).

2.2. Review of previous GIS-based studies in the study area

As an initial step, all available cartographic sources of the study area (land-use maps, historical military surveys, flood inundation boundaries) were integrated into a GIS database. A drainage network of the wider study area was derived from the Hungarian Water Directorate's digital elevation model (HydroDEM) with a spatial resolution of 5 m DEM, which, after filling surface artefacts (fill), was suitable for representing surface runoff. A 5 m spatial resolution DEM was selected as an optimal compromise between spatial detail and noise reduction in the low-relief floodplain environment. While higher-resolution datasets (e.g., 1 m) provide greater micro-topographic detail, preliminary tests indicated that they also amplify local surface irregularities related to vegetation remnants, ploughing patterns, and minor anthropogenic disturbances, which may obscure broader geomorphological structures. Conversely, coarser resolutions (e.g., 10 m) resulted in the loss of subtle elevation differences critical for identifying low-amplitude fluvial and anthropogenic landforms. The 5 m resolution therefore ensured sufficient sensitivity to micro-relief variations while maintaining geomorphological interpretability at the landscape scale. Based on these datasets, a geospatial framework was established for an area of approximately 140 km², including sub-catchments associated with the Hejő, Szinva and Sajó watercourses, as well as a vector dataset of flood inundation heights was obtained from the Flood Risk Management Plan prepared by the Hungarian Water Directorate (ÉMVIZIG, 2014), representing the maximum inundation extent of the 2010 flood event. Areas not affected by the Highest recorded Flood Level (HFL) were delineated and interpreted as permanently dry zones under present hydrological conditions. These areas were proposed as potential targets for archaeological research. While several zones coincide with previously investigated sites, additional areas were newly identified (Dobai A. and Dobos E., 2022). The spatial distribution of these zones corresponds well with the known structure of early medieval settlement networks, characterized by inter-settlement distances of approximately 2-3 km (P. Fischl K. and Pusztai T., 2018). Building upon these results, the second step of the research involved hydrological analyses focusing on narrower areas considered key for investigating the presumed site of the Battle of Muhi and early medieval settlement patterns. These analyses were conducted using a corrected DEM, from which present-day surface features (e.g., linear infrastructure) were manually removed, resulting in a new DEM. The new database was supplemented with DEM-derived parameters, including slope gradient, surface flow accumulation, and the topographic wetness index (TWI). In addition, sub-catchments associated with right-bank outflow points of the Sajó River were identified and analysed (Dobai A. and Dobos E., 2023).

The results demonstrate that the extracted drainage branches are not artefacts produced by flow accumulation algorithms, but represent real, former drainage paleochannels. Along the Hungarian reach of the Sajó River, floodplain basins are predominantly located on the left bank; however, the investigated Szirma–Sajóörös basin represents a right-bank floodplain system. Within this basin, three former Sajó branches were identified, which may become reactivated during flood events exceeding the HFL. One of these channels, referred to as the Sajó III–Ónod branch, emerges at river km 34 + 100 of the Sajó River, near the flood protection levee of Ónod settlement. The channel crosses Ónod over approximately 3.5 km in a northeast–southwest direction and connects to a southward-flowing channel that does not rejoin the Sajó River. Instead, the multi-branch drainage system can be traced to the administrative border of Szakáld (Dobai A. and Dobos E., 2023). Several segments of these former channels are also identifiable on maps of the First Military Survey. A former confluence of the Bársonyos Stream is located approximately 1.2 km northeast of the Sajó III–Ónod palaeochannel. No research has yet been conducted on the relationship between the two channels. It should be noted that a more detailed survey of the former Hernád catchment warrants a separate investigation, as it reveals extensive, continuous drainage networks that in several locations are connected to the contemporary floodplain of the Hernád River at river kilometres 3 + 500 and 5 + 100. The results of József Laszlovszky's investigation into the shared channel system of the Hernád and Sajó pertain to the area between river kilometre 34 + 000 of the Sajó and 2 + 500 of the Hernád (Laszlovszky J. and Nagy B., 2023). The size of the catchment is also explained by the presence of a multi-order flow network within the area. Based on the analysis of the vector datasets, it was determined that certain right-bank sections of the river can typically be regarded as suitable for the establishment of bridgeheads providing a river crossing. This suitability is attributed to the presence of the Sajó River's channels (Sajó I, II, III), which, in the absence of modern flood protection structures, drain excess floodwater more efficiently during high-flow events. Consequently, the hydraulic force of the flood wave is reduced, relieving a substantial portion of the riverbanks from flood-related stress. This pattern is corroborated by the flood inundation boundaries recorded by the North Hungarian Water Directorate during the 2010 flood event.

As a third step of the research, the narrowed study areas were subdivided into 3 km × 3 km zones (A, B, C, D) and 1.5 km × 1.5 km subzones (A1, B2, C3, etc.), reducing the examined sample area to 36 km². In the following, the steps undertaken for the identification of the site located in subzone D1 are presented (Figure 3).

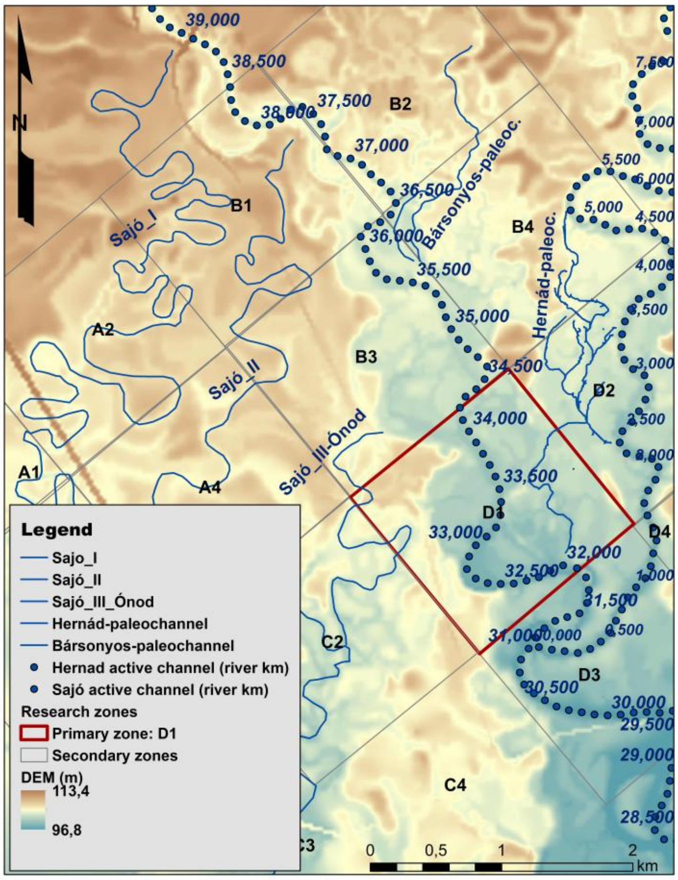

Figure 3.
Summary map of previous GIS-based analysis in the study area

2.3. Presentation of the new GIS methodology

In the present study, the database containing the previously presented datasets was supplemented with additional raster layers and terrain-descriptive indices. As a first step, different flood stages (Grades I–III), as well as the Highest recorded Flood Level (HFL) of 2010, were delineated on a pre-produced digital elevation model (DEM) provided in geoTIFF format by Envirosense Ltd., derived from a UAV-based LiDAR (Light Detection and Ranging) survey. The study relied exclusively on this ready-made DEM product because the raw LiDAR point cloud and detailed preprocessing metadata were not accessible. Consequently, the underlying technical parameters could not be fully assessed. These flood inundation boundaries define the spatial extent of floodplain dynamics within the Sajó River corridor and identify areas that are no longer regularly flood-affected. For subsequent analyses, these areas were designated as *stable banks*, adopting terminology from practical water management, a concept essentially equivalent to *high banks* (HGD 147/2010), as this term more precisely captures the functional characteristics relevant to the objectives of the present study. The delineation of stable banks was necessary to enable the measurement of distances between riverbank sections defined by the maximum observed inundation extent and associated discharge conditions. These calculations can provide an adequate basis for identifying potential crossing points along the Sajó River, as such locations may play an important role in analyses of both the 13th century settlement network and issues related to the Battle of Muhi. In addition, a Relative Elevation Model (REM) was generated for the study area. The REM is a spatial data model that represents variations in surface elevation relative to a defined reference level rather than absolute elevation values (John M. R. et al., 1998; Kairis and Rybczyk, 2010). The REM used for geomorphological analysis was computed as the difference between the working DEM and a smoothed floodplain reference surface (REM = DEM − reference_surface). The reference surface was produced by applying a low-pass smoothing filter (moving-window mean: 50 m window) to the DEM to remove micro-topographic noise while retaining the regional floodplain slope. To account for the scale-dependent expression of floodplain landforms, additional REM layers were generated using different window sizes. Smaller window sizes (10–20 m) enhanced short-wavelength features such as levees and scroll bars, while intermediate windows (30–60 m) emphasized abandoned channels and depressions. Larger windows (>80–100 m) progressively suppressed local relief and highlighted broader floodplain gradients. This multi-scale approach allowed us to distinguish geomorphological units of different spatial extents and ensured that the interpretation was not biased by a single smoothing scale (Greco, S. et al., 2008). The application of the REM facilitates the identification of geomorphological features such as valleys, ridges, and slopes, and, in combination with the delineated flood inundation boundaries, supports further spatial analyses.

3. Results

The examination of the riverbank zones was conducted based on previously established 2-3 km distance criteria and the results of the Relative Elevation Model

(REM). According to the REM analysis, on the left bank of the Sajó River, approximately 240 m from the river's centerline, 683 m southeast of the Ónod Castle, and 623 m from the remains of the Sajóhídvégi Church, a topographically distinct, isolated landform was identified (Figure 4).

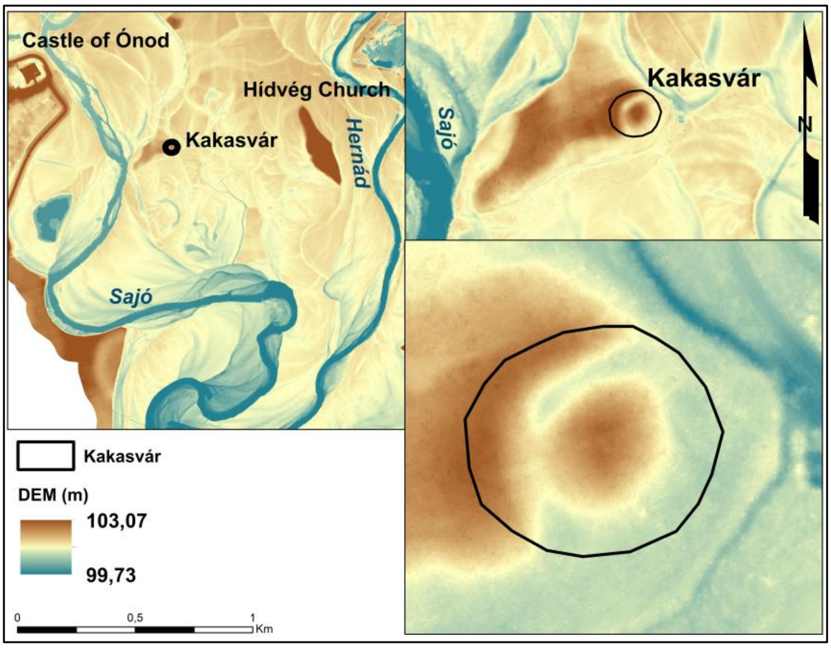

***Figure 4**.*
Result of the REM analysis and location of Kakasvár site

The Sajó–Hernád Plain is generally characterized by a low-relief, monotonous flat surface (Dövényi Z., 2010). In contrast, the investigated landform rises on average about 2 m above its surroundings, showing stronger erosional features on its southern and eastern slopes. It is located within a stagnant flow zone that is only minimally affected by floods, exhibiting flow velocities of merely 0.0–0.5 m/s even under extremely high-water conditions. This velocity range is insufficient to generate channel-forming discharge. The delineation of flow zones is based on sand transport and deposition velocities, providing a suitable basis for interpreting historical channel migration processes in the area (Kiss P., 2018). Based on the I., II., and III. Military Survey maps, as well as archival aerial imagery from fentrol.hu and Google Earth, the area appears to have been continuously forested over an extended period. The landform is situated on the outskirts of Ónod, on plot number 0159, within the area referred to as Kakasvár (Ónod Urban Development Plan, 2014). The site remains forested with dense undergrowth; consequently, only approximate dimensions can be provided until further excavations are conducted. The principal characteristics of the site are summarised in Table 1.

Table 1

Morphometric and spatial characteristics of the Kakasvár site

Parameter	Value	Parameter	Value
Total site area	2006 m²	**Inner circular area**	~496 m²
Highest elevation of inner area (m, a.s.l.)	102.8	**Outer circular + moat area**	1510 m^2
Lowest elevation of outer area (m, a.s.l.)	100.7	**Percentage of inner area**	~24.7%
Elevation difference (inner–outer)	2.1 m	**Length of semicircular ridge**	~60 m

Based on the GIS-derived morphology, the site appears to consist of a near-circular central platform enclosed by a surrounding moat and an outer, topographically elevated zone (Figure 5). The inner plateau represents the feature's highest ground, forming a relatively level surface that contrasts with the adjacent terrain, while the moat constitutes a pronounced and continuous depression encircling it. This concentric arrangement enhances the visual and morphological coherence of the feature. A semicircular ridge borders the circular form along a north–south sector. The circular feature is sharply separated from the outer ridge, indicating deliberate detachment, and a connecting sector on the western side appears to have developed secondarily possibly through the deposition of eroded material. Although the site's position might initially suggest an alluvial origin, its morphology and structural relationships may be consistent with anthropogenic modification. The proximity of abandoned channel forms suggests that past hydrological processes significantly influenced the local microrelief, contributing to sediment redistribution and subtle elevation contrasts. At the same time, the position of the landform on a slightly elevated fan remnant would have provided comparatively stable ground conditions within an otherwise flood-prone setting.

The present description is based exclusively on geomorphological observations and spatial relationships; therefore, it does not constitute archaeological proof in itself. Rather, it provides a terrain-based interpretation of the feature's form and environmental context. While the morphological characteristics may suggest anthropogenic modification, such an assessment remains hypothetical at this stage. The feature may be of anthropogenic origin, but its function and chronology require confirmation through targeted subsurface investigation and systematic archaeological verification.

The surveyed area was designated as *Kakasvár* based on the name appearing in the urban development plan of Ónod. The site was further validated using the map from 1791 (HU MNL BAZML IV.501.e. 2393/1791) by the National Archives of

Hungary, which shows a precise correspondence with the location. Based on the analysis of archival and digital sources, the identified area may have held regional significance. Its spatial relationship to flood inundation limits and to Hídvég Church may indicate a potential association with river crossing locations along the Sajó, potentially contributing to the socio-economic functioning of the surrounding landscape. The precise localization of the Kakasvár thus provides a more reliable spatial framework for interpreting its role within the regional context.

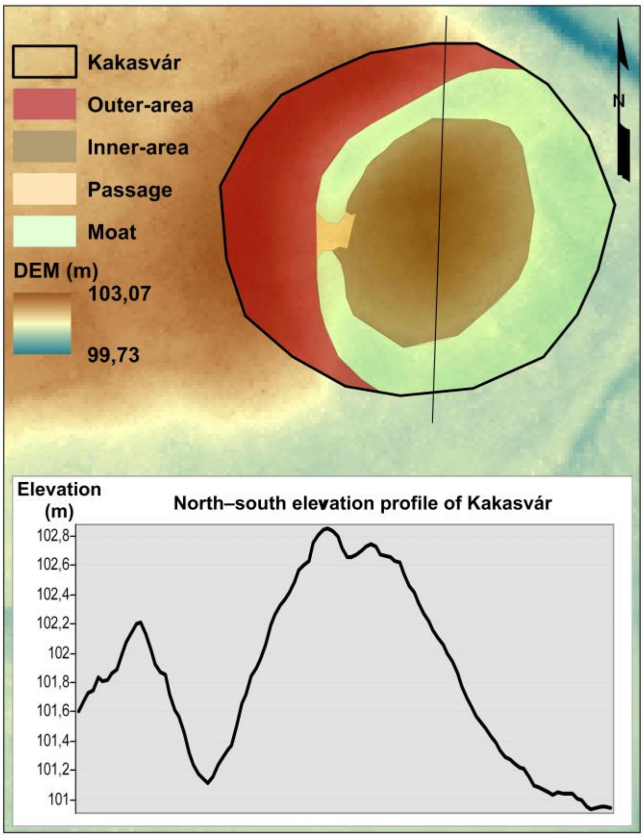

Figure 5
Structure of Kakasvár and north–south longitudinal elevation profile

4. DISCUSSION AND CONCLUSIONS

Despite several centuries of scholarly research, the reconstruction and interpretation of the Battle of Muhi and its contemporary settlement network continue to pose significant challenges to researchers in the field. The aim of the present study was to demonstrate how Archaeo-GIS methodologies based on high-resolution topographic data and complex spatial analyses can contribute to a more precise understanding of spatial and environmental relationships, thereby contributing a methodological perspective that may support ongoing research into the Battle of Muhi and the 13th-century regional settlement system. In a geomorphologically subtle floodplain environment, the precise localisation of the Kakasvár presents considerable methodological challenges without high-resolution topographic modelling and systematic hydrological analysis. Previous investigations, relying primarily on historical maps, surface observations, and approximate spatial correlations, therefore faced inherent limitations in achieving spatial precision.

The integration of high-resolution LiDAR-derived DEMs, flood inundation data, Relative Elevation Models (REM), and hydrological indices enabled the identification of subtle terrain features that are not discernible through traditional cartographic sources or conventional field observation and survey alone. In a low-relief floodplain environment such as the Sajó–Hernád Plain, even minor elevation differences of 1–2 m may have had substantial functional significance in terms of flood safety, accessibility, and visibility. The REM-based analysis proved particularly effective in highlighting isolated relict landforms embedded within an otherwise monotonous alluvial surface, enabling the clear spatial separation of the Kakasvár feature from surrounding geomorphological units. The applied workflow is transferable to other floodplain analysis along major river systems such as the Tisza and the Danube River, provided that DEM resolution is carefully selected and hydrological parameters are locally calibrated. In such environments, reliable identification of anthropogenic features is contingent upon the joint interpretation of relative elevation and flood dynamics rather than on morphological observation alone.

On the basis of the applied spatial terrain analysis, the identified landform at Kakasvár exhibits a combination of characteristics that may indicate anthropogenic modification. Its circular morphology, moat-like depression, outer elevated zone, and spatial detachment from surrounding sedimentary structures are difficult to explain solely by fluvial or aeolian processes. Such settings could potentially have provided favourable conditions for river crossing or controlled movement across the floodplain. The precise origin and potential chronological attribution of the feature require confirmation through future archaeological investigations.

In methodological terms, the study highlights the value of Archaeo-GIS approaches that move beyond descriptive mapping and apply analytically defined spatial criteria. The integration of flood inundation boundaries, stagnant flow zones, and relative elevation as interpretative variables offers a replicable workflow applicable to other lowland battlefield and settlement studies. At the same time, the research also underscores current limitations, particularly the need for higher-resolution subsurface data (e.g., Ground-penetrating radar [GPR], magnetometry) and systematic archaeological verification to complement GIS-based interpretations. While the exact function and chronology of the site remain open questions, the GIS-based analyses presented here provide a robust spatial and geomorphological toolkit for future investigations. The results support the view that interdisciplinary integration of archaeology, physical geography, and geoinformatics is essential for advancing the understanding of medieval conflict landscapes, especially in geomorphologically subtle lowland environments.

ACKNOWLEDGMENTS

We would like to express our gratitude to dr. Tamás Pusztai and István Dobai for their professional support, and to Tamás Bodnár, Vice Director and Archivist of the Borsod-Abaúj-Zemplén County Archives, for providing the map materials necessary for the research. We also thank Fruzsina Félegyházi for her valuable assistance. Furthermore, we thank Envirosense Ltd. for providing the LiDAR survey data. We would also like to express our gratitude to the Mayor's Office of Ónod for their assistance.

REFERENCES

Csoma J. (1972). *A Sajó hidrográfiája*. Vízrajzi Atlasz Sorozat 13. Sajó. 1. Hidrogárfia, geomorfolgia, VITUKI, Budapest, pp. 8–14.

Dobai A., Dobos E. (2022). Térinformatikai eljárások alkalmazása a régészeti kutatások támogatásához *Új eredmények a műszaki föld-és környezettudományban*. A Műszaki Földtudományi Kar konferencia kiadványa, pp. 96–106. https://mfk.uni-miskolc.hu/files/20006/MFK2022kiadvany_vegleges.pdf

Dobai A., Dobos E. (2023). *GIS a régészet szolgálatában: A Muhi-csat*a. Az elmélet és gyakorlat találkozása a térinformatikában XIV, pp 360–361. https://giskonferencia.unideb.hu/arch/GIS_Konf_kotet_2023.pdf

Dövényi Z. (2010). *Magyarország kistájainak katasztere.* MTA Földrajztudományi Kutató Intézet, Budapest, pp. 736–759. https://hungarian-geography.hu/konyvtar/kistaj/Kistaj_cim.pdf

ÉMVIZIG (2014). *Nagyvízi mederkezelési terv készítése a Sajó-Tarna vízrendszerére*. (Szerződés száma: ÉM- VIZIG/Z1540370) A Takta-rendszer Szerencs vasúti híd- Sajó torkolat közötti szakaszának 08.NMT.08 tervszámú Nagyvízi Mederkezelési Terve. https://docplayer.hu/25651211-Nagyvizi-mederkezelesi-terv-keszitese-a-sajo-tarna-vizrendszerere.html

Franyó F. (1966). A Sajó-Hernád hordalékkúpja a negyedkori földtani események tükrében. *Földrajzi Értesítő*, 15, pp. 153–178.

Gábris Gy. (1970). *A folyóvíz felszínalakító tevékenysége Magyarországon*. pp 54–58. https://tef.elte.hu/phocadownload/Gabris_folyoviz_felszinalakito_ tevekenysege_Magyarorszagon.pdf

Greco, S., Larsen, Eric & Mann, J. , Tuil, Jahalel & Lowney, C. (2008). Relative Elevation Topographic Surface Modelling of a Large Alluvial River Floodplain and Applications for the Study and Management of Riparian Landscapes. *Landscape Research*, 33, pp. 461–486.
https://doi.org/10.1080/01426390801949149

HGD 147/2010 – Hungarian Government Decree (2010). 147/2010. (IV. 29.) 2. § 18. Korm. rendelet *a vizek hasznosítását, védelmét és kártételeinek elhárítását szolgáló tevékenységekre és létesítményekre vonatkozó általános szabályokról*, hatályos: 2025. 09. 26.

John, M. R., Callaway, J. C., Day, J. W. Jr. (1998). A relative elevation model for a subsiding coastal forested wetland receiving wastewater effluent. *Ecological Modelling*, Vol. 112, Issue 1, pp. 23–44, https://doi.org/10.1016/S0304-3800(98)00125-2.

Kairis, P. A., Rybczyk, John M. (2010). Sea level rise and eelgrass (Zostera marina) production: A spatially explicit relative elevation model for Padilla Bay, WA. *Ecological Modelling*, Vol. 221, 7, pp. 1005–1016. https://doi.org/10.1016/j.ecolmodel.2009.01.025.

Kiss P. (2018). *Térinformatikai módszerek alkalmazása a nagyvízi mederkezelési és a folyógazdálkodási tervek készítése során a Tisza folyó Tokaj-Tiszaújváros közötti szakaszán*. Szakdolgozat, Műegyetem, pp. 43–47.

Láng S. (1944). Geomorfológiai és hidrológiai tanulmányok Gömörben. III. A Sajó felső völgye és a rozsonyói medence. *Hidrológiai Közlöny*, 29, pp. 141–148.

Laszlovszky J. (2003). Tatárjárás és régészet. In: *Tatárjárás. Nemzet és emlékezet.* Nagy Balázs (ed.). Budapest, Osiris, pp. 453–468.

Laszlovszky J., Pow S., Pusztai T. (2014). A muhi csata és az 1241-es tatárjárás – Új régészeti és történeti megközelítések. Rosta Szabolcs – V. Székely György *"Carmen miserabile" A tatárjárás magyarországi emlékei. Tanulmányok Pálóczi Horváth András 70. születésnapja tiszteletére*. Kecskemét, Kecskeméti Katona József Múzeum, pp. 27–36.

Laszlovszky J., Nagy B. (2023). Mederváltozás és kontinuitás a Sajó folyó középkori átkelőhelyeinél: A Muhi csatatér kutatásához kapcsolódó földrajzi és régészeti vizsgálatok. *Századok*, 156, 5, pp. 943–962.

Laszlovszky J., Rácz T. (2020). Fémkeresős kutatások a Muhi csatatéren: Közösségi régészet, hadszínterek vizsgálata és a kapcsolódó módszertani kérdések. *Magyar Régészet*, 9 (4), pp. 70–80.

Mike K., (1972). A Sajó geomorfológiája, In: *Sajó.1.* Vízrajzi Atlasz sorozat 13. Hidrográfia , geomorfológia. Budapest, VITUKI, pp. 15–26

Négyesi L. (1997). A Muhi csata 1241 április 11. *Hadtörténeti Közlemények*, 2. sz, Műhely, https://epa.oszk.hu/00000/00018/00001/pdf/04negyesi.pdf

Ónod Urban Development Plan (2014). *Ónod településszerkezeti terv a külterületre.* http://onod.hu/Rendezesi_terv/Regi/Onod_kulterulet.pdf

P. Fischl K., Pusztai T. (2018). A dél-borsodi síkság bronzkori és középkori település struktúrájának összehasonlítása. In: In: Mérai, Dóra; Drosztmér, Ágnes;

Lyublyanovics, Kyra; Rasson, Judith; Papp Reed, Zsuzsanna; Vadas, András; Zatykó, Csilla (szerk.). *Genius loci - Laszlovszky 60*. Budapest, Magyarországm, Archaeolingua, 391 p. pp. 82–88., 7 p.

P. Szabó S. (2022): *Hadtudomány: Kínai nyelvű mongol kőtáblafelirat a Muhi csatáról*. pp.112–123. https://doi.org/10.17047/HADTUD.2022.32.2.112

Pusztai T. (2014): Buzogánnyal, tarsollyal és késtok-merevítővel eltemetett halott a muhi csatából. In: *"Carmen miserabile" A tatárjárás magyarországi emlékei. Tanulmányok Pálóczi Horváth András 70. születésnapja tiszteletére*. Rosta Szabolcs, V. Székely György (eds.). Kecskemét, Kecskeméti Katona József Múzeum, pp. 141–150.

Sarris, A. (2024). The polymorphism of archaeological GIS. Unfolding the archaeological dimensions of GIS . *Journal of Greek Archaeology*, 9, pp. 9–19. https://archaeopresspublishing.com/ojs/index.php/JGA/article/view/2731

Somogyi S. (1961). Hazánk folyóhálózatának fejlődéstörténeti vázlata. *Földrajzi Közlemények*, 9, pp. 25–50.

Vadász E. (1960). *Magyarország Földtana*. Budapest, Akadémia Kiadó, pp. 45–88.

Wolf M. (2014). Régészeti adatok a muhi csata történetéhez. In: *"Carmen miserabile" A tatárjárás magyarországi emlékei. Tanulmányok Pálóczi Horváth András 70. születésnapja tiszteletére*. Rosta Szabolcs, V. Székely György (eds.). 69-80. Kecskemét, Kecskeméti Katona József Múzeum, pp. 69–80.

Geosciences and Engineering, Vol. 13, No. 2 (2025), pp. 140–151.
https://doi.org/10.33030/geosciences.2025.02.010

MONITORING THE CONDITION OF URBAN GREEN SPACES THROUGH TIME-SERIES SATELLITE IMAGERY

PÉTER PECSMÁNY[1]*, JÁNOS VÁGÓ[2], ANDRÁS HEGEDŰS[3], LAJOS SZALONTAI[4], BEÁTA SISKÁNÉ SZILASI[5]

[1, *]*Institute of Geography and Geoinformatics, University of Miskolc;*
peter.pecsmany@uni-miskolc.hu
[1, *]*Institute of Mining and Energy, University of Miskolc*
[2]*Institute of Geography and Geoinformatics, University of Miskolc;*
janos.vago@uni-miskolc.hu
[3]*Institute of Geography and Geoinformatics, University of Miskolc;*
andras.hegedus@uni-miskolc.hu
[4]*Institute of Geography and Geoinformatics, University of Miskolc;*
lajos.szalontai@uni-miskolc.hu
[5]*Institute of Geography and Geoinformatics, University of Miskolc;*
beata.siskane@uni-miskolc.hu
[1]https://orcid.org/0000-0002-6047-3286
[2]https://orcid.org/0000-0001-6811-6649
[4]https://orcid.org/0009-0000-8249-5657
[5]https://orcid.org/0000-0003-2937-1721

Abstract: Urban green spaces are essential for maintaining city livability, particularly under increasing climate extremes such as prolonged droughts. This study evaluates the condition and changes of green areas in Mezőkövesd between 2017 and 2024 using Sentinel-2 satellite imagery. NDVI and the Green Surface Intensity Index (ZFI) were used to assess vegetation health and spatial distribution. Findings reveal a significant decline in vegetation from 2022 due to drought, highlighting the vulnerability of urban greenery. Although the average per capita green space exceeds WHO minimums, spatial disparities exist. Accessibility analyses show that several areas lack nearby recreational green spaces. Targeted greening and climate-resilient planting are recommended.

Keywords: *NDVI, Green Space Index, GIS, Sentinel-2*

1. INTRODUCTION

Urban green spaces play a key role in maintaining the livability of settlements, as they contribute to the regulation of the microclimate, the improvement of air quality, the reduction of noise pollution, and also provide recreational and aesthetic value. However, the increasingly frequent and severe weather extremes caused by climate change – such as prolonged droughts – pose a serious threat to the condition and extent of urban vegetation. For this reason, continuous monitoring of green spaces is of paramount importance not only in large cities but also in medium-sized towns such as Mezőkövesd.

Green space refers to the vegetated part of a given area or settlement (e.g., public parks, playgrounds, cemeteries, themed gardens, groves, tree-lined avenues, etc.) and plays an important ecological and aesthetic role, even on private properties. In contrast, "green area" is a specific land-use category defined in urban development plans, referring to public spaces primarily covered with vegetation and not intended for construction.

The aim of our research is to provide a comprehensive overview of the condition and changes of green spaces in Mezőkövesd between 2017 and 2024. For the analysis, we used advanced remote sensing techniques: we processed NDVI (Normalized Difference Vegetation Index) values derived from Sentinel-2 satellite data and analyzed ZFI (Green Space Intensity Index) values to map the changes observed during the vegetation periods. We also assessed the amount of green area per capita and its accessibility. The results reflect not only the current state of green infrastructure but can also serve as a foundation for future urban planning and green infrastructure development strategies.

Since the 1990s, as part of the study of urbanization processes, the analysis of green spaces and green areas as components of urban land use has come into focus. Major research themes include urban forests, urban heat islands, urban ecology, emissions (air pollution), urban structure, mental health, quality of life, well-being, and the concept of the "Green City" (Farkas et al., 2023).

The maintenance and availability of urban green areas for residents are an important part of current urban planning in Hungary and of environmental impact assessments in cities. GIS-based geoinformatics systems provide excellent tools for mapping green areas, establishing monitoring systems, tracking changes in condition, and identifying environmental problems.

The growth and transformation of cities involve not only changes in population numbers but also the scale and direction of urban spatial expansion. Both processes are closely linked to the mapping and characterization of green areas, for which the analysis of time-series satellite images is essential. In the rapidly changing urban world, researchers focus both on rapidly growing cities (Rafiee et al., 2009; Deng et al., 2019) and on the challenges of creating sustainable urban environments (Fórián & Hagymássy, 2009; Bokhari et al., 2022; Szigeti & Czédli, 2022; Siskáné & Szepesi, 2022) using this methodology. One of the challenges for researchers is to adapt the design of green areas to the characteristics of the urban environment, both in terms of plant species and spatial layout (Kisvarga & Horotán, 2023).

While the most dynamic changes can be observed in global and large-scale cities, increasing attention is being paid to the study of small and medium-sized towns, and today, municipal governments also recognize the importance of conducting such analyses (e.g., Bábolna 2014; Salgótarján 2024).

2. Geography of Mezőkövesd

Mezőkövesd is located at the southern foothills of the Bükk Mountains, at the junction of the Great Hungarian Plain and the North Hungarian Mountains, within two distinct natural geographic micro-regions: Bükkalja and Borsodi-Mezőség. The town lies on the coalesced alluvial fans of the Ostoros, Kánya, and Hór creeks. The study area has a warm and dry climate. The number of sunshine hours ranges between 1950 and 2000 per year. The annual mean temperature is around 10 °C, although climate models project a possible increase of up to 3 °C in the coming decades. Annual precipitation varies between 500 and 550 mm (Bihari et al., 2024).

Vegetation in both micro-regions was significantly altered by human activity by the Middle Ages, resulting in fragmented and variably degraded plant communities (Pifkó & Barina, 2004). According to the most recent CORINE Land Cover database, 73% of the municipality's administrative area is used as non-irrigated arable land, 7.7% is discontinuous urban fabric (~built-up areas), 6% is complex cultivation patterns, 5% is pasture, 2% is industrial and commercial area, 1.7% is covered by water bodies, and 1% is occupied by the airport. In addition, land uses such as orchards, recreational and sports facilities, forests, and shrublands each account for approximately 0.5-1% of the total area.

Mezőkövesd is the 4th most populous settlement in Borsod-Abaúj-Zemplén County, with a total population of 15,541 (as of January 1, 2024), covering an area of 100.49 km^2 and a population density of 162.3 inhabitants/km^2.

3. Materials and methods

To map the vegetation-covered areas of Mezőkövesd (hereinafter referred to simply as green spaces for simplicity), and to assess their condition, we used time-series satellite imagery. The satellite image analysis was carried out for the vegetation periods between 2017 and 2024, defined as March 1 to October 31 each year.

As the first step of the analysis, we used Google Earth Engine to automatically filter Sentinel-2 images with 10% cloud cover. From the datasets meeting this cloud cover criterion, we generated Normalized Difference Vegetation Index (NDVI) maps

$$NDVI_{t1} = \frac{NIR - RED}{NIR + RED} \tag{1}$$

This index is used to estimate photosynthetic activity and chlorophyll content in plants, as vegetation strongly reflects near-infrared (NIR) light and absorbs visible red (RED) light. NDVI values can be used to infer plant health, biomass quantity, and vegetation fertility — thus serving as an indicator of vegetation condition and density.

Based on the NDVI datasets calculated from satellite images taken at specific dates, we computed the average NDVI value for the vegetation period of each examined year

$$NDVI_{annual\ average} = \frac{1}{n}\sum_{i=1}^{n} NDVI_i \tag{2}$$

In addition, within the ArcGIS Pro software environment, we prepared the average NDVI map for the eight-year vegetation period (Figure 1/A). Furthermore, using the built-in Zonal Statistics tool in ArcGIS Pro, we calculated the standard deviation of the mean values for the examined years.

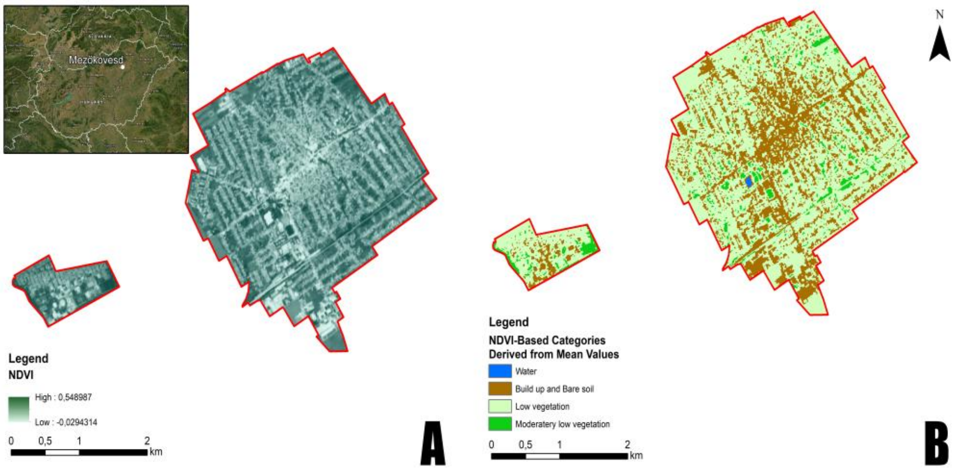

Figure 1
Spatial distribution of mean NDVI values (A) and vegetation categories classified based on those values (B)

As the second step, we calculated the Green Space Intensity Index (ZFI), developed by Jombach (2014). It is perfectly suitable for examining the condition, extent, and temporal changes of green spaces. Although the ZFI is based on the reclassification of NDVI values (Figure 2), it provides a much more intuitive and comprehensible representation of green space coverage than NDVI alone.

ZFI values range between 0 and 100, depending on the NDVI value of the given image element (pixel) (Jombach, 2014). The NDVI maps calculated for each year's vegetation period, as well as the average NDVI map for the entire study period, were reclassified in the ArcGIS Pro software environment to drive the ZFI values according to the method defined by Jombach (2014).

ZFI (%)	NDVI	Nature of the area	Sample
0%	(–1)–0	Built-up area, paved surface, mining area, bare soil surface, and any area without biologically active green cover.	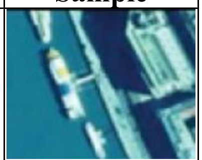
0.01–19.99%	0–0.1	E.g., heavily built-up areas with very low green cover ratio.	
20–39.99%	0.1–0.2	E.g., built-up area with low green cover ratio (densely built suburban area, residential park-like development).	

ZFI (%)	NDVI	Nature of the area	Sample
40–59.99%	0.2–0.3	E.g., medium built-up area with medium green cover ratio (suburban areas).	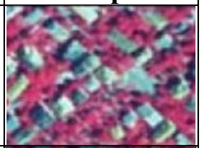
60–79.99%	0.3–0.4	E.g., relatively low built-up area with relatively high green cover ratio (housing estate development with large parks).	
80–99.99%	0.4–0.5	E.g., area characterized by low built-up density with a very high proportion of dense vegetation cover (gardens, parks, significant roadside green spaces).	
100%	0.5–1	Healthy forest stand, park with continuous woody vegetation and grass, vigorous lush grassland.	

Figure 2
Calculation method of the Green Space Intensity Index (ZFI)
based on Jombach (2014)

As the third step of our research, we used the ZFI map generated from the 8-year average NDVI values and the population data from the Hungarian Central Statistical Office (KSH) for the calculation of green space per capita.

In addition to the above analyses, major green areas (parks, playgrounds, and public cemeteries) within the built-up area were identified through field surveys, digitized based on satellite imagery, and their pedestrian accessibility was evaluated.

Using the Network Analyst module of ArcGIS Pro, we created isochrone maps to visualize the accessibility of these different types of green spaces within the city, with varying temporal resolution. The workflow of the research methodology can be seen in Figure 3.

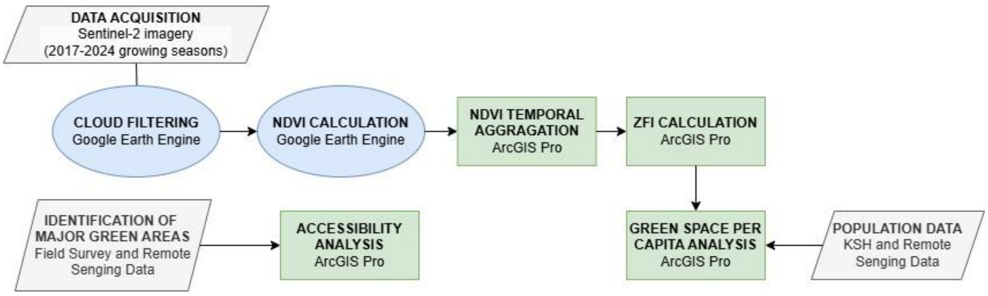

Figure 3
Workflow of the research

4. Results

4.1. NDVI

Based on the average NDVI values for the studied years, higher values (dark green) indicate healthier, denser vegetation — typically associated with continuous forest patches and tree rows — while lower values (light green) correspond to sparser vegetation or unvegetated areas. During reclassification, NDVI values (Figure 1/A) were divided into four categories based on relevant literature (Alex et al., 2017; Nascimento Aquino et al., 2018), as shown in Figure 1/B: water surfaces, built-up/bare areas, low-vegetation, and moderately low-vegetation zones. Their respective proportions are presented in Table 1.

Within the urban area, water surfaces account for the smallest share. The built-up class includes the town center as well as the large buildings of the Zsóry Spa recreational zone (e.g., hotels and the sanatorium area), and linear infrastructure. These areas make up 27.8% of the built-up area (only 3.5% of the total administrative area). The low-vegetation category primarily includes the densely built-up suburban residential zones surrounding the city center and represents the largest share (66.9%). The moderately low-vegetation class includes primarily wooded or forested patches along the railway line and within the Zsóry Spa area, accounting for approximately 5% (Table 1).

Table 1

The area and percentage share of the territories classified into each category

	Administrative area (ha)		**Build up area (ha)**	
Water	71.24	0.71%	0.81	0.09%
Build-up and bare soil	355.03	3.53%	254.37	27.77%
Low vegetation	9082.37	90.38%	613.09	66.93%
Moderately low vegetation	540.09	5.37%	47.73	5.21%

Examining the standard deviation of NDVI values (Figure 4), it can be observed that areas characterized by persistently low NDVI values and minimal temporal variability — primarily the city center and the main transport corridors connecting the town to the surrounding settlements — represent priority zones for targeted green infrastructure interventions. The stability and consistently low vegetation activity in these areas indicate a dominance of impervious or intensively managed surfaces, where ecological functions are limited.

The implementation of tree planting initiatives and the expansion of urban green spaces in these zones could significantly improve the local microclimate by reducing the urban heat island effect, enhancing evapotranspiration, and providing shading. In addition, increasing vegetation cover would contribute to biodiversity conservation by creating new habitats and ecological corridors, while also supporting carbon sequestration and reducing atmospheric carbon dioxide concentrations. Furthermore, such interventions could improve air quality, mitigate surface runoff during extreme precipitation events, and enhance the overall environmental resilience and livability of the urban environment.

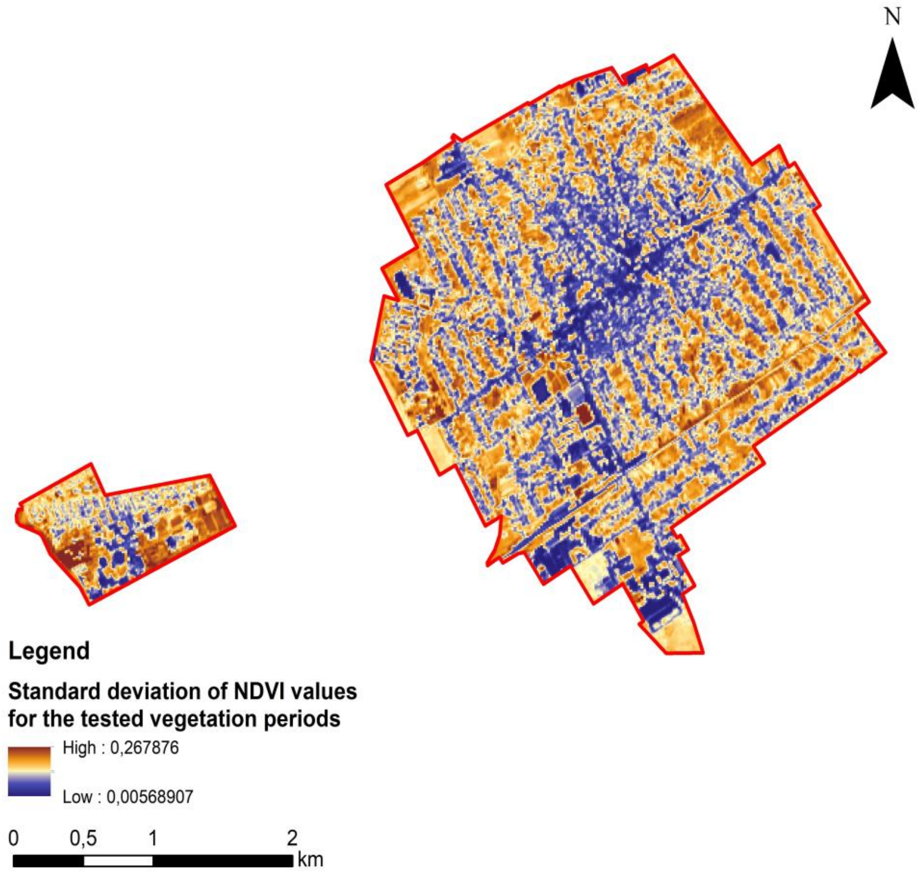

Figure 4
The standard deviation of NDVI values during the studied period from 2017 to 2024

4.2. ZFI

The extent of areas characterized by low building density and covered by a high proportion of dense vegetation (ZFI: 80–99%), as well as areas characterized by healthy forest stands and continuous woody vegetation and grassland (ZFI: 100%), remained nearly constant (~±7%) during this period (Figure 4). A drastic change can be observed starting from 2022, when the two aforementioned categories completely disappeared (Figure 5). This change is not primarily due to an increase in built-up areas, but rather to drought conditions that have increased the costs of maintaining green spaces. Rising irrigation expenses place an increasing burden on residents and local authorities. According to HungaroMET data, precipitation was minimal at the beginning of the year, and only scattered showers alleviated the drought from April to mid-August, while heatwaves increasingly worsened the situation. The time series analysis also highlights that this trend had been ongoing in previous years, and as a result, the vegetation was unable to regenerate naturally and adequately. Owing to global climate change, the Carpathian–Pannonian region increasingly experiences extreme weather events (e.g., drought or, conversely, excessive rainfall). Given this trend, it is advisable to plant native or non-native tree species in the city's parks in the near future that can tolerate drought and extreme conditions well.

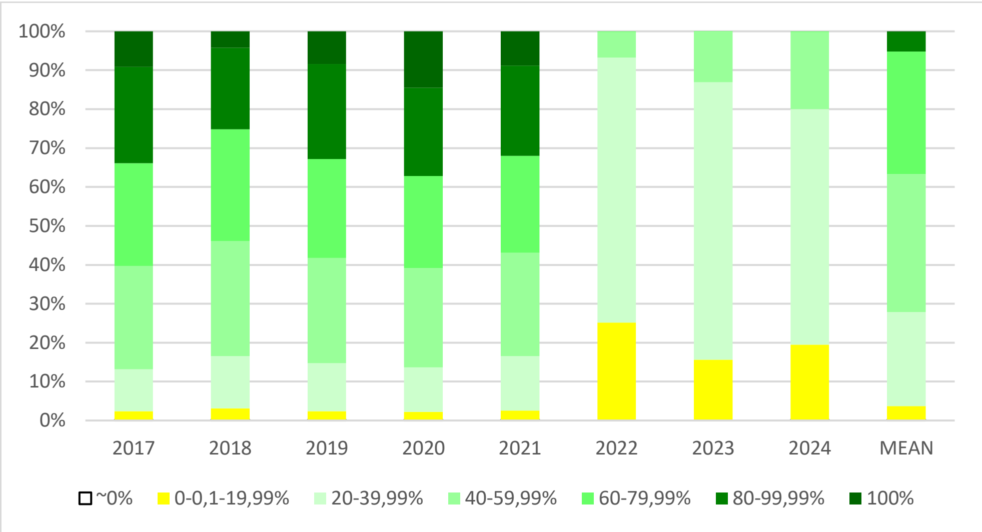

Figure 5

Change of the Green Surface Intensity Index (ZFI) in the inner area of Mezőkövesd (2017–2024)

4.3. Analysis of green space per capita

Due to significant changes in the condition of green spaces over the past three years caused by weather conditions, we used the ZFI map generated from the 8-year average NDVI values for further analyses (Figure 6). For the calculation of green space per capita, only areas with a ZFI value greater than 80% were considered. Based on the 2023 population data from the Hungarian Central Statistical Office (KSH) and the aforementioned criteria, the green space per capita within the inner urban area is 30.71 m^2, while within the entire administrative area it is 347.52 m^2. The value within the inner urban area exceeds the minimum recommended by the World Health Organization (WHO) (Russo & Cirella, 2018), which is 9 m^2, but falls short of the ideal value suggested by the organization, which is 50 m^2.

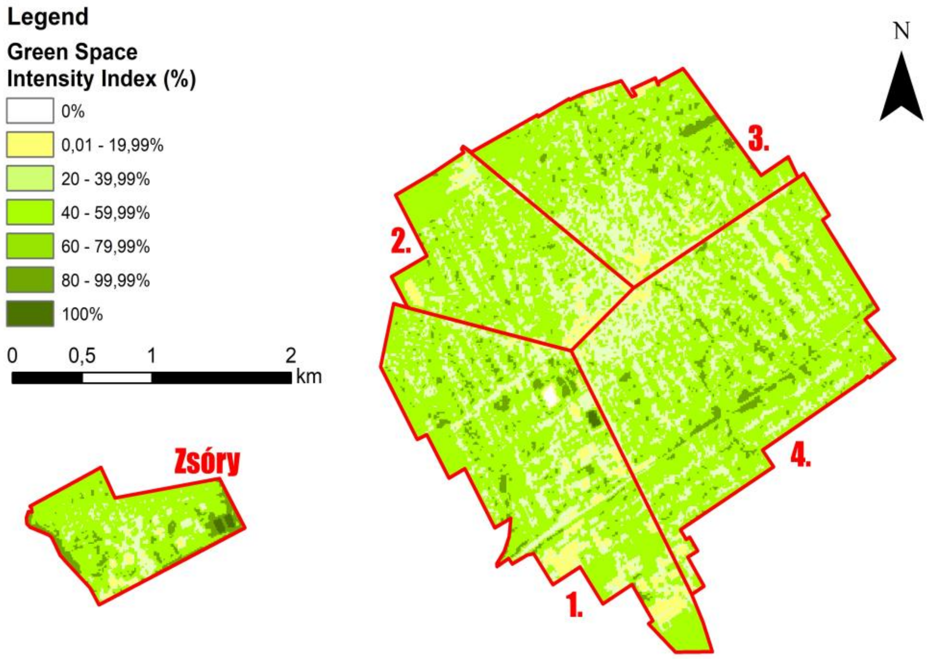

Figure 6
Zonal Green Space Intensity Index (ZFI) map generated from the 8-year average NDVI values

The urban area was divided into five sections based on the main roads. The population of each district was estimated by considering the number and type of properties located within the area. Subsequently, using the estimated population and the area of zones with a ZFI value above 80% in each district, we calculated the amount of green space per capita. According to the results, the Mezőkövesd-Zsóry area has the highest per capita green space, while the district number 2 has the lowest value, which falls just slightly below the minimum recommendation set by the WHO (Table 2).

Table 2
Estimated and calculated data of the individual city districts

	Estimated Population (persons)	**Area with ZFI above 80% (m^2)**	**ZFI per Capita (m^2)**
Mezőkövesd-Zsóry	300	114,200	**380.6667**
Mezőkövesd-1	3295	128,000	38.8467
Mezőkövesd-2	2272	20,100	**8.8468**
Mezőkövesd-3	4356	73,900	16.9651
Mezőkövesd-4	6150	141,100	22.9430

4.4. Distance from major green areas

Based on the recommendation of the World Health Organization, major green areas should be accessible within a minimum of 15 minutes of walking. Assuming an average walking speed of 4-5 km/h, this condition is practically met from almost the entire area of the city along the roads.

When examining the accessibility of public parks, which are most suitable for recreational purposes (see Figure 7, top right panel), the situation is similarly favorable — only from the eastern and western edges of the city (about 8% of the total area) does it take more than 15 minutes to reach them.

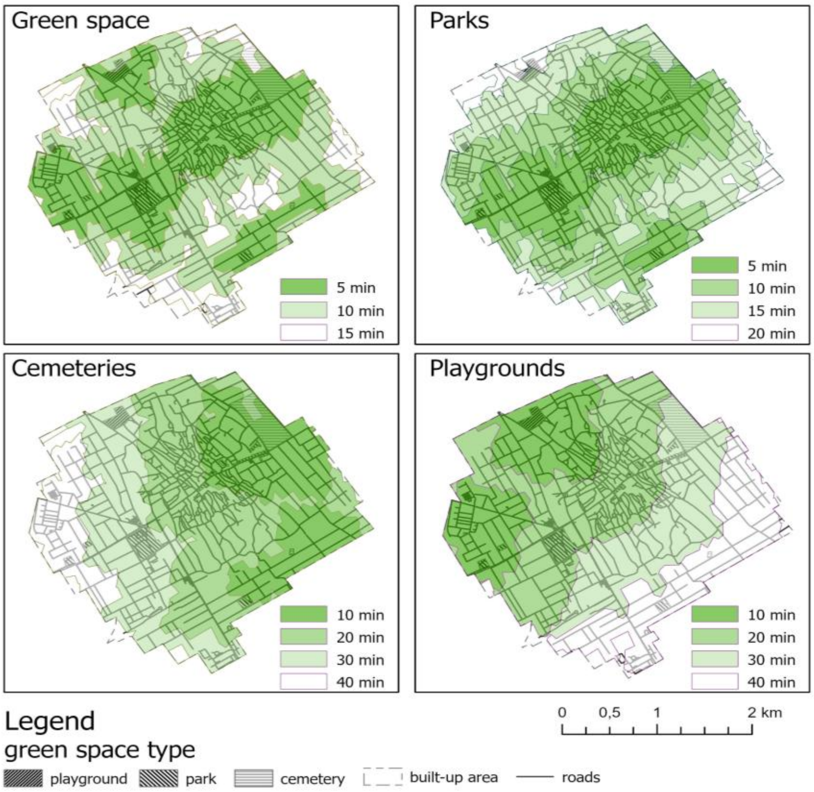

Figure 7
Green areas' pedestrian accessibility in minutes

If we consider cemeteries visited by elderly people or playgrounds that are primarily important for families with small children, a slower walking speed was assumed, and a 10-minute accessibility time was used as the basis. It can be established that neither cemeteries nor playgrounds located outside parks are reachable within 10 minutes from about three-quarters of the city. This is because these public areas are situated on the outskirts of the city. The cemeteries are located on the eastern side of the settlement, while playgrounds outside parks are on the western side.

For areas where the WHO criteria are not met, it is advisable to establish new recreational public spaces (parks, playgrounds) in the near future.

5. Conclusions

Our study examining the green areas of Mezőkövesd highlighted that using NDVI calculated from Sentinel-2 satellite images and the resulting Green Surface Intensity (ZFI) index is an effective method for spatial mapping and temporal analysis of vegetation-covered areas. The results show a positive trend in the condition of green spaces within the administrative boundaries between 2017 and 2021. However, due to the severe drought conditions starting in 2022, there was a drastic decline in vegetation health, especially in areas covered by natural vegetation. This underscores the local impacts of global climate change and the vulnerability of urban green infrastructure.

The amount of green area per capita within the built-up area exceeds the minimum recommended by the WHO but does not reach the ideal value, while some districts fall short of the desired green space availability. Accessibility to green spaces as recreational public areas is also uneven, making targeted greening interventions advisable in under-served neighbourhoods. Additionally, to improve climate resilience, it is recommended to plant drought-tolerant tree species in the city's green spaces that can better withstand climatic extremes.

Acknowledgments

This work has been implemented by the National Multidisciplinary Laboratory for Climate Change (RRF-2.3.1-21-2022-00014) project within the framework of Hungary's National Recovery and Resilience Plan support by the Recovery and Resilience Facility of the European Union.

References

Alex, E. C., Ramesh, K. V., Hari, S. (2017). Quantification and understanding the observed changes in land cover patterns in Bangalore. *International Journal of Civil Engineering and Technology (IJCIET)*, 8 (4), pp. 597–603.

Bábolna város közcélú zöldfelületeinek fejlesztési koncepciója. Varga-Erdőmester Kft. 93, 2014. https://www.babolna.hu/wp-content/uploads/2017/01/zoldteruleti-koncepcio.pdf

Bokhari, S. A., Saqib, Z., Amir, S., Naseer, S., Shafiq, M., Ali, A., Zaman-ul-Haq, M., Irshad, A., Hamam, H. (2022). Assessing Land Cover Transformation for Urban Environmental Sustainability through Satellite Sensing. *Sustainability*, 14 (5), 2810. https://doi.org/10.3390/su14052810

Bihari, Z., Babolcsai, Gy., Bartholy, J., Ferenczi, Z., Gerhátné Kerényi, J., Haszpra, L., Homokiné Ujváry, K., Kovács, T., Lakatos, M., Németh, Á., Pongrácz, R., Putsay, M., Szabó, P., Szépszó, G. (2024). Éghajlat. In: Kocsis K. (ed.).

Magyarország Nemzeti Atlasza – Természeti környezet. Budapest, HUN-REN CSFK Földrajztudományi Intézet. pp. 58–69.

Deng, J., Huang, Y., Chen, B., Tong, Ch., Liu, P., Wang, H., Hong, Y. (2019). A Methodology to Monitor Urban Expansion and Green Space Change Using a Time Series of Multi-Sensor SPOT and Sentinel-2A Images. *Remote Sensing*, 11 (10), 1230. https://doi.org/10.3390/rs11101230

Farkas, J. Zs., Hoyk, E., Batista de Morais, M., Csomós, Gy. (2023). A system review of urban green space research over the last 30 years: A bibliometric analysis. *Heliyon*, 9 (2). https://doi.org/10.1016/j.heliyon.2023.e13406

Fórian, S., Hagymássy Z. (2009). Zöldterületek szerepe az urbanizált környezetben. *Debreceni Műszaki Közlemények*, (1–2), pp. 43–52.

Jombach, S. (2014). Passzív képalkotó távérzékelés a tájkarakter-elemzésben. Doctoral (PhD) Dissertation. Budapest, Corvinus University, Doctoral School of Landscape Architecture and Landscape Ecology. https://doi.org/10.14267/phd.2014017

Kisvarga Sz., Horotán, K. (2023). *GREEN CITY a változó városi zöld*. Magyar Díszkertészek Szakmai Szervezete, 51 p.

Nascimento Aquino, D., Rocha Neto, O. C., Moreira, M. A., Santos Teixeira, A., Andrade, E. M. (2018). Use of remote sensing to identify areas at risk of degradation in the semi-arid region. *Revista Ciência Agronômica*, 49 (3), pp. 420–429.

Pifkó D., Barina Z. (2004). Adatok a Bükkalja flórájához. *Kitaibelia*, 9 (1), pp. 151–164.

Rafiee, R., Mahiny, A. S., Khorasani, N. (2009). Assessment of changes in urban green spaces of Mashad city using satellite data. *International Journal of Applied Earth Observation and Geoinformation*, 11, pp. 431–438.

Russo, A., Cirella, G. T. (2018). Modern Compact Cities: How Much Greenery Do We Need? *International Journal of Environmental Research and Public Health*, 15 (10), pp. 1–15. https://doi.org/10.3390/ijerph15102180

Salgótarján Települési Zöld Infrastruktúra Fejlesztési és Fenntartási Akcióterve. 151 p. https://www.salgotarjan.hu/wp-content/uploads/20240726_tarsadalmasitas_akcioterv.pdf

Siskané Sz. B., Szepesi, M. (2022). Városi területhasználat változások vizsgálata a CORINE adatbázis alkalmazásával. In: Bujdosó Z. (ed.). *A "ZÖLD MEGÁLLAPODÁS" – kihívások és lehetőségek. XVIII. Nemzetközi Tudományos Napok*, Gyöngyös, pp. 579–585.

Szigeti, C., Czédli, H. (2022). Városi ökológiai lábnyom és zöldterületek. *BGE Szemelvények*, pp. 220–230. https://doi.org/10.29180/978-615-6342-49-2_26

Responsible: Prof. dr. Péter Szűcs Vice-Rector
Published by the Miskolc University Press under leadership of Beáta Szabóné Kovács
Responsible for duplication: Erzsébet Pásztor
Number of copies printed:
Number of permission: MERT-2026 – 100 – ME
HU ISSN 2063-6997